First Principle simulations of electrochemical interfaces - a DFT study

Ahmed, Rizwan; Rossmeisl, Jan

Publication date:
2015

Document Version
Peer reviewed version

Ph.D Thesis

First Principle simulations of electrochemical interfaces - a DFT study

Rizwan Ahmed

Center for Atomic-scale Materials Design
Department of Physics
Technical University of Denmark

Thesis submitted for the degree of
Ph.D in Physics
February 2015

Preface

This dissertation is submitted in candidacy for the Ph. D. degree from the Technical University of Denmark (DTU). The work presented here has been carried out at the Center for Atomic-scale Materials Design (CAMD), Department of Physics from October 2011 to February 2015 under supervision of Assistant Professor Jan Rossmeisl. Financial support was provided by DTU.

Lyngby, February, 2015

Rizwan Ahmed

Acknowledgement

This thesis is the end of my journey in obtaining my Ph.D. and it has formed a strong foundation for any further research or opportunity that my destiny may lead me to. My research study has been kept on track and been seen through to completion with the support and encouragement of numerous people including my well wishers, friends, colleagues and various other people. I would like to extend my heartfelt gratitude to them all for having made this journey a truly wonderful and unforgettable experience.

First and foremost I wish to thank my supervisor Jan Rossmeisl for being supportive since the very beginning of my work. His extensive knowledge and expertise in the field of DFT has provided me with the help, guidance and inspiration that I required to complete my research study and allowed me to grow as a research scientist. Under his guidance I successfully overcame many difficulties and learned a lot. He truly has set an example for me and taught me how to achieve excellent results along with working in a relaxing atmosphere.

I would also like to acknowledge Ole H. Nielsen, Marcin Dulak and Jens J. Mortensen for keeping all the "numerous mists" of little data in place and for helping me out with all the technical issues related to hardware and software. I am very grateful to the "people working backstage" Marianne Ærsøe, Helle W. Wellejus, and Henning B. Nicolajsen for taking care of all administrative work and ensuring that everything runs smoothly in CAMD.

A special note of thanks to Mårten Björketun who proofread a major part of the thesis writing and also Martin Hangaard Hansen, Mohnish Pandey for proof reading some portions of thesis. Mohammadreza Karamad, I truly appreciate all the help you provided me to find a good starting in this new environment and workplace and I also express my gratitude to Vladimir Tripkovic for his valuable input and advice in the little talks that we had during my study.

I am sincerely indebted to my colleagues Ulrik Grønbjerg Vej-Hansen, Niels Bendtsen Halck, Chengjun Jin and Manuel Šaric for providing a stimulating and fun filled environment to work in and for making this journey of 3 years a memorable one. I also whole-heartedly thank DTU for providing the fund and backing up my research study financially without which I could not have come this far.

I specially thank Martin Hangaard Hansen for being my last moment savior and translating the abstract portion of my thesis at such a short notice. During my work I had the opportunity to meet many wonderful and extraordinary people and I feel greatly privileged for having been able to work and share short coffee/tea breaks besides having scientific or non-scientific discussions and these little moments have made my experience in DTU nothing short of amazing.

A special thanks to my family. I would like to thank my parents for making me what I am. Words cannot express how grateful I am to them for all of the love and support they have provided me throughout my life and work. Their prayers for me was what kept me sustained this far.

Lastly I am glad that Denmark has not just been a beautiful place to be but also a place which holds a distinct and valuable mark in my career path.

Abstract

In this thesis, I have looked beyond the computational hydrogen electrode (CHE) model, and focused on the first principle simulations which treats the electrode-electrolyte interfaces explicitly. Since obtaining a realistic electrode-electrolyte interface was difficult, I aimed to address various challenges regarding first principle electrochemical interface modeling in order to bridge the gap between the model interface used in simulations and real catalyst at operating conditions.

Atomic scale insight for the processes and reactions that occur at the electrochemical interface presents a challenge to both, the experimentalists, and the theorists. Energetics of charge transfer reactions over the electrochemical interface, determines, to a great extent, the efficiency of energy conversion. Therefore, gaining an atomic-level understanding of the interface, have utmost importance. Experimentalists measure macroscopic quantities, e.g., current versus voltage and have no direct information about the corresponding interfacial atomic structure. However, scanning tunneling microscope (STM) might be useful in disclosing information about the atomic structure, but it can not be performed in situ in aqueous electrolytes in order to reveal metal-water interfacial structure.

First principle calculations are useful in disclosing interfacial atomic structure, however, theorists, have other challenges to deal. Atomic scale modeling of the electrochemical interface, is still far from realistic. The real electrochemical interface is challenging to model because processes that take place over the interface are complicated. First principle methods have limitations due to the various approximations in implementations and may sometimes lead to incorrect electronic structure at the electrochemical interface, which can result in an improper/ill-defined electrochemical interface. Considering the electronic structure of the interface, I have mentioned some of the pitfalls in modeling electrochemical interfaces, and I have also shown how to avoid these pitfalls. The electrode-electrolyte interface models constructed without care for electronic structure, could exhibit an unphysical charge transfer due to the DFT's notorious under-estimation of the HUMO-LUMO gap. For such systems, electrode potential cannot be tuned. I have shown that the HOMO-LUMO gap of the electrolyte have to straddle the Fermi level, in order for the whole system to qualify as a proper electrochemical interface.

I have also contributed to the model, which accounts for pH in the first principle electrode-electrolyte interface simulations. This is an important step forward, since electrochemical reaction rate and barrier for charge transfer can strongly dependent on pH. I have shown that pH can have influence over the interface structure, and hence can influence the adsorbate free energies with direct hydrogen bonding or chemical interactions with the electrolyte dipole. Therefore, in order to study the reactions at constant electrochemical potential, pH has to be kept constant together with the chemical potential of protons and electrons. However, this was not the case for some of the calculations reported in the literature for constant electrochemical potential, where the calculations are not really done at constant electrochemical potential, as the chemical potential of proton (or pH) was not considered. However, in most of the cases, the effect of pH was negligible. We have applied this developed model to Pt(111)-water interface as an example, and constructed the corresponding Pourbaix diagram, which shows the effect of pH and potential on adsorbate coverage and interface structure.

I have also investigated the pH effect on the electrochemical adsorption of hydrogen for Pt(100) and Pt(111) surfaces by applying the above model that account for pH in the simulations. As a consequence of negligible interaction between electrolyte and adsorbed hydrogen, I found that modeled electrochemical interface and pH have no influence over hydrogen adsorption energy. In fact, hydrogen adsorption is well defined by considering just CHE model. However, barrier for charge transfer, can depend on the pH, as pH can influence the water structure at the interface. I have also discussed a scenario, where proton is more stable at the electrochemical interface, where the water layer is almost chemi-adsorbed at the surface. This is an interesting case as proton being stable in the Outer Helmholz Plane (OHP), significantly change the electrostatic potential in the double layer region. This might also have an impact over barrier for charge transfer considering hydrogen evolution reaction (HER). I have also calculated the pseudo-capacitances for hydrogen adsorption region for both surfaces, which agrees with experiments.

Resume

I denne afhandling er jeg gået udover computer hydrogen elektrode (CHE) modellen og fokuseret på simuleringer fra første principper, som behandler hele elekrode-elektrolyt grænsefladen explicit. Siden det førhen var svært at finde frem til en realistisk elekrode-elektrolyt grænseflade struktur, sigtede jeg efter at løse nogle af de udfordringer, der var forbundet med at lukke gabet imellem model grænsefladen og det virkelige katalysator under operationelle betingelser.

Atomar-skala indsigt i processerne og reaktionerne, der finder sted i den elektrokemiske grænseflade udgør en udfordring for både eksperimentalister og teoretikere. Energilandskabet for ladningsoverførselsreaktioner over den elektrokemiske grænseflade afgør i høj grad effektiviteten af elektrokemisk energikonvertering. Derfor har atomar-skala forståelse af grænsefladen den højeste vigtighed. Eksperimentalister måler makroskopiske størrelse, eksempelvis strøm som funktion af spænding, og de har derfor ikke direkte information om den atomare struktur. Skanning tunnelerings mikroskoper (STM) kan dog være nyttige til at udlede informationer om den atomare struktur, men de kan ikke opereres *in situ* i vandige elektrolytter for at afsløre metal-vand grænsefladens atomare struktur.

Beregninger fra første pricipper er nyttige til at afsløre den atomare grænsefladestrukturer, men teoretikerne har stadig udfordringer at løse. Atomar-skala modeller af den elektrokemiske grænseflade afspejler endnu ikke virkeligheden. Den virkelige elektrokemiske grænseflade er udfordrende at modellere på grund af de komplicerede processer som foregår over grænsefladen. Metoder til beregninger fra første principper er også begrænsede af forskellige approksimationer i implementeringerne og det kan i visse tilfælde lede til en ukorrekt elektronstruktur i grænsefladen, hvilket fører til ukorrekte eller dårligt definerede grænsefladestrukturer. Angående elektronstrukturen har jeg beskrevet nogle faldgruber der er forbundet med modellering af den elektrokemiske grænseflade og jeg har vist hvordan disse faldgruber kan omgås. Elektode-elektrolyte grænseflade modeller, som er konstrueret uden at holde øje med elektronstrukturen kan udvise ufysiske ladningsoverførsler på grund af tæthedsfunktionalteoriens notoriske under-estimation af HOMO-LUMO gabet. For sådanne systemer kan elektrode potentialet ikke justeres. Jeg har vist at HOMO-

LUMO niveauerne af elektrolytten er nødt til at befinde sig omkring Fermi niveauet, for at hele systemet kan kvalificere sig som en model af en elektrokemisk grænseflade.

Jeg har også bidraget til den model, som tager pH i betragtning i simulationer af den elektrokemiske grænseflade. Denne er et vigtigt skridt fremad, siden elektrokemiske reaktionsrater og -barrierer for ladningsoverførsel kan være stærkt afhængige af pH. Jeg har vist at pH kan have betydning for grænseflade strukturen, og dermed kan have betydning for fri energier af adsorbater med direkte hydrogenbindinger eller kemiske interaktioner med elektrolyttens dipol moment. Derfor er det nødvendingt at holde pH konstant sammen med det kemiske potential af protoner og elektroner i simulationer af reaktioner ved konstant elektrokemisk potential. Dette var dog ikke tilfældet for nogle beregninger der var rapporteret med konstant elektrokemisk potential i litteraturen, hvor beregningerne var foretaget uden hensyn til det kemiske potential af protoner, og dermed ikke i realiteten var ved konstant elektrokemisk potential. I de fleste tilfælde er effekten af pH dog negligibel. Vi har anvendt denne nyudviklede model til Pt(111)-vand grænsefladen som eksempel og konstrueret det tilsvarende Pourbaix diagram, som viser effekten af pH og potential på adsorbat dækningsgrader og på grænsefladestrukturen.

Jeg har også undersøgt effekten af pH på elektrokemisk adsorption af hydrogen på Pt(100) og Pt(111) overflader, ved at anvende ovenstående model til at holde regnskab med pH i simulationerne. Som en konsekvens af den negligible interaktion mellem elektrolytten og adsorberet hydrogen, fandt jeg at den modellerede elektrokemiske grænseflade ikke har nogen indflydelse på bindingsenergierne af hydrogen. Faktisk er hydrogen adsorption velbeskrevet ved at nøjes med at anvende CHE modellen. Til gengæld kan barrierne for ladningsoverførsel afhænge af pH, eftersom pH kan have betydning for vandet struktur i grænsefladen. Jeg har også diskuteret et tilfælde, hvor protonen er mere stabil i den elektrokemiske grænseflade, hvor vandlaget nærmest er kemisorberet på overfladen. Det er et interessant tilfælde, siden protonen værende mest stabil i det ydre Helmholtz lag ændrer det elektrostatiske potential i dobbeltlaget betydeligt. Dette kan også have betydning for barrieren for ladningsoverførsel, når man betragter den elektrokemiske hydrogenoverførselsreaktion (HER). Jeg har også beregnet pseudokapacitanser i hydrogenadsorptionsregionen for begge overflader, som stemmer overens med eksperimenter.

List of Included Papers

Paper I

Avoiding pitfalls in the modeling of electrochemical interfaces.

Mårten Björketun, Zhenhua Zeng, Rizwan Ahmed, Vladimir Tripkovic, Kristian S. Thygesen, Jan Rossmeisl

Chemical Physics Letters, Vol. 555, 2013, p. 145-148.

Paper II

pH in atomic scale simulations of electrochemical interfaces.

Jan Rossmeisl, Karen Chan, Rizwan Ahmed, Vladimir Tripkovic, Mårten E. Björketun

Physical Chemistry Chemical Physics, Vol. 15, No. 25, 2013, p. 10321-10325.

Paper III

Influence of the Electrochemical Interface on adsorbed H.

Rizwan Ahmed, Martin H. Hansen, Mårten E. Björketun, Jan Rossmeisl

To be sumbitted soon.

Table of Contents

LIST OF ABBREVIATIONS

AIMD -	ab initio molecular dynamics
ASHEP -	Absolute Standard Hydrogen Electrode Potential
CHE -	Computational Hydrogen Electrode potential
DFT -	Density Functional Theory
EDL -	Electrical Double Layer
emf -	electromotive force
EP -	Electrostatic Potential
ESM -	Effective Screening Medium
GGA -	Generalized Gradient Approximations
GPAW -	Grid based Projector Augmented Wave method
HER -	Hydrogen Evolution Reaction
HF -	Hartree-Fock
HK -	Hohenberg and Kohn theorem
HOMO -LUMO -	Highest Occupied Molecular orbital and Lowest Unoccupied Molecular Orbital
HOR -	Hydrogen Oxidation Reaction
LDA -	Local Density Approximation
LSDA -	Local Spin Density Approximation
MD -	Molecular Dynamics simulation
OHC -	Oceanic Heat Content
OHP -	The Outer Helmholtz Plane
ORR -	Oxygen Reduction Reaction
PAW -	Projector Augmented Wave
PBE -	Perdew-Burke-Ernzerhof
PZC -	Potential of Zero Charge
RHE -	Reversible Hydrogen Electrode

RPBE - Revised Perdew-Burke-Ernzerhof

SHE - Standard Hydrogen Electrode

SHEP - Standard Hydrogen Electrode potential

STM - Scanning Tunneling Microscope

TW - TeraWatt

UHV - Ultra-high Vacuum

WF - workfunction

WL - Water Bilayer

Chapter 1 : Introduction of Energy Scenario

Global change is bringing about enormous challenges for humanity. Modern life is sustained by a relentless stream of energy that is delivered to final users as fuels, heat and electricity. With advancement in technology, the consumption of energy worldwide has increased radically, with supply depending largely on fossil fuels plus some hydro power and then nuclear energy. Fossil fuels, as the name suggests, are very old. North Sea oil deposits are around 150 million years old, whilst much of Britain's coal began to form over 300 million years ago. Although humans probably used fossil fuels in ancient times, as far back as the Iron Age [1], it was the Industrial Revolution that led to their wide-scale extraction. In this very short period of time since then – just over 200 years – we have consumed an incredible amount of them, leaving fossil fuels all but gone and the climate seriously impacted.

Clearly fossil fuel reserves are finite – it is only a matter of when they run out. Globally, every year we currently consume the equivalent of over 11 billion tonnes of oil in fossil fuels. Crude oil reserves are vanishing at the rate of 4 billion tonnes a year[1]– if we carry on at this rate without any increase for our growing population or aspirations, our known oil deposits will be gone by 2052.

We will still have gas left, and coal too. But if we increase gas production to fill the energy gap left by oil, then those reserves will only give us an additional eight years, taking us to 2060. But the rate at which the world consumes fossil fuels is not standing still, it is increasing as the world's population increases and as living standards rise in parts of the world that until recently had consumed very little energy. Fossil fuels will therefore run out earlier. It is often claimed that we have enough coal to last hundreds of years. But if we step up production to fill the gap left through depleting our oil and gas reserves, the coal deposits we know about will only give us enough energy to take us as far as 2088. New reserves of fossil fuels are becoming harder to find, and those that are being discovered are significantly smaller than the ones that have been found in the past. Quality of life is strongly correlated with energy consumption and 90% of today's energy is produced by burning carbon based fuels (oil, coal and gas) [2]. It is evident from Fig. 1.1 shown below that mostly the countries which have a higher

income per capita show a higher consumption of energy compared to those which have a lower GDP(PPP)[1] per capita [3]. Fig. 1.2 shows the linear relationship between both[1].

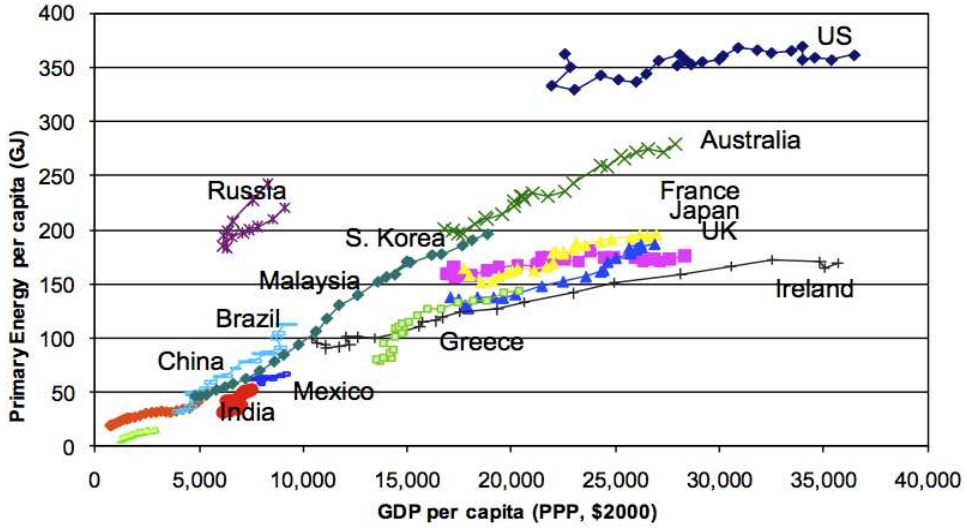

Fig. 1.1:Energy Demand and GDP(PPP)Per Capita (1980-2004) Each line represents a different country and the points are for the years 1980-2004, with the exception of Russia which is 1992-2004. Taken from ref.[3]

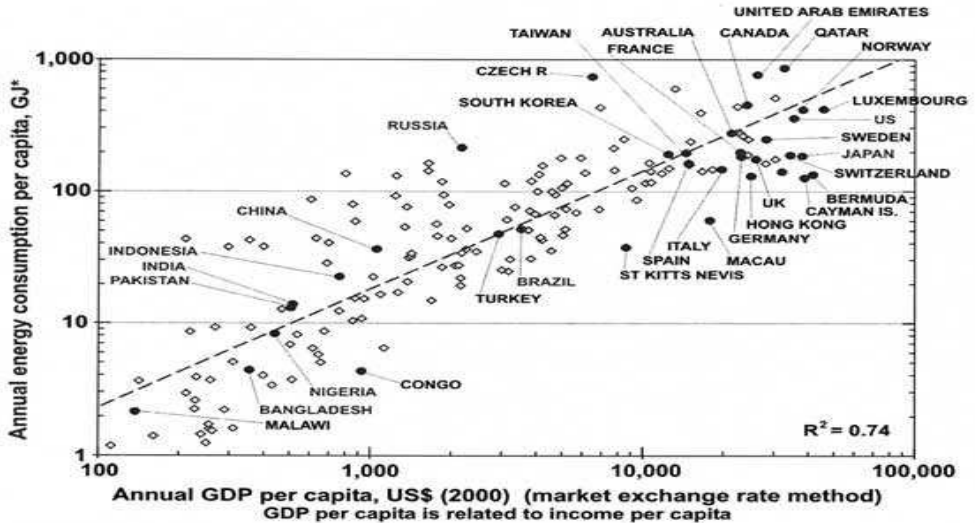

Fig. 1.2: Energy consumption according to GDP per Capita. Taken from ref.[1]

[1]**GDP(PPP)- gross domestic product (at purchasing power parity) per capita**, i.e. the purchasing power parity (PPP) value of all final goods and services produced within a country in a given year, divided by the average (or mid-year) population for the same year. GDP per capita is often considered an indicator of a country's standard of living.

Currently, over 85% of the world's primary energy supply is provided by fossil fuels (81%) and uranium minerals (5.9%) . The current global energy demand is expected to double by 2050, mainly driven by economic growth in developing countries and by an increase of human population from the current level of 7 billion to over 9 billion people. This comes with a high price, that is, the emission of carbon dioxide (CO_2)from the combustion processes into the atmosphere.

The current global energy demand is expected to double by 2050, mainly driven by economic growth in developing countries and by an increase of human population from the current level of 7 billion to over 9 billion people. This comes with a high price, that is, the emission of CO_2 from the combustion processes into the atmosphere.

Fossil fuels including coal, oil and natural gas are currently the primary sources of energy and this results in chemical products which is produced at the cost of added concern about CO_2 (green house gas) emission contributing to possible global warming. However, by mid-century, the global fossil and fissionable mineral resources will be severely depleted, whilst global warming will have affected several regions of the planet with unpredictable economic and social consequences[4]. The severity of the problem we are facing is best illustrated in Fig. 1.3*[5]*.

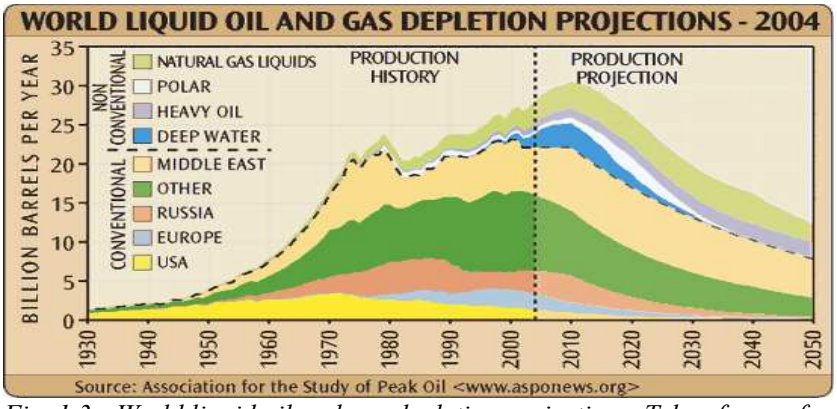

Fig. 1.3 : World liquid oil and gas depletion projections. Taken from ref. [5]

Increasing global emissions of carbon dioxide, a heat-trapping gas, are pushing the world into

dangerous territory, closing the window of time to avert the worst consequences of higher temperatures, such as melting ice and rising seas. Since the dawn of the Industrial Revolution, carbon emissions from burning fossil fuels have grown exponentially. Despite wide agreement by governments on the need to limit emissions, the rate of increase ratcheted up from less than 1 percent each year in the 1990s to almost 3 percent annually in the first decade of this century. After a short dip in 2009 due to the global financial crisis, emissions from fossil fuels rebounded in 2010 and have since grown 2.6 percent each year, hitting an all-time high of 9.7 billion tons of carbon in 2012[6] as shown in Fig. 1.4

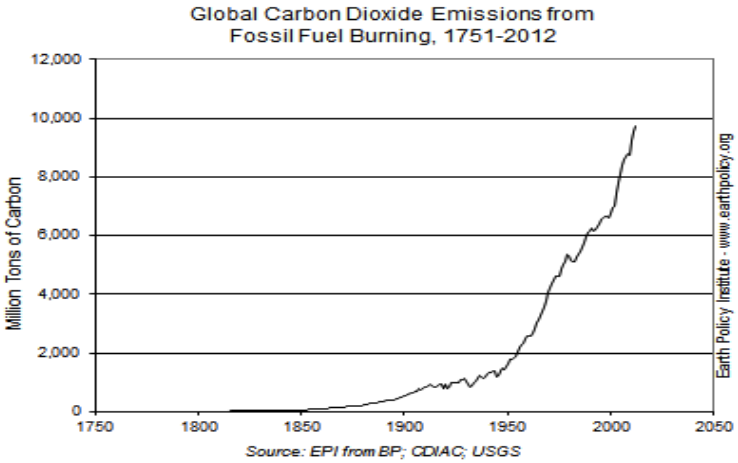

Fig. 1.4 Global Carbon dioxide emissions from fossil fuel burning for years 1751-2012. Taken from ref. [6]

The graph below Fig. 1.5, known as the Keeling Curve, shows the increase of atmospheric carbon dioxide (as parts per million by volume (ppmv)) concentrations from 1958–2008[7]. Monthly CO_2 measurements display seasonal oscillations in an upward trend; each year's maximum occurs during the

Fig. 1.5: Keeling Curve showing CO_2 measured at Mauna

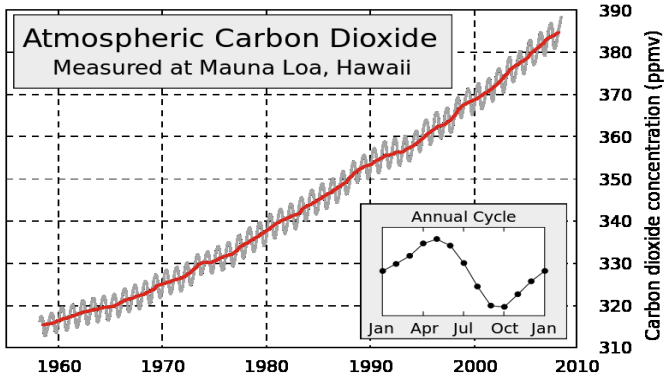

Loa, Hawaii (1960-2010).Taken from ref. [7]

Northern Hemisphere's late spring, and declines during its growing season as plants remove some atmospheric CO_2.

Fossil fuels are not the only source of CO_2 emissions. Changing the landscape, for example by burning forests, releases roughly 1 billion tons of carbon globally each year. Brazil and Indonesia have high levels of deforestation and are responsible for much of the current carbon emissions from the land. CO_2 acts like the glass of a greenhouse, trapping heat. Global warming is primarily a problem of too much carbon dioxide in the atmosphere—which acts as a blanket, trapping heat and warming the planet. This excess heat trapped by the CO_2 (produced by burning fossil fuels), is stored in earth's atmosphere, continents, and in different glaciers and ice sheets. Oceanic heat content (OHC) is the heat stored in the ocean. The increase in ocean heat content is much larger than any other store of energy in the Earth's heat balance over the two periods 1961 to 2003 and 1993 to 2003, and accounts for more than 90% of the possible increase in heat content of the Earth system during these periods as shown by Fig. 1.6 [8,9]. Changes in the ocean heat content play an important role in the current sea level rise, because of thermal expansion. It is with high confidence that ocean warming accounts for 90% of the energy accumulation from global warming between 1971 and 2010. [10]

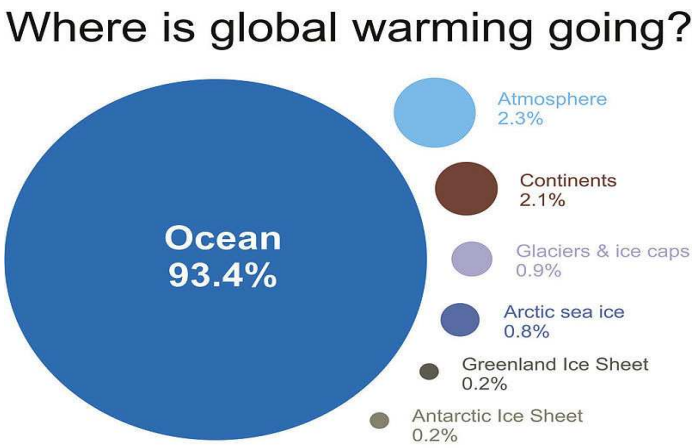

Fig. 1.6 :Oceanic heat content is much larger than any other store of energy in the Earth's heat balance. Taken from ref. [9]

As a result of burning fossil fuels on a large scale, earth's mean surface temperature has raised by about 0.8 °C (1.4 °F), with most of the increase (two-thirds) occurring after 1980 as shown in Fig. 1.7

[11].These findings are recognized by the national science academies of all major industrialized nations. The temperature is shown relative to the 1951-1980 mean, where black line, red line and green bar show the annual mean, 5 year running mean and uncertainty estimates respectively.

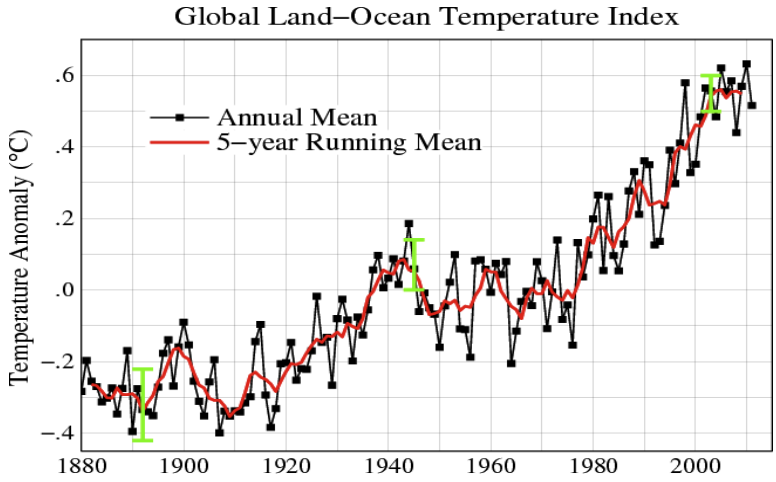

Fig. 1.7 Global mean land-ocean temperature index. Taken from ref[11]

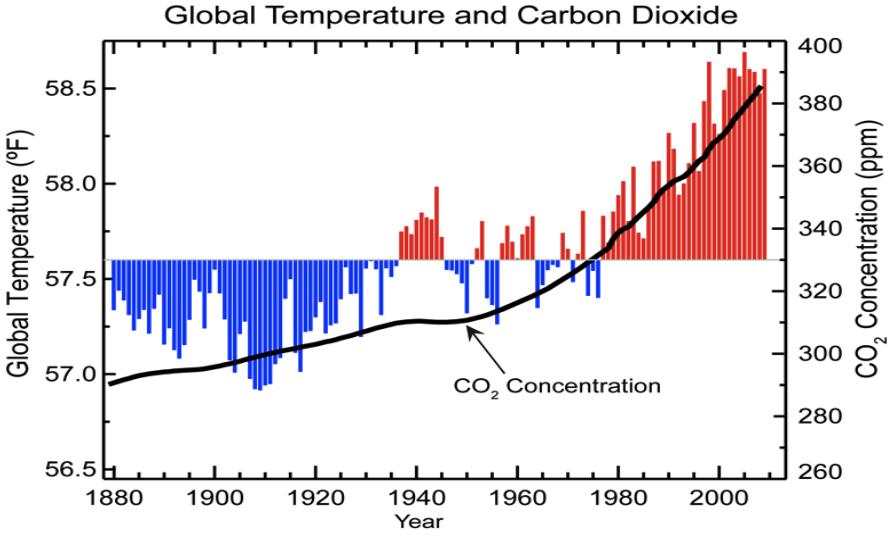

*Fig. 1.8 :*Global annual average temperature measured over land and oceans. (1880-2010). Taken from ref. [12]

In Fig. 1.8 above, it can be clearly seen that global mean ocean-land temperature correlates with CO_2 concentration in the atmosphere[12]. Red bars indicate temperatures above and blue bars indicate temperatures below the 1901-2000 average temperature. The black line shows atmospheric carbon dioxide concentration in parts per million. Projected temperature increases will most likely result in a variety of impacts including rising sea levels, disappearing Arctic sea ice, more heat waves, and declining yields of food crops. Altered weather patterns may result in more extreme weather events. And inland agricultural zones could suffer an increase in the frequency of droughts. Substantial scientific evidence indicates that an increase in the global average temperature of more than 3.6 degrees Fahrenheit (°F) (or 2 degrees Celsius [°C]) above pre-industrial levels poses severe risks to natural systems and to human health and well-being. The good news is that, because we as humans caused global warming, we can also do something about it.

There is unprecedented interest in renewable energy, particularly solar and wind energy, which provide electricity without giving rise to any carbon dioxide emission. The Earth receives an incredible supply of solar energy. The sun, an average star, is a fusion reactor that has been burning over 4 billion years. The sun provides the Earth with more energy in an hour than the global fossil energy consumption in a year. It is a source of energy many more times abundant than required by man; harnessing the free energy of the sun could therefore provide a clean and secure supply of electricity, heat and fuels. Except for nuclear energy, geothermal energy from the Earth's hot core, and energy from running water accelerated by the Earth's gravitation naturally (waterfalls) or artificially (dams), all other energy on the Earth comes from the sun. The sun's energy also plays a principal role in hydropower by driving the water cycle. Solar energy may have had great potential, but it was left on the back burner whenever fossil fuels were more affordable and available. Only in the last few decades when growing energy demands, increasing environmental problems and declining fossil fuel resources made us look to alternative energy options have we focused our attention on truly exploiting this tremendous resource. A clear picture of the solar power potential for energy source has been shown in Fig 1.9 [13].

Developing scalable, efficient and low-intensity tolerant solar energy harvesting systems represents one of the greatest scientific challenges today. The sun’s heat and light provide an abundant source of

energy that can be harnessed in many ways as shown in Fig. 1.10. Electricity can be produced from wind, waves or photovoltaic cells powered by sun and then this electrical energy can be converted in chemical energy and stored into chemical fuels by electrocatalytic processes[14]. During photosynthesis, chemical energy is created and stored in biomass, which can also be used to produce electrical power or fuels. Photoelectrocatalytic devices integrate light absorption together with electrochemical processes in order to produce chemical fuels directly from sunlight. One thing is common to all these solar energy harvesting methods, which is catalysis. Catalysis plays an important role while converting, storing and processing energy. Conversion to chemical energy is essential for transportation of energy and for storage as an intermittent energy source.

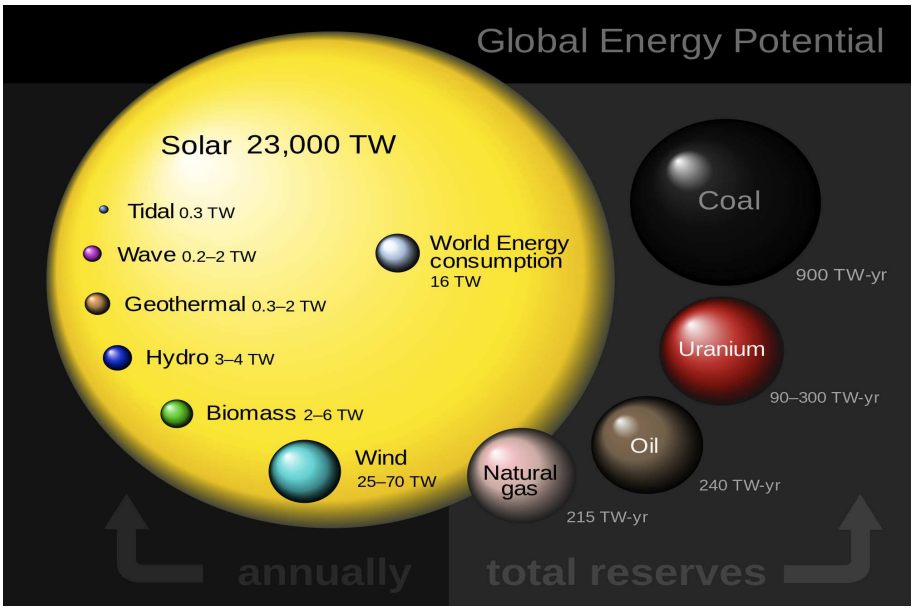

Fig 1.9 :Outstanding solar potential compared to all other energy sources. Taken from ref. [13]

However, one thing is common to all these solar energy harvesting methods, which is catalysis, so it's importance is vital. Catalysis will be introduced in a bit more detail in the subsequent chapter. In essence, catalysis is the increase in the rate of a chemical reaction due to the participation of an additional substance called a catalyst [15].With a catalyst, reactions occur faster and with less energy barrier. Catalysis plays a fundamental role in the harvesting, storage, and transformations of energy as well as in many other processes of great technological importance from gas generation to corrosion to

metal processing [16]. Because catalysts are not consumed, they are recycled, often only tiny amounts are required [17]. Catalyst will shape our modern society and it will change the way we live today. However, often good catalyst consists of precious and rare earth elements e.g. platinum and iradium which are expensive and scarce. So, finding a robust, cheap, efficient and chemically stable catalyst is a question of research and development. Many people across the globe are putting their efforts for this purpose.

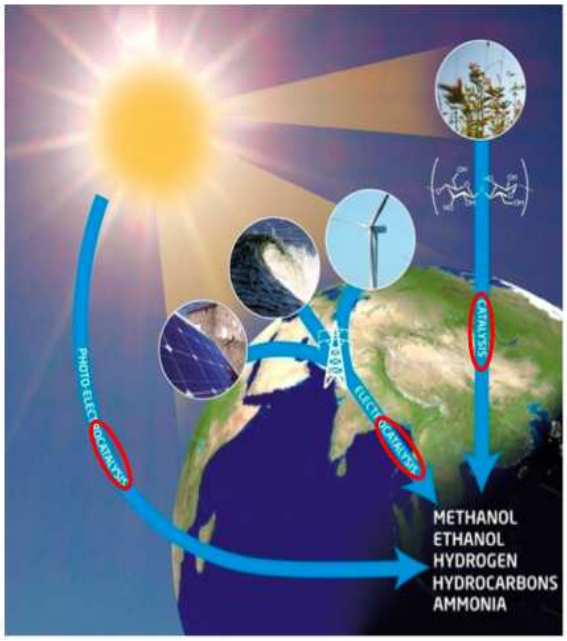

Fig. 1.10 :Different ways of harnessing the solar energy.

We use density function theory (DFT), which is a computational quantum mechanical modeling method used in various branches of science in order to investigate the properties (e.g. electronic structure) of a system. All the calculations in this thesis are done using DFT. DFT will be explained in detail in the subsequent chapters in the thesis.

1.2 Summary

Fossil fuels takes millions of years to form and we are using these at a devastating rate, which is much more rapid than the rate at which nature is able to produce them. This rapid consumption of fossil fuels

due to ever increasing energy demand may cause the reserves of fossil fuels to become limited or depleted in future while our global energy demand keeps on growing due to the development in technology and increase in population. So, there is an imminent threat of energy shortage in future.

In addition to this, burning fossil fuels at a larger scale has devastating effects on the nature and our lives. It increases the CO_2 concentration in the atmosphere which in turn causes global warming. Therefore we also need to limit the CO_2 emission in the air. We are currently facing the severe threat of the effects of global warming due to CO_2 emission. As a result of green house effect, average annual temperature of earth's surface is increasing. Increasing concentration of CO_2 in the air has a severe impact on the nature and life on earth. Thus, we need to find environment friendly and clean technologies with minimum emission of CO_2 to serve our energy needs and for a better future of mankind.

One way to get rid of these problems is to use renewable energy sources which has the added potential of minimizing CO_2 emission in the atmosphere. This can be done by using solar energy and producing solar fuels like hydrogen gas. Hydrogen has an inherent advantage of having high energy density as compared to other fuels but it has a very low volumetric storage capacity. Research is still going on in order to develop material which can store more and more hydrogen. Annual energy consumption resulting from human activities is about 17.5 TW(TeraWatt), while solar energy reaching the earth per year is about 120,000 TW. The sun has enormous potential to fulfill our future energy demand and there is plenty of solar energy which can be harvested. In order to harvest as much energy as we can to produce solar fuel like hydrogen, which is considered to be safe for atmosphere, we need to develop efficient materials for catalyst. These materials need to have properties to efficiently harvest energy, convert energy from one form to another and then store it in some form. But there are plenty of engineering challenges while designing efficient materials having these properties. A lot of experiments and computational approaches are being conducted in order to get an understanding of material challenges and then subsequently design efficient materials, which can harvest, store and convert solar energy efficiently.

Chapter 2 :Electronic Structure Calculations

2.1 Introduction

In this chapter, I will provide an overview of the computational method used to do calculations, reported throughout the thesis. First, I will discuss the main aspects of Density Functional Theory (DFT), and the different approximation which make DFT a feasible practice. Then I will discuss how we can translate and relate the DFT calculations, into some understandable form by using theoretical models, such as standard hydrogen electrode. Computer calculations have become an increasingly important tool in many areas of science due to the technological development in today's computer power and capacity.

It is well known that electronic structure of the system governs the forming/breaking of the various bonds among all the atoms inside solids and molecules. The fundamental laws of quantum mechanics can be applied to any system having various atoms in order to get its electronic structure. But, electronic structure problem can not be solved exactly for most systems having a multiple number of atoms. However, reasonable accuracy can be achieved due to the approximations being made in theoretical methods and the advent in computational power. The advent in computational power and the approximations in computational methods (improved theory), have allowed us to solve the electronic structure problem within an acceptable accuracy to many fields in science.

2.2 The Schrödinger equation

In quantum mechanics, wave function describes the quantum state of an isolated system of one or more particles. This is the one function which contains all the information about the system. Quantities such as the average momentum of a particle can be derived from this wave function. It is represented by a symbol, psi and is written as, $\Psi = \Psi(r_1, \ldots r_N;, R_1, \ldots R_K; t)$,[18] which is a function of time *t*,

electron coordinates $\{r_1,...r_N\}$ and nuclei coordinates $\{R_1,...R_K\}$ including the spin coordinate. The wave function of the system satisfies the time dependent non-relativistic Schrödinger equation

$$\hat{H}\,\Psi = i\frac{\partial}{\partial t}\,\Psi \quad , \tag{2.1}$$

$$\hat{H}\,\Psi = E\,\Psi \tag{2.2}$$

where $\hat{H}$ is called the Hamiltonian operator, acting on the wave function, and corresponds to the total energy of the system. It can be expressed as, $\hat{H} = \hat{T}_e + \hat{T}_n + \hat{V}_{en} + \hat{V}_{ee} + \hat{V}_{nn}$, where $\hat{T}$ and $\hat{V}$ represent the kinetic and potential energy operators, and subscript e and n refer to electrons and nuclei respectively. Hamiltonian can be expressed in coordinate representation[2] as,

$$\hat{H} = -\frac{1}{2}\sum_{i=1}^{N}\nabla_i^2 - \sum_{k=1}^{K}\frac{1}{2M_k}\nabla_k^2 - \sum_{i=1}^{N}\sum_{k=1}^{K}\frac{Z_k}{|r_i - R_k|} \tag{2.3}$$

$$+\frac{1}{2}\sum_{i\neq j}^{N}\frac{1}{|r_i - r_j|} + \frac{1}{2}\sum_{k\neq l}^{K}\frac{Z_k Z_l}{|R_k - R_l|}$$

where the first term is the kinetic energy of the electrons, the second term is the kinetic energy of all the nuclei, the third term is the energy due to the interactions between the electrons and the nuclei, the fourth term is the energy due to the electron electron interactions and the fifth term is the energy due to the interactions between the nuclei. The electronic and nuclei movements can be decoupled due to the fact that nuclei are 3-4 times heavier than the electrons, so we can assume that the electrons respond instantaneously to the movements of the nuclei. In other words, we can treat the heavy nuclei as fixed points, and can solve only the ground-state quantum mechanical problem for the electrons. This is called Born-Oppenheimer approximation. It will simplify the problem and allows us to just focus on the electronic part of the wave function. Looking for the stationary solution to the electronic structure problem, the time independent electronic wave function $\Phi = \Phi(r_1,....r_N)$, will satisfy the Schrödinger equation,

$$\{\hat{T}_e + \hat{V}_{en} + \hat{V}_{ee}\}\;\Phi = E\Phi, \tag{2.4}$$

[2]The Hamiltonian is written in atomic units.

The solution to equation 2.1, is not possible analytically for many-body systems. That's why the approximations are made in order to solve the ground state electronic structure problem to reasonable accuracy with no prohibitive computational resources consumption. A lot of approaches consider various approximations in order to solve electronic structure problems. Hartree-Fock (HF), configuration interaction, coupled cluster, Møller-Plesset perturbation theory and DFT are few approached to solve electronic structure problem. Each of these approaches have certain accuracy and computational power consumption and one can be chosen depending on the required accuracy.

2.3 Density Functional Theory

Computer calculations have become an increasingly important tool in many fields mainly due to the increase in computational power and capacity. Empirical and semi-empirical methods have been used in the field of catalysis for few decades, and now *ab initio* (first principles) calculations are becoming increasingly popular. These first principles calculations have more accuracy, so they have more predictive power. One of the most popular method now a days is DFT, which is extremely successful quantum mechanical approach. It has been used for many years in solid state physics for electronic structure calculations, but was not considered reasonable in quantum chemistry due to the fact that it required prohibitive amount of computational resources to reach reasonable accuracy. However, in 1990s when approximate functionals were proposed, it became very popular in quantum chemistry because approximate functionals provided a good balance between accuracy and computational cost. The approximate functionals allowed us to treat larger systems while having reasonable accuracy with no prohibitive computational resources.

As I said above, DFT is the *ab initio* method, and it does not parametrize empirical results, in fact it is not even just another way for solving Schrödinger equation. DFT approaches any interacting problem, by mapping it exactly to a much easier to solve non-interacting problem. It relies solely on electronic density in three dimensional space (cartesian coordinates). In DFT, many body problem in 3N vector space, where N is the number of quantum particles, can be mapped to a much easier to solve problem

for only 3 independent variables. Instead of writing the ground state energy in terms of Ψ , which is a function of 3N variables, DFT uses the electronic density n(r), which depends only on the 3 spatial coordinates. This enormous simplification on the number of parameters made the DFT use widespread in electronic structure calculations for quantum chemistry and condensed matter physics. The electronic density is subject to the two physical constrains

$$n(r) \geq 0, \tag{2.5}$$

and

$$\int n(r) d^3 r = N. \tag{2.6}$$

The founding father of DFT, Walter Kohn, who made essential contributions to theory, was awarded the noble prize in 1998 in chemistry.[19][20] Noble prize was co-shared by John Pople because of his DFT implementation in chemistry.[21]

2.3.1 The Hohenberg-Kohn (HK) theorem

By replacing the N-particle wave function for the Schrödinger equation, with the electron density $n(r)$, simplifies the problem from 3N variables to one with 3 variables. From a physical point of view it is evident that the ground state is uniquely defined by the external potential and the number of electrons in the potential, since the external potential specifies the Hamiltonian. The basis of DFT is the Hohenberg and Kohn theorem, which they presented in 1964 and showed that external potential can be uniquely determined by the ground state density $n(r)$ [22]. So, according to the theorem, there is one-to-one correspondence between the potential and ground state electron density. The groundstate N-particle wave function and all observables of the ground state are in principle functionals of the density $n(r)$. Therefore, the total ground state energy of a quantum mechanical electron gas is a unique functional of its density, $E[n(r)]$, which is given by

$$E[n(r)] = \langle \Psi[n(r)] | H | \Psi[n(r)] \rangle \tag{2.7}$$

where the $n(r)$ is an observable whereas the wave function is not, so by using the Raleigh-Ritz variational principle, one can minimize the energy in order to find groundstate energy and density. Using variational principles it may be shown, that the ground state density $n(r)$ minimizes the energy, $E[n(r)]$ [23]. The groundstate density minimizes $E[n(r)]$ in case the ground state is degenerate. Following the approach by Lieb and Levy[24],[25] the groundstate energy may be obtained by minimizing the energy over all possible wave functions with the density $n(r)$, and then minimizing over all densities,

$$E[n(r)] = F[n(r)] + \int v_{ext}(r)\, n(r)\, dr, \tag{2.8}$$

where $F[n(r)]$ is a universal functional of density and is the same for all the electronic structure problems because of the fact that it does not depend on the external potential as can be seen from equation 2.9. It is obtained by minimizing over all wave functions with density $n(r)$,

$$F[n(r)] = \min_{\Psi \to n(r)} \langle \Psi | \hat{T}_e + \hat{V}_{ee} | \Psi \rangle. \tag{2.9}$$

The energy functional can be rewritten as

$$E[n(r)] = F[n(r)] + V_{ext}[n(r)], \tag{2.10}$$

where $V_{ext}[n(r)] = \int v_{ext}(r)\, n(r)\, dr$ is the external potential energy. As I mentioned above, the first term in equation 2.10 is independent of the external potential and thus same for all systems having electrons interacting through the coulomb potential. The second term is easily evaluated and depends on the system. The minimization takes place over all the reasonable densities satisfying the constraints of equation 2.5 and 2.6 $(n(r) \geq 0,\ \int n(r)\, d^3r = N)$. The relation in equation 2.10 is only formal and these equations only prove that the energy is a functional of the density and Hohenberg-Kohn did not state how to obtain this functional. In 1965, Kohn and Sham published an indirect approximate approach for calculation of the energy functional $E[n(r)]$.

2.3.2 The Kohn Sham Equations

Kohn and Sham replaced the real system of interacting electrons with fictitious system of non-interacting electrons having the same electronic density as the real physical system. Then by the Hohenberg-Kohn theorem, the energies (and other groundstate observables) of these two system will be the same supposing that the densities of these two systems are also the same. The Kohn-Sham theory treat the electrons as the non-interacting particles moving in an effective potential V_{eff} while yielding the same electronic density as of the real interacting physical system. If the effective potential is constructed such that the Kohn-Sham electrons have the exact same density as the (real) interacting electrons, then the HK theorem states that the Kohn-Sham electrons also have the same energy as the interacting electrons.

Since the electrons are non-interacting for Kohn-Sham theory, Kohn-Sham equations are a set of single particle equations, which are much easier to solve than coupled Schrödinger equation (2.1, 2.2), especially for large number of electrons. Kohn-Sham equation for single electron wave function can be written as

$$\left[-\frac{1}{2}\nabla^2+v_{eff}\right]\phi_j=\epsilon\,\phi_j(r) \tag{2.11}$$

The effective potential V_{eff}, and the wave function ϕ_j can be found when the equation is solved self-consistently, hence giving the electron density,

$$n(r) = \sum_{j \in occupied} |\phi_j(r)|^2 \tag{2.12}$$

The effective potential is

$$V_{eff}(r) = V(r) + V_H(r) + V_{xc}(r), \tag{2.13}$$

where $V(r)$ is the sum of the kinetic and ionic potentials, $V_H(r)$ is the Hartree potential, given by

$$V_H(r) = \int d^3r' \frac{n(r')}{|r-r'|} \tag{2.14}$$

and $V_{xc}(r)$ is the exchange correlation potential, which is functional derivative of $E_{xc}[n(r)]$, give by

$$V_{xc}(r) = \frac{\delta E_{xc}[n(r)]}{\delta n(r)} \tag{2.15}$$

where $E_{xc}[n(r)]$ is the exchange-correlation functional which is the local function describing the electron-electron interaction. This function is not known exactly and strength of DFT relies on accurate and efficient approximations to $E_{xc}[n(r)]$. Since the effective potential V_{eff} depends on $n(r)$, the Kohn-Sham equations below must be solved in iterations until a self-consistent density is obtained.

$$\left[-\frac{1}{2}\nabla^2 + V(r) + \int d^3r' \frac{n(r')}{|r-r'|} + V_{xc}(r)\right]\phi_j(r) = \epsilon_j \phi_j(r), \tag{2.16}$$

and

$$n(r) = \sum_{j \in occupied} |\phi_j(r)|^2. \tag{2.17}$$

The Kohn-Sham equations are exact and yield the exact density, however, the exchange-correlation energy must be approximated.

2.3.3 Exchange Correlation Functionals

The Kohn-Sham equations are in principle exact, however, the exchange-correlation function is unknown and in practice exchange correlation energy has to be approximated. For most of the systems, the contribution from E_{xc} to total energy is the smallest, yet it is 100% responsible for atomization energy or chemical bonding between atoms/molecules. Its importance and practical usefulness is

evident, since it is the "glue" without which atoms would bind weekly if at all, so its accurate approximations are essential for DFT to be used in various fields. As the name exchange-corrleation implies, this term has two factors, exchange E_x and correlation factor E_c. E_x is due to the Pauli exclusion principle, which says that the two electrons with the same spin cannot have same energy (antisymmetrazation). Exchange part is usually larger than correlation part and it can be calculated exactly with the Hartee-Fock method(HF). E_c is due to the correlation and the exact value of this term is uncertain.

Kohn and Sham also proposed the simple approximations to exchange and correlation functional.[26] They assumed the exchange correlation energy for the system having electronic density $n(r)$ to be the same as for the homogeneous electron gas having same density. This is known as the local-density approximation (LDA) and can be written as,

$$E_{xc}^{LDA} = \int d^3r \;\; \epsilon_{xc}^{hom}[n(r)] \;\; n(r) \tag{2.18}$$

where $\epsilon_{xc}^{hom}\;[n(r)]$ is the energy of the exchange correlation hole in the homogeneous electron gas having density $n(r)$. LDA developed for spin-polarized systems is known as the local spin density approximation LSDA. Different parameterizations of $\epsilon_{xc}^{hom}\;[n(r)]$ exist.[27][28][29] For the system whose density varies slowly such as bulk materials, LDA works quite well despite its simplicity. LDA describes some properties such as lattice constants, vibrational frequencies and equilibrium geometries of physical systems quite well. LDA does not work well for atoms/molecules for which it tends to overestimate the binding energies. Dissociation energies of molecules and cohesive energies of solids are predicted within 10-20%, whereas the bond geometries are often predicted within 1%.

Although LDA approximations often are sufficiently accurate in solid state physics, however, DFT did not become popular in quantum chemistry until the development of the Generalized Gradient Approximations (GGA). GGA uses the density as well as density gradient in order to approximate the exchange correlation energy, which is given by

$$E_{xc}^{GGA}[n(r)] = \int d^3r \ \epsilon_{xc}^{GGA}[n(r), \nabla n(r)], \tag{2.19}$$

Contrary to ϵ_{xc}^{hom}, ϵ_{xc}^{GGA} is not uniquely defined and several GGA's have been proposed. The most widespread GGAs are PW91[30], PBE[31][32] and RPBE [33] which usually overbinds from 0.2 to 0.3 eV. The exact choice of functional will depend on the system of interest. I have used the Revised Perdew-Burke-Ernzerhof (RPBE) exchange and correlation functional for the calculations which are reported in this thesis. RPBE is believed to have improved performance for the estimation of adsorption energies.

There are many hybrid methods exist which take the exact exchange energy calculated with Hartree-Fock, and add it to the correlation energy calculated with other functionals such as PBE/RPBE in order to estimate the exchange and correlation energy in total, for the purpose to improve accuracy. The most widespread hybrids are PBE0 and B3LYP. In meta-GGAs Laplacians of the density or the kinetic energy density are also used in the calculation of E_{xc} [34][35] which are considered even more accurate. However, there is trade off between accuracy and computational cost, so the choice of exact functional depends on the requirement.

2.4 Calculation Details

The electronic structure problems were solved using density functional theory (DFT), based on the real space uniform grid based projector augmented wave [36] (PAW) method and the Revised Perdew−Burke−Ernzerhof [37] (RPBE) functional was used for exchange and correlation. The calculations were performed using the GPAW [38][39] software package integrated with the Atomic Simulation Environment [40] (ASE). Pt(111) and Pt(100) metal surfaces were represented by periodically repeated 4-layer slabs, separated by at least 15 Å of vacuum in the direction perpendicular to the surface in order to ensure convergence of work functions and energies. An optimized lattice constant of 4.0 Å and a grid spacing of 0.18 Å were used for all calculations. For both (111) and (100) surfaces, surface unit cells of size (3×3) were employed and sampled with (4×4×1) Monkhorst-Pack k-point grids. Symmetry was applied to further reduce the number of k-points. In all the cases, a dipole

correction [41] was applied in the direction perpendicular to the electrode surface in order to decouple the electrostatic interactions between periodically repeated slabs. The width of the Fermi smearing was set to 0.1 eV and energies were extrapolated to an electronic temperature of 0 K. The two bottom layers of the slabs were fixed in their bulk positions, while all other atoms were relaxed until the magnitude of the forces acting on them became less than 0.01 eV/Å.

2.5 Theoretical Electrochemistry

The improved theory of DFT together with increased computational power, have allowed many electrochemical systems to be investigated under DFT, which have driven the development of new electrocatalyst.[42][[43] [44] Electrochemistry is very rich and many-facetted science. In order to describe the chemical processes for heterogeneous catalysis, there are two main types of *ab initio* studies for electrochemical systems. One way is to just focus on the adsorption free energies of reaction intermediates on surface and neglect the electrolyte/electric field on the interface. These calculations are fast to perform now a days since omitted electrolyte will reduce the computational cost. However, these DFT calculations focusing on just the adsorption free energies have emerged a decade ago.[45] [46][47][48][49][50][51].

In other type of calculations where the interface (electrolyte) is explicitly included, one can describe the electrochemical reactions at liquid-solid interface.[52][53][54] Despite being more elaborative, these calculations also present challenges; salvation effects due to the presence of water, effects of the applied bias, and effects due to the counter-ions. The charge transfer reactions and charge transfer barriers can also be examined with these calculations. One would like to model the electrochemical environment as accurate as possible, however, many trends and relative features can be obtained with the first approach. Much of the calculations reported in this thesis are done where we explicitly modeled the whole electrochemical interface and I have discussed the electrochemical interface in more detail in the subsequent chapters. Here I will just review the methodology developed for describing trends in reaction free energies for electrochemical systems.[55] Then I will review that based on these reaction free energies, how one can get the trends in electrochemical reactivity in order

to search for the material having desired properties.

2.5.1 Computational standard hydrogen electrode

Present day computers and the theoretical methods allow *ab initio* simulations of hundreds of atoms at the quantum mechanical level. But in reality, electrochemical cell contains astronomical number of atoms, therefore, simplifications are necessary. One can study the half-cell reactions separately but this means that a reference electrode with a known fixed potential is required. For this reason, a theoretical counterpart to the standard hydrogen electrode (SHE) was established [38]. One can mimic the electrochemical half-cell by using the periodic boundary conditions in the model, so less number of atoms will be needed in the simulations. But the challenge will be to translate/link the micro-canonical calculations to grand macro-canonical stage. However, having a repetitive unit-cell will at least allow us to perform calculations and then the challenges can be addressed later as briefed in chapter 3. I will describe the model in some detail below, so consider the following reaction,

$$\frac{1}{2}H_2(g) + * \quad \Leftrightarrow \quad H^* \quad \Leftrightarrow \quad H^+(aq) + e^- + * \tag{2.20}$$

where H* is adsorbed on the surface, and * denotes surface site. By ignoring the H* we get

$$\frac{1}{2}H_2(g) + * \quad \Leftrightarrow \quad H^+(aq) + e^- + * \tag{2.21}$$

At standard hydrogen electrode potential (SHEP), pressure of the hydrogen gas will be 1 bar and the pH of the solutions will be 0 and the reaction free energy (ΔG) of any of these reactions (equation 2.21) will be zero by definition at room temperature. Hence the $\frac{1}{2}H_2(g)$ will be in equilibrium with $H^+(aq) + e^-$, and both will have same chemical potential. This means that at an electrode potential. U = 0 V, relative to standard hydrogen electrode, the free energy of proton in the solution and electron in the metal (which is difficult to calculate), can be replaced by free energy of half a hydrogen molecule

in the gas-phase. At other potential, U, relative to standard hydrogen electrode, the chemical potential of the electrons (e^-) is changed by a factor of -eU with respect to hydrogen in the gas phase. Considering this, the adsorption free energy of H*, which is adsorbed on the surface, can be related to the free energy of H_2 in the gas phase without calculating the free energy of proton in solution and electron in the metal. So, at a given potential U vs. SHE (U_{SHE}), the free energy of the reaction 2.21 will be

$$\Delta G(U) = \Delta G_0 + eU \tag{2.22}$$

Where ΔG_0 is the reaction free energy for the reaction

$$\frac{1}{2}H_2(g) + * \quad \Leftrightarrow \quad H^* \tag{2.23}$$

at standard conditions of SHE and can be directly calculated using DFT and standard molecular tables via equation 2.24

$$\Delta G_0 = \Delta E + \Delta ZPE - T\Delta S. \tag{2.24}$$

Here ΔE is the differential adsorption energy for H* and ΔZPE is the difference in zero point energy for reaction 2.23. Both can be calculated with DFT. ΔS is the entropy change for reaction 2.23. If the pH is different from SHE conditions (where the pH=0), the entropy for the protons (H^+) will change. The free energy of proton in solution depends on its concentration in solution. So, we can correct the overall free energy (equation 2.24) for reaction 2.23 by adding another term,

$$\Delta G(pH) = -K_B T \ln[H^+] = -K_B T \ln(10) \times ph \tag{2.25}$$

where K_B is Boltzmann's constant. So, the final equation will become

$$\Delta G(U) = \Delta G_0 + eU - K_B T \ln(10) \times ph \tag{2.26}$$

and this equation gives the potential, (U) and pH dependence of the reaction free energy of reaction 2.23. In this way, one can have a direct link between DFT calculations and the electrode potential, since

the reaction 2.21 defines SHEP at standard conditions. This approach is very powerful within DFT, and by using it, one can calculate the potential dependent reaction free energy for any reaction (or reaction intermediate). Principally ΔG_0 will also depend on the coverage of the adsorbate, θ , and when considering the macroscopic coverage, one will also have to include the configurational entropy as stated by the equation 2.27.

$$S_{CONF.} = -K_B \{ \theta_{H^*} \ln \theta_{H^*} + (1-\theta_{H^*}) \ln(1-\theta_{H^*}) \} \tag{2.27}$$

If we are considering the differential free energy, then differential configurational entropy, $\frac{\delta S_{CONF.}}{\delta \theta_{H^*}}$ given by the equation 2.28 should be added.

$$\frac{\delta S_{CONF.}}{\delta \theta_{H^*}} = K_B \ln\left(\frac{1-\theta_{H^*}}{\theta_{H^*}}\right) \tag{2.28}$$

However, adsorption energy of different adsorbates (i.e H*) should be calculated by simulating realistic electrochemical environment and not at ultrahigh vacuum (UHV) conditions. This means that in addition to electrode and adsorbates, one also needs to simulate electrolyte. In order to simplify the problem, we can neglect the effect of other ions, and consider only the effect of the electrolyte on the adsorption energies of adsorbates. I have modeled the electrolyte with the water bilayer which will be discussed in more detail in the next chapter. This liquid electrolyte can influence the adsorbate adsorption energy in two ways; by making direct hydrogen bonds with the adsorbates and stabilizing/destabilizing the adsorbed species via its dipole. The explicit modeling of the electrolyte is important for the adsorbates that easily form hydrogen bonds and react with water. The electric field present in the electric double layer, can interact with the adsorbates which have large dipole moments, effectively changing their adsorptions energies. For this case, external field can be included in the simulations if the electrolyte is not modeled explicitly. For other adsorbates such as H*, the effect of electrolyte is negligible as we will also see in subsequent chapters.

2.5.2 Catalytic activity: The Oxygen Reduction Reaction

Here we apply the theoretical SHE in order to investigate the oxygen reduction reaction (ORR) in order to show the power of the method. Since the method allows us to calculate the adsorption energies of all the intermediates during ORR, so lets consider the four proton and electron transfer elementary steps

$$O_2 + * + (H^+ + e^-) \rightarrow OOH^* \tag{2.29}$$

$$OOH^* + (H^+ + e^-) \rightarrow H_2O + O^* \tag{2.30}$$

$$O^* + (H^+ + e^-) \rightarrow OH^* \tag{2.31}$$

$$OH^* + (H^+ + e^-) \rightarrow H_2O + * \tag{2.32}$$

I have assumed the reaction mechanism where $H_2O_2^*$ is not formed on the surface but the reaction mechanism goes through O^* because it is more stable than the $H_2O_2^*$. For the ORR, reaction 2.29 or reaction 2.32 is potential determining step, so the conclusion will stay the same even if the reaction goes through $H_2O_2^*$. Based on the theoretical standard hydrogen electrode method discussed above, one can calculate the reaction free energies of all the intermediates (OOH^*, O^*, OH^*) using DFT and then can construct the free energy diagram at several electrode potentials, U, which is plotted in the Fig. 2.1 [56]. Height of the steps scales directly with the potential because of the fact that all steps involve exactly one $(H^+ + e^-)$ transfer.

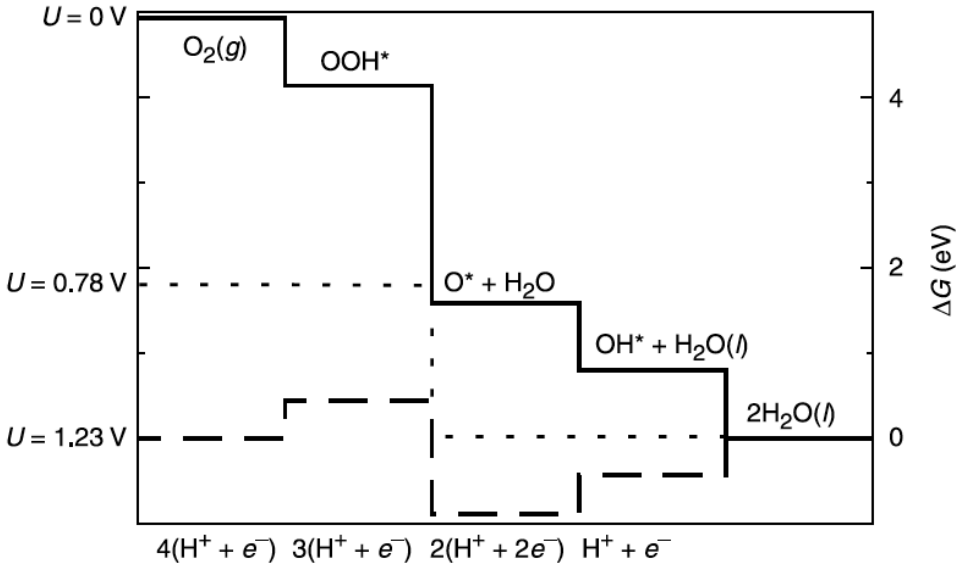

Fig. 2.1: The free energy of ORR intermediates on Pt(111) at different potentials. Adapted from [39].

At U=0 V, all the steps are strongly exothermic and this situation is roughly equivalent to the gas-phase hydrogen oxidation. This case corresponds to the reaction running by short circuiting the cell. The equilibrium potential $U_0 \approx 1.23\ V$ is the maximum potential allowed by the thermodynamics. In order to calculate the reaction free energies at equilibrium potential $U_0 \approx 1.23\ V$, the levels are moved down by $n \times 1.23\ eV$, where, n is the number of $(H^+ + e^-)$ are shown on the horizontal axis of Fig. 2.1. At this potential, the formation of OOH^* and removal of OH^* (equivalently formation of H_2O) from the surface becomes uphill. So, there are barriers for these two steps which are almost the same, meaning that reaction at the surface is slow. One can define the highest potential, U^{max}, where all the steps are downhill in free energy and overpotential, η, is $U_0 - U^{max}$. In other words, adsorbed hydroxide on the Pt(111), is thermodynamic sink for ORR and the activation energy for the maximum cell voltage, $U_0 \approx 1.23\ V$ is 0.45 eV [38] approximately. This overpotential value calculated with DFT, is close to the experimentally observed overpotential for ORR.[57] Above U^{max}, reaction is slow because catalytic reactions on the surface is slow due to the barrier. Below U^{max}, reaction is transport limited. The higher U^{max} is, the better the catalyst. A perfect catalyst will have the same hight for each step at U= 0 V and this case corresponds to the $U_0 \approx U^{max}$ by definition, where overpotential is 0 eV. If the hight is the same for each step at U= 0 V, it will result in a

flat potential energy landscape at the equilibrium potential, where the barrier will be 0 eV. Considering Pt(111), some steps have larger free energy change compared to others, meaning that Pt is not a perfect catalyst for ORR.

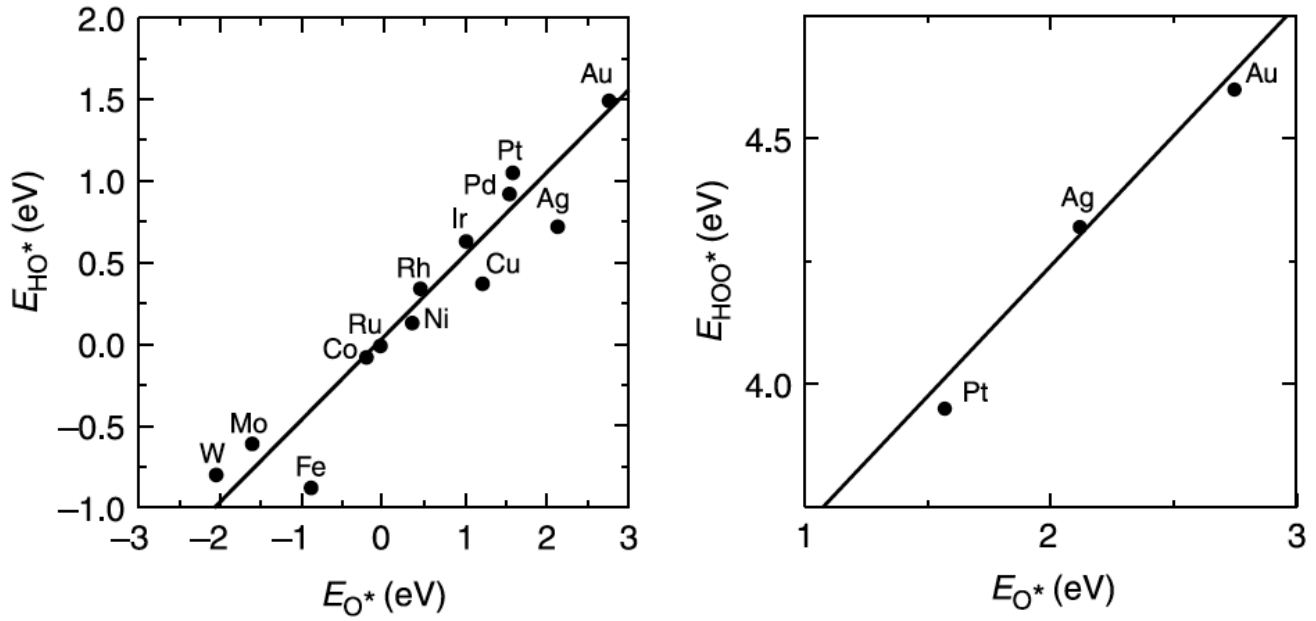

Fig. 2.2: Adsorption energies of OH and OOH* as a function of adsorption energy of O* (for terrace sites). Taken from [39]*

By focusing on the free energy diagram at equilibrium potential, one can see that peroxide (OOH*) is too weekly adsorbed on the surface, whereas atomic oxygen (O*) and hydroxyl (OH*) are too strongly adsorbed on the Pt(111) surface. The O*, OH* and OOH* binds to the surface via the oxygen atom, and the chemistry of these bonds are the same for all these intermediates. This means that the binding energies of O*, OH* and OOH* are related to each other via a constant difference. In other words, binding energy of any intermediate, can not be varied independently by just changing the catalyst, because all of these intermediates are related to each other and their binding energies scale linearly as shown by the Fig. 2.2. Alternatively, the height of different steps in Fig. 2.1, scale linearly with each other. This relationship is universal in the sense that it is independent of the catalyst surface and the constant difference in adsorption energies is only related to the internal bonds in the O, OH and OOH species.

The best linear fits for the scaling relationships shown in Fig. 2.2, are $E_{OH^*} = 0.50\,E_{O^*} + 0.05$ eV and $E_{OOH^*} = 0.53\,E_{O^*} + 3.18$ eV. Consequently, there will be an intrinsic limitation due to the correlations. This means that any catalyst where only the reactivity can be varied must have an over-potential of at least ~0.4 eV. Since the height of each step in Fig. 2.1 scales linearly with each other, which in return means that reaction free energies for the reactions 2.29, 2.30, 2.31 and 2.32 also scales with each other. As a consequence, one can use the binding energy of O* or OH* as a descriptor in order to define the reactivity for that catalyst (surface), which is shown in the Fig. 2.3. [38]

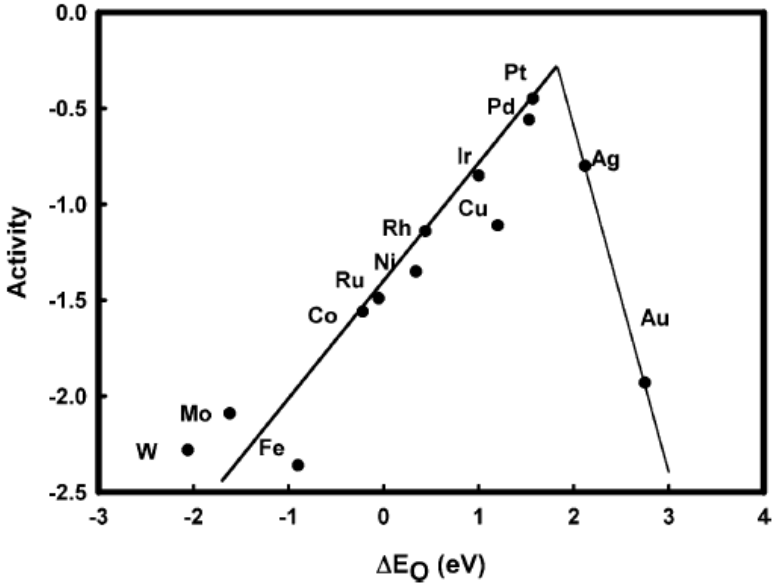

Fig. 2.3: DFT predicted trends in ORR activity as a function of ΔE_{O^*} Taken from [38].

It is evident now that Pt is the best intrinsic material for ORR. Those metals which have stronger binding of oxygen than Pt (i.e. Ni; on the left side of volcano plot), binds O* and OH* very very strongly and surface is almost poisoned due to the coverage of these species at equilibrium potential. In return the reaction is very slow, because the proton transfer to these species is very slow. In case of Au which have weaker binding of oxygen than Pt, proton transfer is fast because it is exothermic, however the oxygen is more stable in the gas phase than being adsorbed on the Au, resulting in a no transfer of proton and electron to oxygen. The weak binding of oxygen on Au, leads to another problem, which is the barrier for oxygen dissociation being large. This illustrates the Sabatier principle, which states that a good catalyst is the one which adsorbs the reactions intermediates "just right"; neither too strongly nor

too weekly but just moderately. So, the optimal catalyst, will have an optimal trade-off between being reaction while yet not being poisoned by reaction intermediates. The above analysis only deals with the adsorption energy of intermediates and in order to do better one would have to calculate the barrier for $(H^+ + e^-)$ transfer between surface and the electrolyte. However, this barrier is usually small and at present this is computationally demanding.

2.6 Summary:

In conclusion, DFT plays an important role for predicting the properties of electrochemical systems. One can calculate and analyze the electronic structure of different materials, and then those materials which give optimal properties can be subsequently tested during real experiments. This descriptor based approach for screening of electrocatalyst material, have been discussed in detail in [39]. Principally, it just can not explain the experimental results but also predict different materials on just its own due to the fact that it is based on *ab initio* calculations. For example, from Fig. 2.3, we know that an optimal extrinsic material will at least sit at the top of the volcano, however, one just need to design the material, which have just bit (~0.2 eV) weaker binding of oxygen than Pt, off course it also needs to be stable in strong electrochemical environment. DFT has predicted such materials which shows an order of magnitude higher activity than pure Pt while having reasonable stability.[25] [26] [27]

Chapter 3 : Electrochemical Electrode-Electrolyte Interface

3.1 Introduction

In the introduction chapter I have emphasized on how important it is to be less dependent on fossil fuels. Then in the second chapter we have discussed that density functional theory is an important computational tool for predicting the system properties. The strength of DFT in the quest for new catalyst materials can lead us to cheap, selective and stable catalysts while still having reasonable activity compared to catalysts based on rare earth elements [58][59][60]. We witness the impact of electrochemical reactions in our daily life and we know we need better, cheaper, more selective and robust catalysts. In the end of previous chapter, I have discussed the computational hydrogen electrode (CHE) model, which focuses on the adsorption free energies of various adsorbates on different surfaces. Many computational researchers in the past have been working on including biases in the calculations in order to study the reactions at different biases. By using this CHE model, calculations were performed and then potential was accounted later on, by shifting the free energy levels of states involving electrons by the chemical potential of those electrons [55]. By using this model, one can reduce the computational cost, where the electric field and interaction with electrolyte can be ignored. In this thesis, I aimed to looked beyond the CHE model, and address various challenges for the electrode-electrolyte interface simulations which are discussed below.

Atomic scale insight for the processes and reactions that occur at the electrochemical interface presents a challenge to both, the experimentalists, and the theorists. However, it has vital significance, since energy conversion takes place through charge transfer, that occur between electrode and the electrolyte. So, energetics of charge transfer reactions over the electrochemical interface, determines, to a great extent, the efficiency of energy conversion. Therefore, gaining an atomic-level understanding of the interface, have utmost importance. Experimentalists measure macroscopic quantities, e.g., current versus voltage and have no direct information about the corresponding interfacial atomic structure.

However, the electrochemical systems still present a challenge to experimentalists if the experiments are aiming at atomistic information, especially in situ. However, scanning tunneling microscope (STM) might be useful in disclosing information about the atomic structure, but it can not be performed in situ in aqueous electrolytes in order to reveal metal-water interfacial structure.

First principle calculations are useful in disclosing interfacial atomic structure, however, theorists, have other challenges to deal. Different models have been proposed for electrochemical interface modeling, where Skúlason's model was the most successful in describing electrochemical interface. However, atomic scale model of the electrochemical interface, is still far from realistic. At relevant conditions e.g., potential and pH, electrochemical interface modeling should reveal electrode surface with or without the charge, electrolyte, ions solvated in the electrolyte, and atomistic structure of the interface. The real electrochemical interface is challenging to model due to the fact that processes that take place over the interface are complicated.

Density function theory (DFT) has become a standard tool and is being used in various areas of materials modeling. It can not just complement experimental investigations but can also be useful in the quest for new suitable materials. During the last decade, atomic and electronic structure calculations of the electrochemical interface, treating electrode and electrolyte at the level of density function theory, have started to appear. The main reason behind it, is the increase in computational power, which has made it possible to simulate the whole electrochemical interface rather than just focusing on the electrode surface. However, the new computational methods and approximations are also being developed, which have also reduced the computational cost. But there are still limited number of atoms which can be treated within DFT and benchmarking of modeling approaches concerned with the simulation of whole the electrochemical interface, mimicking the grand canonical formulation, is still hard because it requires a prohibitive number of computationally expensive calculations. Before running computationally expensive calculations, we need to make sure that the modeling we are doing captures the features of a real system. Therefore, in order to model the electro-catalytic reactions to a reasonable level, the modeled solid-liquid interface should have the essential features of electrical double layer (EDL) and I will start with the discussion of general aspects of the EDL.

In the first principle calculations, we feed an atomic structure, which has fixed number of atoms and a fixed total charge. Then the potential, pH and other informations can be obtained as posteriori. This is in contrast to experiments, where potential and pH set up the corresponding interfacial atomic structure. Ideally one would like to include potential priori at the time of submitting calculations, so that reactions barrier can also be studied at different potentials. Unfortunately, this is not a simple task. In order to describe the solid-liquid interface to a reasonable level, we need to model the solid surface, liquid electrolyte, ions solvated in the electrolyte, possibility of charge transfer and varying the electrode potential. Many authors have proposed different methods in order to cope with these problems within the framework of DFT.

In this chapter and in the following chapters, I will review and present the solid-liquid interface properties, techniques to tune the surface charge densities as a priori, charge transfer reaction studies, techniques to align solid-liquid interface energy levels, and electrochemical potential and pH addressing in the simulations. In the start of the chapter, I will review the historical development regarding the theoretical methods mimicking the solid-liquid interface. Afterwards I will review the Skúlason's developed method to describe the solid-liquid interface. Then in the coming chapters, I will describe how to avoid the pitfalls related to energy level alignment at the interface. FurtherI will also explain how can we address the electrochemical potential and pH in simulations.

3.2 The Electrical Double Layer (EDL)

Luigi Galvani was an Italian physician who discovered in 1780 that dead a frog's leg kicked as if in life when two different metals were connected in series with the frog's two legs and he named it “animal electricity” [61]. Galvani described that an electrical fluid that is carried to the muscles by the nerves is the force that activated the muscles of his specimens. Alessandro Volta was also an Italian but physicist, who realized that the frog's leg served as both a conductor of charge (what we would now call an electrolyte) and as a detector of electricity. He replaced the frog's leg with brine-soaked paper, and detected the flow of electricity by other means familiar to him from his previous studies [62]. He tried different pairs of metals as electrodes in order to achieve maximum effect. In this way, he discovered

the law of electromotive force (emf) of a galvanic cell. He found that the emf is directly proportional to the difference between two electrode potentials, which are separated by a common electrolyte. Thus, two similar electrodes having the same electrode potential, separated by common electrolyte will give zero net emf.

3.2.1 History of computational EDL

When a bias is applied between two electrodes which are immersed in the same electrolyte, the electrons are forced to move from one electrode to the other, and in return the electrodes will become oppositely charged. The anode will become positively charged, and will attract negative ions solvated in the solution electrolyte, whereas the cathode will become negatively charged, and will attract

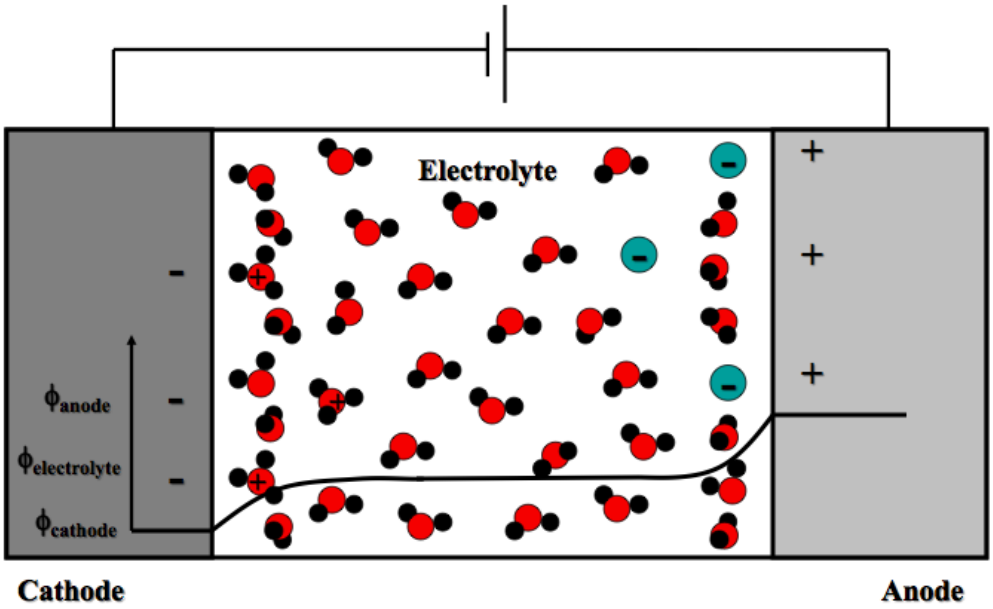

Fig. 3.1 : Schematic of an electrochemical cell along with electrode potential profile

positive ions solvated in the solution electrolyte. Depending on the bias value, positive ions will move closer to the cathode surface and negative charges will be accumulated on the cathode surface and vice versa for the anode as shown in the Fig. 3.1. An interface where a strong electric field exists, will be formed between oppositely charged metal electrode and solution electrolyte, which is usually called "electrical double layer" or simply as Helmholtz layer as shown in Fig. 3.1. This electric field will be screened as we move away from the interface towards the bulk of solution electrolyte/metal electrode

which will result in a flat (constant potential with no electric field) electrostatic potential in both the regions of bulk electrolyte and bulk metal.

This interface is very similar to a parallel plate capacitor, where we have two oppositely charged capacitor plates and an electric field exists between these plates. In the case of capacitor, the potential increases/decreases linearly while moving from one plate to another, however, a real electrochemical interface behaves little differently than a capacitor. For a more realistic interface, the electrostatic potential first changes linearly while moving away from the electrode surface towards the electrolyte since some of the counter ions are located near the surface(e.g. adsorbed covalently). Most of the electric field will be screened in this region. However, moving further away from this region towards the bulk electrolyte, yhe potential will change exponentially and finally reach a stable value in the bulk electrolyte where all the electric field will be screened. This model was developed by Stern by refining Helmholtz model and is shown in Fig. 3.2 [63][64].

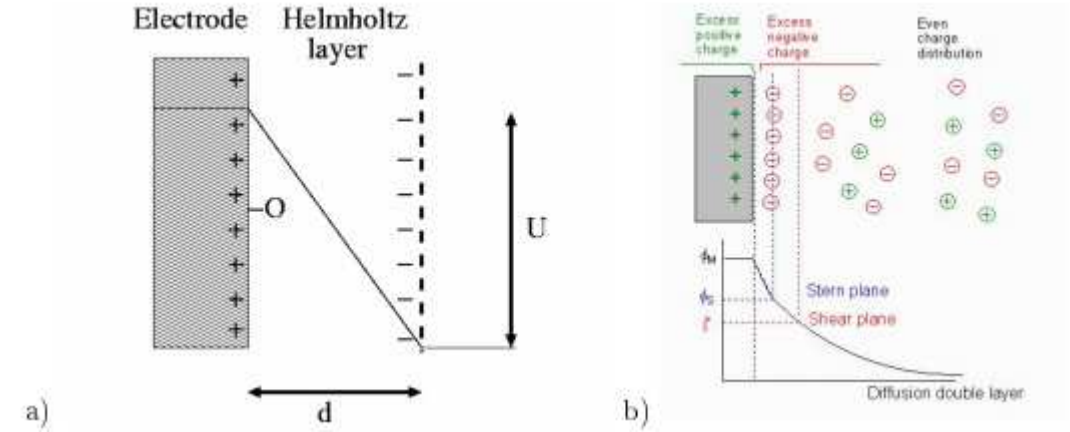

Fig. 3.2 : a) Helmholtz layer. b) The Stern model of EDL along with EP profile.

The solid-liquid interface properties are quite unique and different from either of bulk electrode and bulk liquid. In the bulk liquid, no net dipole will build up at a macroscopic level because water molecules are randomly oriented and there is an even amount of charge which will result in an electrically neutral bulk solution. At the interface, there will be force anisotropy acting from both sides of the phase, so there will be no electro neutrality. At the interface a molecule is subject to forces from

both sides of the interface, whereas in the bulk phase, it is subject to forces of equal magnitude from all directions. This force anisotropy in the EDL will force the water molecules and solvated ions to have a certain preferential orientation. On the other hand, the electrode surface will respond with electrons dragged to or from its surface. This charge separation and rearrangement on both sides of the electrochemical interface, on the metal surface and on the electrolyte end facing the surface, will result in electrostatic potential drop. Since the water dipoles will effectively screen the potential at larger distances, this potential drop is restricted to the EDL region. This potential drop will give rise to a substantial electric field, which could be as high as 0.3 V/Å due to the small thickness (~2.7 Å) of the EDL.

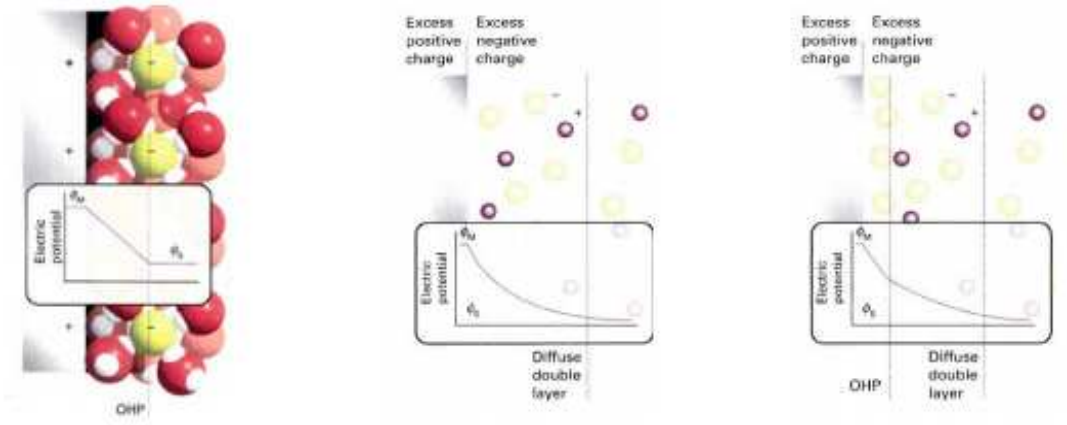

Fig. 3.3: Graphical representation of the a) Helmholtz b)Gouy-Chapman and b) Stern model of the EDL.

Adapted from [65]

The simplest model describing the interface is presented in Fig. 3.3a. It was proposed in 1853 by Hermann Ludwig Ferdinand von Helmholtz, a German scientist [66][67]. He assumed that on each side of the interface, localized opposite charges are accumulated on the planar surfaces. This interpretation is equivalent to the classical capacitor model, where a linear potential drop is observed between the two oppositely charged plates. This interface model resulted in a capacitance which is independent of potential and concentration of ions in solution. Apart from this drawback, this simple model by Helmholtz does not capture ion diffusion, specific adsorption and solvent dipoles.

Gouy and Chapman assumed that ions possess certain kinetic energies and hence they will be readily replaced from the electrode surface in compliance with some statistical distribution rule, e.g. the Boltzmann distribution [68][69]. They have addressed the shortcomings of Helmholtz's model such that the counter ions are mobilized by kinetic energies and hence they will be dispersed toward the solution. Their model is shown in Fig. 3.3b and it resulted in an exponential potential drop in the interface region and finally reaching a stable value in the bulk electrolyte at some distance from the electrode surface. Contrary to experimental observations, this model predicted exponential increase of capacitance with potential, originating from a incorrect assumption made during the integration of the Poisson equation. The electrode surface was taken to be the lower boundary in the integration because ions were considered to be point charges and hence they could completely approach the electrode.

Stern took the opportunity and successfully reproduced the true capacitance behavior by unifying the approaches by Helmholtz, and Gouy and Chapman [59]. He assumed that the counter ions have certain kinetic energies and hence they will be readily displaced from the surface of the electrode but he also included the hypothesis that counter ions can not reach closer to the electrode surface than the radius of a hydrated ion. Based on Stern's model, the resulting potential drop comprises two regions. The plane cutting through the center of the ions at their closest approach to the electrode is called “The Outer Helmholtz plane”(OHP). The first region is between the electrode surface and the OHP. This is also called a linear region because the potential drops linearly in this region. The second region is between OHP and to a point in solution where the potential reaches a reasonably stable value. This region is called diffuse layer and here the potential drops exponentially due to the thermal motion of ions. These two qualitatively different regions might have given birth to the term “double layer”. The charge distribution and potential profile for the Stern model is shown in Fig. 3.3c. The induced charge on the metal is counterbalanced by the ions in the OHP and excess of ions in the diffuse layer. However, this model does not take into account the ions adsorbed on the electrode surface, so Graham developed a new theoretical picture by taking into account the ions adsorbed on the electrode surface[70].

3.2.2 Water structure at the interface

The structure and electrochemical properties of water on various metal surfaces have utmost importance to many scientific areas, such as electrochemistry, heterogeneous catalysis, corrosion, biochemistry and many more. Electrochemical measurements on electrocatalysts are normally done at macroscopic level, measuring, e.g., current versus voltage, and offer no direct information about the atomic-scale properties of the electrochemical interface. Measurements revealing the atomic structure, such as STM, cannot easily be performed in aqueous electrolytes, and even if performed will not reveal the exact water structure together with hydrogen bonding. First principle simulations seem well suited to provide the required fundamental understanding of the structure of the electrochemical interface. Water is not just a mere spectator, but rather an active participant in a reaction when a reaction takes place in aqueous solution. The significance of establishing the true water structure rests upon the fact that water either actively takes part in a reaction mechanism or exerts its influence by stabilizing/destabilizing the reactive species through hydrogen bonding. Many experimental and theoretical research studies have been devoted in finding the exact binding structure of water on solid surfaces and resulted in disclosing ordered water films on solid surfaces [71],[72] ,[73],[74], [75], [76].

However, it is known that water binds in the form of an ice-like structure on the close packed surfaces of most transition metals, e.g., platinum [71],[78]. Water covers 2/3 of the metal and forms a honeycomb ($\sqrt{3}x\sqrt{3}$)R30 structure. This structure has two types of water molecules oriented differently, hence, called water bilayer. One type of water molecules are oriented planar to the surface and binds to surface atoms via oxygen, whereas the second type of water molecules are oriented perpendicular to the surface with H atom pointing either away (called H-up structure) or towards (called H-down structure) the metal surface. The structures are shown in Fig. 3.4. The planar water molecule binds to the surface in the same way as a single water monomer[77][78]. The H-up and H-down structures were found to have comparable stabilities across transition metals [71], [79],[80], [81]. However, water bilayers having mixed and equal orientations of H-up and H-down structures are more stable than any of the water bilayers having complete H-up or H-down structures. Michaelides has shown that the main contribution to the adsorption energy of such bilayers, comes from the water-water interaction through hydrogen bonding within the bilayer and much less contribution comes from the metal-bilayer interaction [81]. However, he has also observed that variation in the metal-bilayer interaction is responsible for the difference among bilayer adsorption energies on metal surfaces.

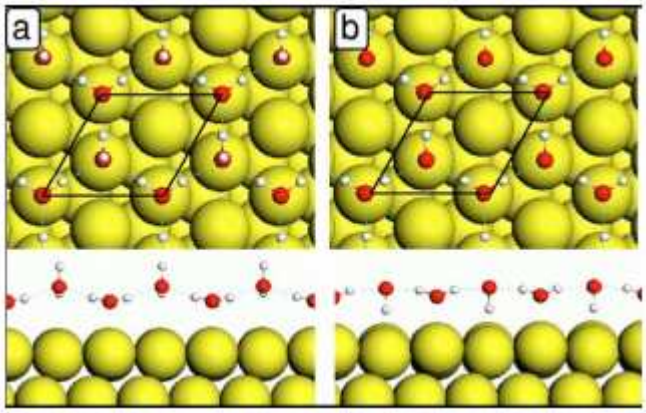

Fig. 3.4 :Side and top view of the a) H-down bilayer and b)H-up bilayer. Adapted from [81]

The second type of water molecules within the water bilayers, which are oriented perpendicular(H-up and H-down) to the closed packed surfaces, have a great influence on the metal work function. In my calculations, water bilayer where all second type water molecules have hydrogen pointing away, leads to a metal work function which is 2.7 eV less than the metal work function given by the same system but with hydrogen pointing towards the metal. This value can be compared with 2.2 eV reported by Schnur and Groß [79]. Slight charge transfer/rearrangement takes place at the interface between water bilayer and metal surface in order to equilibrate the whole system. This charge transfer give rise to an additional dipole whose magnitude and sign depends on the orientation of dangling H bond. For the case of H-up structure, the additional dipole due to the charge transfer, superimposes with the intrinsic dipole moment and hence substantial reduction of the metal work function occurs. For the case of H-down structure, the additional dipole due to charge transfer opposes the intrinsic dipole moment, which leads to a change in the metal workfunction.

Since the interaction between water bilayer and metal surface is weak compared to the interaction between hydrogen bonded water molecules within the bilayer, water bilayers do not cause any major changes in the electronic structure of the substrate they bind to [79]. It has also been seen that binding energies of other adsorbates are not considerably affected by water bilayers, unless water induce hydrogen bonds with the adsorbed species. Many reactions in real electrochemical environment take

place at room temperature and atmospheric pressure, and it is important to determine water structure at these conditions. However, many experimental studies have been devoted in disclosing the nature of water bonding on metal surfaces under ultra high vacuum conditions and at low temperatures (~200 K) [71],[82],[83], [84], [85]. Apart from temperature and pressure being different in real electrochemical systems, strong electric fields are also present and ions from the electrolyte can be co-adsorbed on metal surfaces. So that's why, most of the experimental techniques will fail in disclosing the water structure. However, finite temperatures can be included in molecular dynamics (MD) simulations, and this problem can easily be avoided. Many MD simulations have been carried out to determine the structure, bonding nature and properties of water on metal surfaces [86],[87], [88], [89]. Here I will show one which is very interesting.

Schnur and Gross took the water bilayer structures with H-up and H-down found on different transition metals in UHV studies and performed ab initio molecular dynamics (AIMD) simulations thermalized to 300 K for about 8 ps [79]. Water hexagonal structure was retained on metals with a smaller lattice constant (Ru(0001), Pt(111)) except the dangling hydrogen atoms were randomly oriented to H-up and H-down. This in fact makes sense since we know that mix of H-up and H-down in the hexagonal structure are more stable than any of complete H-up and H-down. So at room temperature, a mixture of H-up and H-down structure will dominate. But on the other hand, hexagonal structures were completely lifted for the metals having large lattice constants(Ag & Au). On these surfaces water molecules within the hexagonal ring were not strongly hydrogen bonded with each other because of the large lattice constants of the metals.

A snapshot of the structure is shown in Fig. 3.5a for AIMD simulations after 8 ps of thermal motion at 300 k for Pt(111). The evolved trajectories of oxygen atoms within hexagonal ring are also shown in Fig. 3.5b and trajectories of different oxygen atoms are color coded. From Fig. 3.5, it is obvious that the hexagonal structure remains intact for Pt(111) despite some water reorganization has occurred.

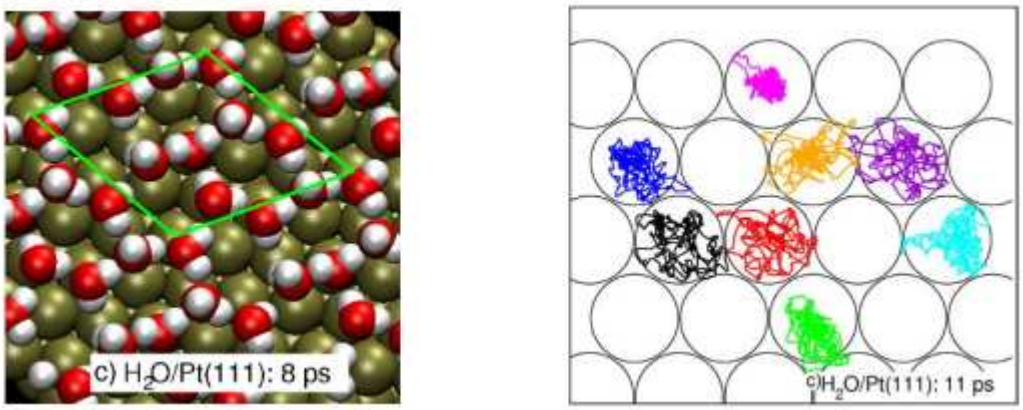

Fig. 3.5 : a) Snapshot of the water structure on Pt(111) from the AIMD simulations at 300 K. b) Trajectories of oxygen atoms in water molecules during an AIMD run. Both figures are adapted from [79].

3.3 Surface charge tuning methods

In this section, I will outline the brief history regarding electrochemical interface models developed and improved over (the period of) time, to account for potential in the simulations by explicitly changing the surface charge density of the electrode surface, so that reactions can be related to different potentials. Potentials can also be added posteriori by shifting the energy level of all the electrons for this potential value, but this simple method only allows one to study the electrochemistry of the elementary reactions while reaction barriers for charge transfer reactions are completely ignored. Many electrochemical properties depend on the electrode potential since the potential determines the atomic structure and many reactions, e.g. activation barriers, depend on the atomistic structure. So a scheme for assessing the potential is indispensable for the electrode surfaces with surface charge density explicitly changed. We will also see to which extent the postulated EDL models agree with the electrochemical solid-liquid interface.

3.3.1 The Method of Otani and Sugino

Otani and Sugino have developed a effective screening medium (ESM) method and benchmarked it on Pt(111)/water interfaces by performing AIMD simulations[90],[91],[92]. ESM allows non-periodic cell in the z direction in order to maintain the electro-neutrality for the periodically repeated cell in the x and y directions. The setup of their system is shown in Fig. 3.6, where the slab is sandwiched between

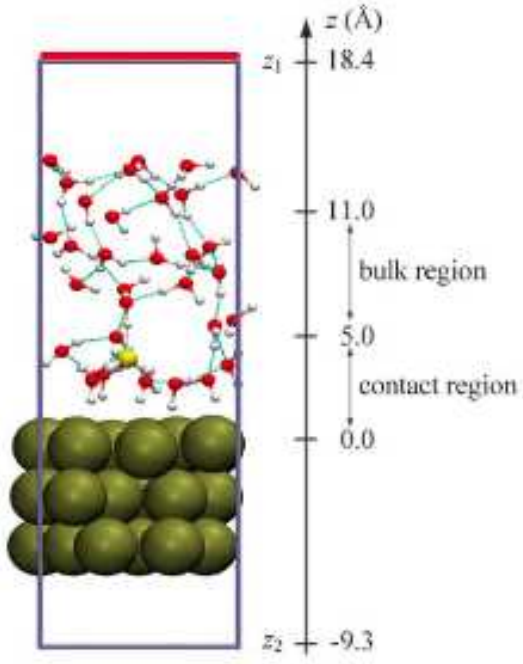

Fig. 3.6:Computational setup for the ESM method developed by Otani and Sugino. Adapted from [91]

two continuum mediums. The unit cell portion below the slab was set to represent vacuum ($\varepsilon_{r=1}$), then the electrochemical interface can be formed above the slab between electrode and electrolyte. The upper end of the unit cell can be used to represent a perfect conductor ($\varepsilon_r = \infty$), where counter charge can be placed for the charged systems in order to make whole system electro-neutral. The electrolyte was represented by 32 water molecules and an excess hydrogen atom was added in the electrolyte in order to account for strong acidic conditions they aimed to replicate. The red bar represents the onset of the perfect conductor region whereas red, white and tan spheres represent O, H, Pt atoms respectively and the yellow sphere represents the oxygen atom of a hydronium ion. The surface charge on the slab, hence the potential, can now be tuned by adding/subtracting charge from the slab and counter charge can be placed in the ideal conductor region. Near surface water molecules will be reoriented in order to effectively screen the electric field. They have divided the screening region in to two regions, contact region and the bulk region, depending on whether the region is adjacent to the electrode surface or further away in the bulk, as shown in the Fig. 3.6. Most of the potential drop will occur in the contact region and will spread through both regions. In order to measure the electrode potential, they took the reference point in the bulk region for an uncharged system, so all the potentials for charged systems were calculated with respect to this reference point level. The potential of this reference point can then be called the potential of zero charge (PZC) for that specific system.

The main advantage of this method is that potential can be varied continuously by adding/subtracting charge from the system. The downside of this method is that the electrochemical interface is poorly defined because the counter charge is placed far from the electrode surface (~ 18 Å away). It does not qualitatively agree with the theoretical picture where most of the counter charge is localized in the vicinity of the interface and strong field exist in the interface region due to the build up of these opposite charges. The reference (PZC) they used, is not universal but strongly material dependent.

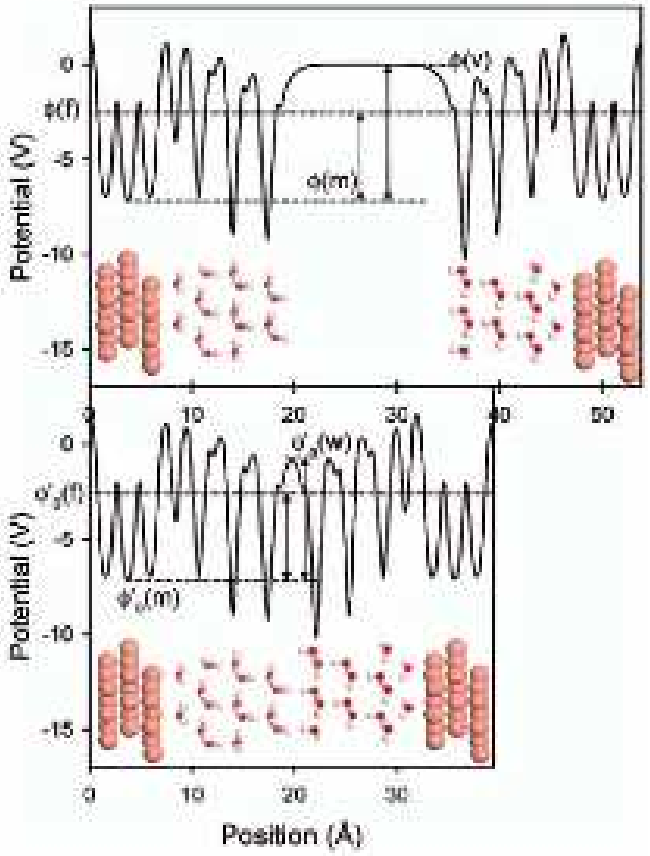

(3.1)

Fig. 3.7: Double reference method developed by Filhol and Neurock where two figure panels depict vacuum cleaved (upper panel) and the non-cleaved system (lower panel). Adapted from [93]

3.3.2 The method of Filhol and Neurock

Filhol and Neurock, also developed a method to control the surface charge and applied this method to various metal-water interfaces [93], [94],[95]. They let the counter charge be smeared out in the whole unit cell rather than placing it at some distance from the electrode surface. Electro neutrality is maintained by the counter charge and will allow to have periodic boundary conditions. Water at the interface can have a finite dipole and water polarization will induce the electrostatic potential drop across the interface. Again the surface charge can be tuned by adding/removing charge from the metal slab, and uniform background charge will induce an electric field throughout the unit cell.

The Potential in the vacuum region is not flat due to the uniform background charge smeared out through entire unit cell, so the vacuum reference point can not be established. On the other hand, a reference point in the bulk of solution can be established since the charge here is effectively screened by water regardless of its magnitude. So, the authors have used two systems, called double reference model, in order to establish a link between the vacuum level and the level in the bulk solution. They have used two uncharged systems, one with the unit cell filled with water(non-cleaved, lower panel), and the other one having a vacuum inserted in the middle of the water(cleaved, upper panel) as shown in Fig. 3.7.

Every region where the potential is flat (screened) can be regarded as reference point. In the bulk metal, the electrostatic potential will be screened by a large number of electrons, whereas in the simulated water, the electrostatic potential will be screened by the water layers. Hence, both levels in the bulk can be declared as references. The chemical potential of electrons at the Fermi level, is the same for cleaved and non-cleaved system, so we can equate these levels and establish a link between the vacuum and the bulk solution. In order to obtain unique solution potential, a portion of water molecules in the middle of the cell had to be fixed, while the rest were allowed to relax. This solution reference point can then be related back to the vacuum point through the link we have established above and then the potential is deduced from the system workfunction (WF) shown in equation (3.1) below:

$$U(vs.SHE) = e \cdot WF - U_{SHE}^{abs} \quad (3.1)$$

where U_{SHE}^{abs} is the absolute potential of the standard hydrogen electrode (SHE). Calculating the potential vs. absolute potential of SHE was first used by Trastti [96] and afterwards exploited by others [97], [98]. The WF of a system measures the potential on an absolute potential scale and absolute potential scales are meaningless unless converted to some known relative potential scale. That's why they used the experimental value for the absolute SHE potential (ASHEP). However, a range of ASHEP values (4.4-4.85) have been reported in the literature.

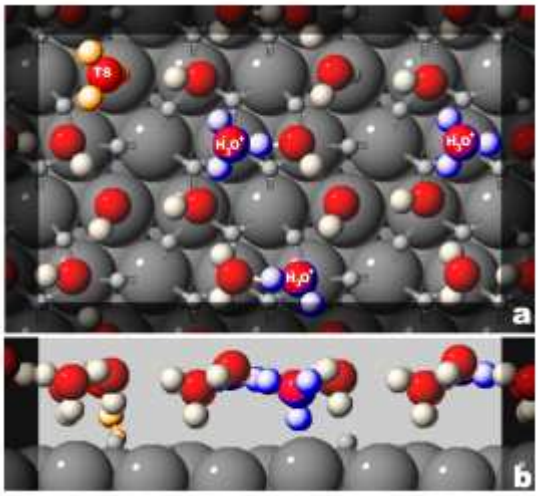

Fig. 3.8: Top (a) and side (b) view of Skúlason's model for EDL. Adapted from [98]

Again, for this method, the potential can be varied continuously by giving an excess or deficit charge to the metal slab. However, counter charge is dispersed over the entire system, which does not agree well with the classical description of EDL, where there is an accumulation of counter charge at the interface, effectively producing a strong electric field at the interface.

3.3.3 The Method of Skúlason

Egill Skúlason and coworkers introduced a simple model of the electrified solid-liquid interface in order to study the hydrogen evolution reaction (HER) and hydrogen oxidation reaction (HOR) [98]. They used a metal slab as electrode and water bilayers as electrolyte. They used close packed surfaces of the metals, since for these close packed surfaces water form hexagonal water bilayer structure due to strong hydrogen bondings among water molecules in the bilayer; this hexagonal honeycomb structure has been experimentally and theoretically identified[71]. They used only H-down bilayer in order to simulate water environment on the metal slab. They chose the H-down water bilayer because it is lower in energy when considering negatively charged surfaces, whereas the H-up structure is more favorable when the surface is positively charged [80], [99]. This is a reasonable structure to assume, since this structure was found to be most stable under ultra high vacuum conditions up to 200 K [71], [79]. This water structure was also found on Pt(111) when thermalized to room temperature, except that some water molecules change their orientations in order to point away from the surface[79]. This makes sense because the water bilayer is most stable when it has equal amount of dipole in both directions.

As we have seen, the water structure has great impact over calculated workfunction (potential). They added hydrogen to the water layer, in order to change its dipole. But system results in the formation of solvated proton (or an acid), because they found that hydrogen donates its electron to metal immediately and become solvated as a proton in the water bilayer due to the fact that DFT is a ground state state method and it automatically finds minimum. The electron from the hydrogen finds its minimum at the metal surface rather than in the water. Adding/removing hydrogen to/from a water bilayer or to other solvents in order to create acid or base is not new [94], [100], [101]. For example, Neurock and coworkers, also created an electrostatic potential difference by putting e.g. sodium atoms in their unit cell, both in the vacuum and in the water at some distance from the metal surface [93]. Since the sodium atom is highly reactive with water, a certain portion of the unit cell has to be fixed.

However, Skúlason has shown that by adding/removing hydrogen from the water bilayer, these difficilities can be easily avoided. In response to this charge separation at the interface between metal electrode and water electrolyte, a strong electric field was created. The water bilayer alone can create an electric field at the interface due to its dipole, but the magnitude of it could not be made strong enough. The electrified interface created this way corresponds to exactly the Stern's picture of the EDL

[63], [70].

The surface charge density and electrostatic potential of the double layer can be tuned by varying the number of hydrogen atoms in the unit cell, or equivalently by changing the unit cell size for the same number of protons, electrons and for same water structure. Fig. 3.8 shows the top and side view of Skúlason's model of the EDL, which contains three hydronium ions labeled as H_3O^+ and colored blue. The potential is again deduced from the workfunction of the system as was done in the double reference method.

For this method, the charges and the counter charges are localized at the interface as in real electrochemical interfaces in contrast with the other methods discussed before. That's why a strong electric field exists at the interface region due to this build up of opposite charge on either side of the interface (because of charge separation). The methods of Otani and Sugino, and Filhol and Neurock were unable to capture EDL properties, however they changed the potential by adding/removing external charge to/from the metal surface as it is done experimentally [90],[91],[92],[93]. But at real electrochemical interfaces, this excess/deficit charge is counteracted by the ions in the electrolyte, which react to the bias change in experiments. However, in computer simulations there are no explicit counter ions available in the electrolyte which can react to this excess/deficit charge. Hence the background charge is smeared out implicitly over the whole space or located far from the metal surface. One can only insert neutral atoms in state of the art *ab initio* periodically repeated calculations and expilcit counter ions cannot be added to the interface. So, the advantage of the model presented by Skúlason is that it explicitly describes the ions, surface charge, electric field at the interface and the potential. Apart from that, the strong electric field at the interface, which is real phenomena, can have effect on the energetics of chemical reactions and one can not neglect the possibility of dipole induced stability/destability at the interface.

However, for Skúlason's model, since one can-nott add partial hydrogen to the system/bilayer, the charge and in return the potential cannot be varied continuously but rather only in discrete amounts. This is the major drawback of this model in comparison to the other models where we can add/remove partial electrons from the system. For realistic electrode potentials, the charge on the surface is small, even less than one electron per 10 surface metal atoms. So, in order to mimic the real electrode

potentials, large area unit cells having more than 10 surface atoms are needed. An even more severe problem is that, when charge transfer reaction takes place, the electrochemical potential changes significantly between initial and final state due to the finite size effects. However, together with Jan Rossmeisl, they have developed a method to deal with it and it will be explained later in this chapter [102]. The difference in the resulting workfunction/potential for two different proton concentrations is shown in Fig. 3.9. The electrostatic potential (EP) is averaged in the xy direction and plotted against the direction prependicular to the surface. The electrostatic potential is also shown for the Neurock and

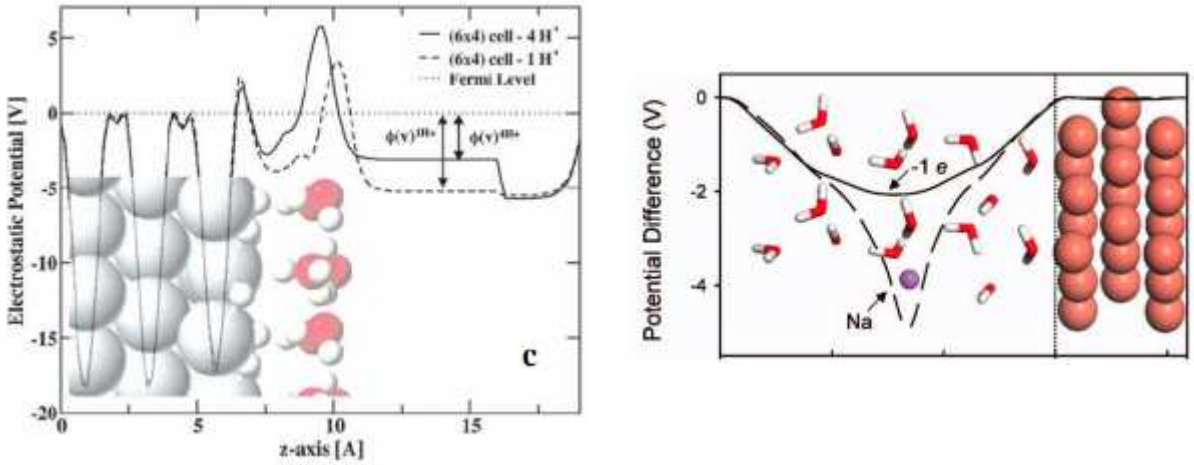

Fig. 3.9: Laterally averaged variation of the EP for two different proton concentrations. Adapted from [98],[94]

coworkers [94], where they have explicitly added a sodium atom in the simulations.

3.4 Comparision of different methods

Fig. 3.10 shows schematic models oh the different methods discussed above, along with electrostatic potential profiles, shown below, for each model. Fig. 3.10a shows a model of the ESM method developed by Otani and Sugino. Fraction of a charge can be changed, so large area unit cells can be avoided. The electrostatic potential profile and the electric field at the interface is not well defined since the counter charges are placed far away from the surface in the conductor. Since the counter charge is placed 15-20 Å away from the metal surface, the water polarization is ill-defined. Since there are not counter charge present in the electrolyte close to the surface or at the interface, so the screening will

happen both in the contact and in the bulk region. For this model, the potential drop is linear at the interface as shown in the figure.

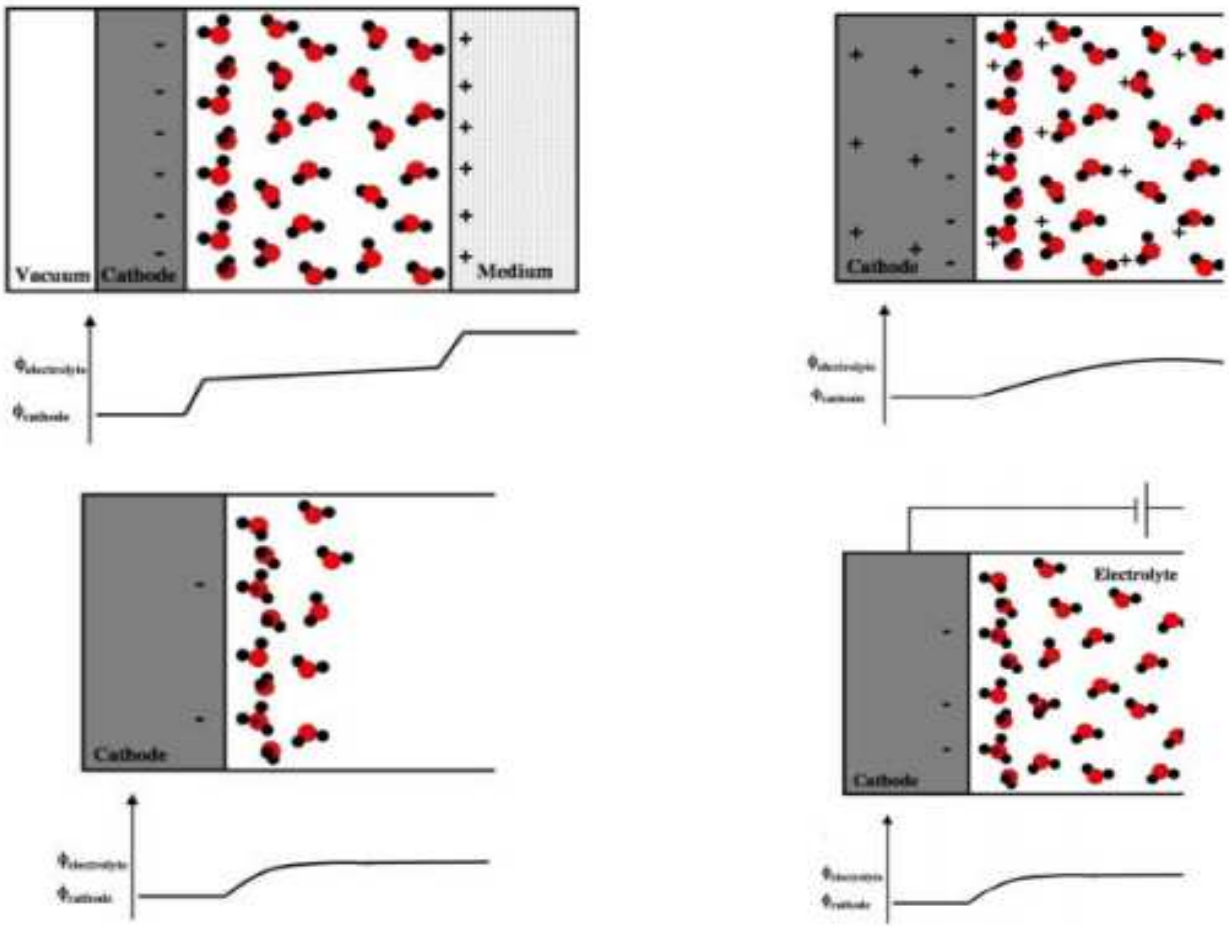

Fig. 3.10: Schematic of EDL models along with EP profiles. a) ESM model b) the double reference model c) model introduced by Skúlason et al. d) real electrochemical half cell. Adapted from [64]. (a) top left, (b) top right (c) bottom left and (d) bottom right.

The schematic and potential profile for the double reference model developed by Filhol and Neurock is shown in Fig. 3.10b. As can be seen from the schematic, this model implicitly distribute the counter charge over the entire unit cell. Again, fraction of a charge can be added/removed, so computational cost can be reduced by avoiding large area unit cells. However, since the counter charge is smeared out over whole system, the field at the interface is very poorly defined. Water is very inefficient in screening the electric field, because of the smeared charge over entire system (not explicitly located in the OHP) and due the fact that some of the water molecules are held fixed. This gives rise to a slow

exponential potential change at the interface.

For the Skúlason model shown in Fig. Fig. 3.10c , there is a one to one correspondence between the proton concentration, surface charge, electric field and potential drop, that's why it accurately mimics the real electrochemical half cell, as shown in the Fig. Fig. 3.10d. Since most of the counter ions are located at the interface, the water is very efficient in screening the electric field. A strong electric field exists at the interface as in a real electrochemical cell due to the build up of opposite charge at the interface. On the other hand, the potential can only be changed in discrete quantities. Qualitatively the potential profile for this model looks similar to classical double layer models such as the Stern and Graham [63], [70].

3.4 EDL properties for Skúlason's method

There are certain properties of the EDL which a model should exhibit. In this section we will explore certain properties of the EDL and will see whether this model exhibit these properties.

Isosurface plots are very useful in order to obtain the qualitative picture of how the charge is distributed across the system. The total charge density is usually not so interesting, but it is much interesting to study how the charge density change when chemical bonds are formed, or how the charge density changes when we add or remove charge from the system. For the cathode, negative charge is distributed on the electrode surface and positive charge is distributed on water layers close to surface. Charge density change for atoms, upon formation of chemical bonds in the molecule, can be analyzed by calculating the charge density of all individual atoms(but having same position as in molecule) and then subtracting from the total charge density of the molecule. So, for the electrified solid liquid interfaces, charge separation taking place at the solid-liquid interface can be visualized by isosurface plots of electron density differences. When the system is charged, the charge density difference can be calculated by subtracting the charge density of the uncharged system from the charged system as shown by equation (3.2) below.

$$\Delta\rho(r)=\rho_{charged}(r)-\rho_{uncharged}(r) \tag{3.2}$$

This is quite straight forward to calculate if the system is charged by adding/subtracting the charge from the slab or by applying an external potential over the system. However, for the method presented here, where the surface is charged by adding/removing hydrogen in the electrolyte, one needs to find an uncharged reference system. So, three independent charge density calculations are needed. The first calculation is for the whole system including metal slab, water bilayer and solvated protons in the water. The second calculation is for metal slab having water bilayer as an electrolyte and last calculation for hydrogen atom in a separate cell. Calculations for individual systems(references) are performed with all atoms in the same position as they were in the full system. By subtracting the charge density of the partial systems from the charge density of the whole system, one can obtain the charge redistribution upon insertion of a hydrogen atom as shown from the equation (3.3) below.

$$\Delta\rho(r)=\rho_{Pt+water+H}(r)-\rho_{Pt+water}(r)-\rho_{H}(r) \tag{3.3}$$

In Fig. 3.11 below, the isosurfaces, which are charge density differences in three dimensions, are plotted for Pt(111), when having an addition hydrogen in the first bilayer. The blue color represents the charge depletion or the accumulated positive charge which is highly localized over the hydronium ion and three adjacent hydrogen bonded water molecules in the bilayer, whereas the purple color shows the accumulated negative charge at the surface. In bulk water electrolyte, protons are solvated within two to four water molecules yielding Zundel ($H_5O_2^+$) and Eigen complexes ($H_9O_4^+$) respectively [103], [104]. The proton solvation shell in water bilayers is 2-dimensional where its size is dictated by the hexagonal water structure and it does not spread out to the water above, which shows that one water bilayer is enough to model this. In response to the proton solvation shell at the interface, the accumulated negative charge seems to spread our over whole surface.

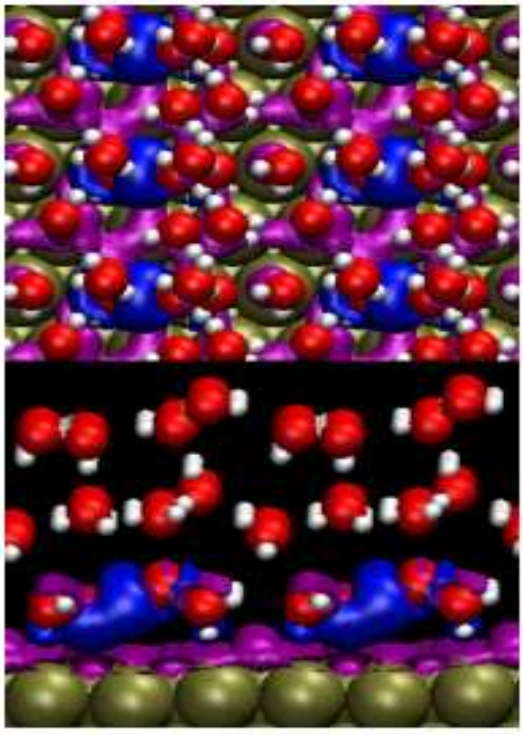

Fig. 3.11:a) top and b) a side view of water ontop of a Pt(111) electrode. Adapted from [105]

One can also calculate the electrostatic potential (EP) difference in order to quantify the charge separation taking place at the interface while charging as shown in equation (3.4). The electrostatic potential is averaged in the direction perpendicular the to surface. In order to calculate the potential difference, the potential of the separate systems have to be subtracted from the potential of the whole system, in a similar way as we did while calculating charge density difference.

$$\Delta U(r) = U_{Pt+water+H}(r) - U_{Pt}(r) - U_{water+H}(r) \tag{3.4}$$

Electrostatic potential difference is shown for different number of water bilayers in Fig. 3.12 [102]. The average EP difference obtained from MD simulation is also shown for three water layer obtained by taking the average over 60 random frames of 3ps run after thermalization, and it is very similar to the zero temperature profile [79]. We can see that the EP profile is almost fully converged for two bilayers, and it is reasonably converaged already for one water bilayer with complete H-down structure. Qualitatively, the potential profiles look similar to classical double layer models such as the Stern and Grahame models [63],[70].

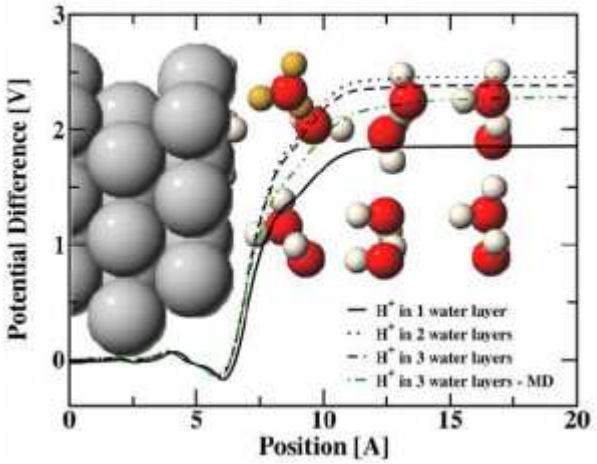

Fig. 3.12: EP for different water layers having a single proton in first bilayer for Pt(111). Adapted from [102]

We have seen that EP profile and solvation shell are reasonably well described by just one water

bilayer, and just having one water bilayer in the system reduces the computational burden. The potential can be tuned by changing the proton concentration in the water bilayer which in turn will change the surface charge. The effect of varying the proton concentration can be seen in Fig. 3.13. The proton concentration is different for three different unit cell sizes as mentioned by the labels on Fig. 3.13. They have just used one water layer since it reduces the computational cost significantly [105].

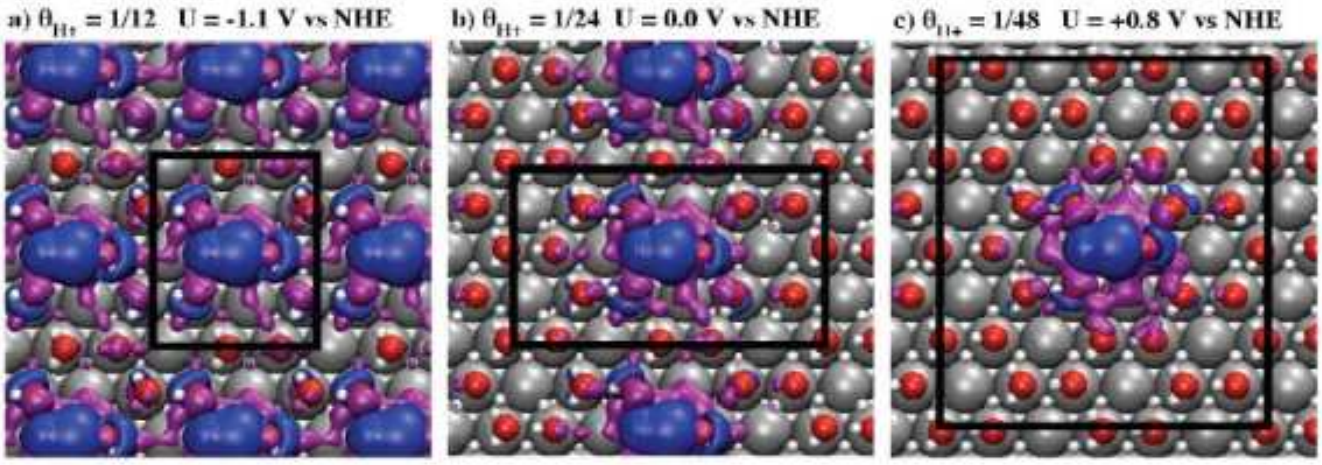

Fig. 3.13: Isosurface plots of a solvated proton for different unit cell sizes. The unit cell is designated by the black bouding box. Proton concentration and corresponding potentials are indicated above the figure panels. Adapted from [105]

As we have seen, the solid-liquid interface model resembles the Stern model of the EDL. Hence, it should share the same properties as the classical capacitor model. Here we will investigate the free energy stored in the solid-liquid interface by increasing the hydrogen amount in the water layer, which solvate as protons by giving electrons to the metal. The total or integral free energy stored in the interface per surface metal atom (or per surface area) can be calculated by the given equation (3.5),

$$G_i = \frac{G(N,n) - G(N,0) - n\mu_{H_2}}{N} \tag{3.5}$$

G_i is the function of charge per surface area, $\theta = \frac{n}{N}$, and not directly dependent on the area of the

unit cell. The chemical potential of hydrogen is μ_{H_2} . First, they have chosen μ_{H_2} so that G_i has

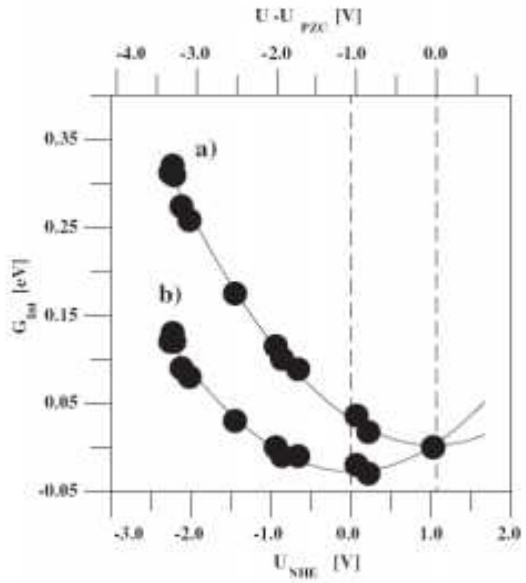

Fig. 3.14: : Integral free energy stored in the interface, plotted as a function of potential. Adapted from [102]

its minimum for the system with no protons in the water layer, where G_i is zero by definition (a). This corresponds to the potential U-U_{pzc}, where U is the electrode potential calculated from the workfunction and U_{pzc} is the potential of zero charge. For the above mentioned reason, U_{pzc} is not a universal scale but rather depends on the material. Potentials are deduced from the workfunction in the same way as in the double reference method. Then they have chosen μ_{H_2} to be equal to the energy of a proton and an electron in equilibrium with half of a hydrogen molecule at standard conditions (b). So, the minimum automatically shifts to a new value and subsequently all the potentials are re-scaled with respect to this reference value. By definition this value corresponds to the value of the standard hydrogen electrode (SHE) on an absolute scale. So, in theory, this value should be universal and not material dependent. Both the plots are shown in the Fig. 3.14 [102], where we can see that the nice parabolic features are easily observed. So, from the quadratic behavior, we can see that the interface model behaves as a capacitor as we charge it by adding hydrogen to the water bilayer. From the curvature, they have determined the capacitance, which is 26 μF/cm^2 in comparison to experimentally

determined 20 μF/cm^2 [106]. The good comparison to experiment gives further confidence concerning the structural model of the solid-liquid interface.

3.5 Extrapolation Scheme

This model is very efficient in producing Stern's EDL, but it also has some challenges. We know that hydrogen can only be added in discrete quantities, it cannot be added fractionally similarly to some other contemporary models where fractions of a charge can be added and the surface charge can be varied continuously. Another big challenge is the finite size problem. We know that at real electrochemical interfaces, reactions take place at constant electrochemical potential. However, this is not the case in DFT, where we have periodic boundary conditions and bound to use small unit cells in order to reduce the computational cost. So, in DFT the potential can change dramatically during an electrochemical reaction. For example, during a charge transfer reaction, the potential can change between initial and final state since ions set up the potential and the field. But in a real system, one would not observe this change in the bias during electrochemical reactions. There might be a local change in the electric field where the reaction is taking place, but globally the potential will essentially stay the same. In periodic DFT we always have many proton/electron transfer reactions at the same time because the unit cell is repeated.

The surface dipole changes much more during a reaction when we use a small cell. We can reduce the severity of this problem by increasing the size of the unit cell and then only allow one proton/electron transfer reaction to occur for this unit cell. When there is a lower concentration of these reactions, the potential change will be much less and we will start to reach the limit of real electrochemical reactions. However, by doing so, the computational cost increases exponentially, so there is a limited number of atoms which can be treated within DFT.

One reaction per unit cell area defines how much the potential can change. While increasing the unit cell area per reaction, reduces the finite size error and change in potential. One type of reaction can be studied for unit cells having different areas, but the same proton/electron concentration. Rossmeisl et al.

performed the calculations for the Heyrosky reaction using different unit cell sizes. The initial proton/electron concentration is the same for all the unit cells. In each case only one proton was allowed to react, so the proton concentration in the final state is different for all unit cells. The results of their calculation are shown in Fig. 3.15 [64]. We can note how the dipole change (equivalently ΔU) decreases when the unit cells are increased, but also how the reaction becomes increasingly exothermic at the same time. The activation barrier is more or less constant when we increase the unit cell size, However, if we would oxidize the H_2 molecule, going from right to left in the in the equation above Fig. 3.15, it can be seen how the activation barrier would increase when the unit cells are increased.

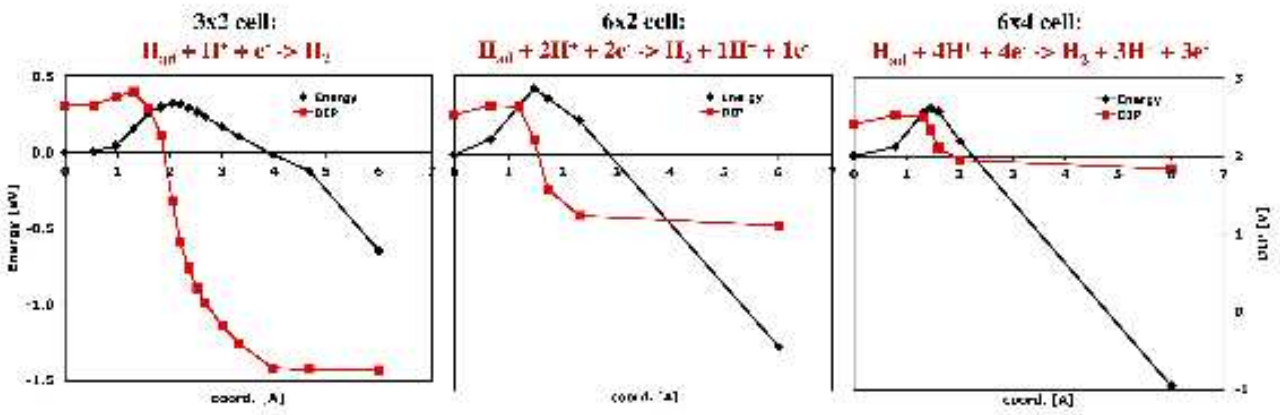

Fig. 3.15: : Surface dipole (red) and reaction energy profile along the reaction coordinate of the Heyrovsky reaction for different unit cell sizes. Adapted from [64]

Now the next question is, can we calculate the reaction energies and activation barriers for charge transfer reactions by completely avoiding finite size errors? Rossmeisl et. al. have calculated the energies for different unit cell sizes, and showed how to extrapolate the results to the limit of an infinite unit cell by following the approach above. By extrapolating the results to an infinite unit cell, where ΔU, during the reaction approaches zero, we can mimic the reactions taking place in a real electrochemical system. They have considered the hydrogen oxidation reaction (HOR), as shown in below equation (3.6), whose reverse is named hydrogen evolution reaction (HER).

$$H_2(g) + * \rightarrow H^+_{(bi)} + e^- + H^* \quad (3.6)$$

They have extrapolated the reaction free energy and the activation barrier to $\Delta U = 0$, as shown by Fig. 3.16 [102]. The variation in ΔU is obtained by using different unit cell sizes (N), with a fixed ratio of proton concentration (n/N) in the initial state. In order to extrapolate values to the limit of an infinite unit cell (or $\Delta U = 0$), one needs to perform several calculations for different unit cell sizes and it is a bit more cumbersome than ordinary calculations for surface reactions. On the other hand it is extremely important to get results mimicking the grand canonical formulation.

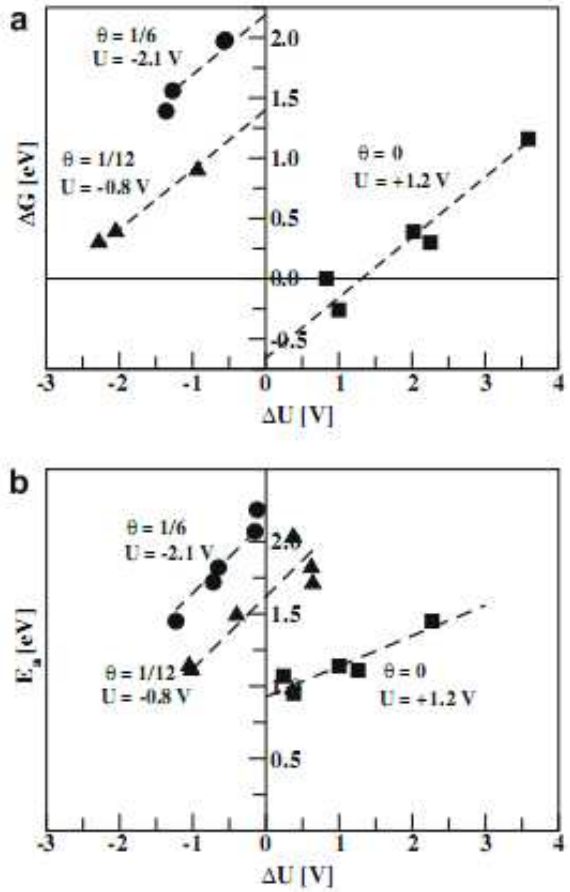

Fig. 3.16: a) The reaction free energy of the Heyrovsky reaction as a function of the electrode potential change during the reaction. b) Same as (a) but for the activation energy. Adapted from [102]

3.6 Summary

I have explained the EDL and historical development of the EDL modeling. I have outlined the advantages and disadvantages/constraints of each model and the potential profile for each model was discussed. For the ESM method presented by Otani and Sugino [90],[91],[92], we need large unit cell in the direction perpendicular to the metal surface, thus, increasing the computational cost. However, a fraction of charge can be added/removed in order to change the potential for this model. The double reference model presented by Filhol and Neurock [93],[94],[95], a background charge exists over the entire unit-cell, making it cumbersome to deduce potential. However, large area unit cells can be avoided because fraction of charge can be added/removed from metal surface.

Then I have explained in a bite more detail the electrochemical interface model, that was developed here in this group. I have elaborated the properties of the EDL, that a model should have. I have also concluded that the model behaves as a capacitor, it has linear potential drop and quadratic behavior when being charged and it agrees well with the Helmholtz picture of the EDL. We have also seen that it has strong electric field at the interface region which is true electrochemical interface property.

I have discussed the water structure and its screening of the electric field and the method to tune the bias. Furthermore, I have also discussed the constraint faced by this model, that the potential can be changed in discrete quantities rather than continuously. However, it is really simple to deduce the potential and measure the workfunction for this model. Large area unit cell are essentials in order to tune the potential in small quantities. A common problem for all the models was the finite size effects and a method was needed to translate simulations to grand canonical picture. So, in the end of this chapter, I have discussed how Jan et al. did workaround and addressed the finite size effects in DFT calculations [102].

Chapter 4 :Energy level alignment at metal-solution interfaces

4.1 Introduction:

I have discussed different models for electrochemical interfaces in the previous chapter. It was in the last decade that atomic and electronic structure simulations of the electrochemical interface at the level of density function theory (DFT) started to appear [107], [108], [109], [110], [111], [112], [113], [114], [115], [116], [117], [118], [119]. These computer simulations all face the fundamental challenge, that charge transfer reactions, which can be the main subject of the simulations, take place at a constant electrochemical potential. But the common implementation of DFT only provides results for the fixed number of electrons. I have discussed in the previous chapter, that how we can reformulate DFT in the grand canonical picture, by performing calculations for different, but fixed, number of electrons in the simulation cell. Afterwards, this set of constant-number-of-electrons calculations can be mapped into a reaction taking place at a constant chemical potential[107],[111]. As the scheme relies on all the features being calculated at varying charge, the number of simulations is about an order of magnitude larger for electrochemical reactions than for reactions not involving charge transfer. The objective of these simulations is to study charge transfer reactions and electrochemical properties that usually depend on the electrode potential. Hence, a scheme for assessing the potential is indispensable. For all the interface models discussed in previous chapter, the workfunction which is evaluated in vacuum outside the interface, is normally used as a measure of the electrode potential [107], [116], [120], [121]. The DFT methods have indeed proven valuable and promising in providing atomic level descriptions of various properties of the electrochemical interface [109],[112], [114], [116], [122], [175],165].

In this chapter, I will discuss some of the pitfalls in the electrochemical interface modeling. We have investigated the alignment of metal and molecular electronic energy levels at the electrode-electrolyte interfaces using DFT. We have found and addressed a critical issue regarding the electronic structure of the interface, which is the alignment of metal and molecular electronic energy levels[123]. This

critical issue so far, with a few notable exceptions,[117], [119], [124] has been largely overlooked in ab initio electrochemical modeling. A universal behavior is observed and three qualitatively different regimes, exhibiting qualitatively different energy level alignments are observed. The regimes are defined by the size of the metal workfunction relative to the ionization potential and/or electron affinity of the electrolyte. I will demonstrate that proper matching of these quantities is essential for successful *ab initio* modeling of electrochemical interfaces and it is further discussed how such matching can be obtained by careful tailoring of the interfacial atomic structure.

Only the electrode-electrolyte combinations with metal work functions larger than the electron affinity and smaller than the ionization potential constitute true electrochemical systems. In other words, HOMO and LUMO levels of the isolated electrolyte have to straddle the Fermi level of the metal electrode in order for the combined system to qualify as an adequate model of the electrochemical interface. These systems fall into the middle regime and constitute systems with a tunable electrode potential. When the work function of the bare metal falls outside the HOMO-LUMO range, the interface becomes conductive and charge is transferred between the originally neutral electrode and electrolyte. For such systems it is not possible to model changes in the electrode potential. Although a conductive interface might sometimes be a true physical effect, it is often a consequence of the unphysical self-interaction experienced by electrons in conventional DFT, which introduces errors in calculated electron affinities and ionization potentials.

Spurious interfacial charge transfer has implications beyond the field of electrochemical interface modeling. For instance, it will give an additional contribution to workfunctions calculated for metal-water systems, thus making comparisons between experimental and theoretical structures ambiguous. Unfortunately, there is no obvious way of correcting an inaccurate interfacial electronic structure. Extending the atomic model by including more of the electrode and the electrolyte in the simulations does not automatically improve the electronic descriptions. Even though neither more advanced DFT implementations are enough to ascertain that the model represents a real electrochemical interface, nor does a correct experimental atomic configuration guarantee that an electronic structure fulfills the necessary requirements. However, the very same objective can be achieved by controlling the atomic configuration and carefully analyzing the corresponding electronic structure.

4.2 Metal-solution interfaces:

For the modeled electrochemical interface, I have explained in detail in previous chapter that how surface charge density and hence the electrode potential can be varied in order to study the reactions at different biases. By injecting (removing) electrons into (from) the metal slab[107] or by adding hydrogen atoms to the first water layer[111], [116], surface charge density and hence the corresponding electrode potential can be varied. In the former case the additional negative (positive) charge is compensated by a background charge of opposite sign to ensure overall charge neutrality of the computational cell. In the latter case, the additional hydrogen atoms spontaneously separate into protons that become solvated in the water bilayer and electrons that end up on the surface of the metal slab. Again the computational cell remains charge neutral. I have adopted the Skúlason's interface model, described in some detail in the previous chapter and the later approach to change the surface charge in the calculations reported throughout my thesis. Based on the relative size, the so-called Integer Charge Transfer model,[125] applicable to interfaces with weak interaction between electrodes and electrolytes, identifies three different regimes, where each regime have a unique alignment of metal and molecular electronic energy levels. Here I will discuss the three different regimes (or regions) defined by $\Phi_M \precsim E_A$ (region I), $E_A \precsim \Phi_M \precsim E_I$ (region II) and $\Phi_M \succsim E_I$ (region III), exhibiting qualitatively different energy level alignments. Alignment of electronic energy levels in these regimes is discussed comprehensively in [120], [113]. Here, only few systems have been investigated showing different alignments in order to just establish concepts.

The relevant symbols in the discussion of energy level alignment stand as, M for metal, E_F for metal Fermi level, Φ_M for bare metal workfunction, V_M represent vacuum level for bare metal, HOMO and LUMO reprensents the HOME and LUMO level of electrolyte, E_A and E_I represent electron affinity and ionization potential for electrolyte, $V_{WL,I}$ and $V_{WL,O}$ represent vacuum level on both sides (inner side adjacent to metal surface and outer side adjacent to vacuum) of isolated electrolyte. $\Delta\Phi_{intrinsic}$ shows the dipole difference for both sides of isolated electrolyte and ΔE_H is named as

HOMO offset which is a HOMO position relative to metal Fermi level for the system in equilibrium.

4.2.1 Region I: $(\Phi_M \lesssim E_A)$

In order to explain the electronic energy level alignment for this region, I will take (111)-terminated Li artificially constrained to the fcc structure, as a metal electrode and two bilayers thick water film as an

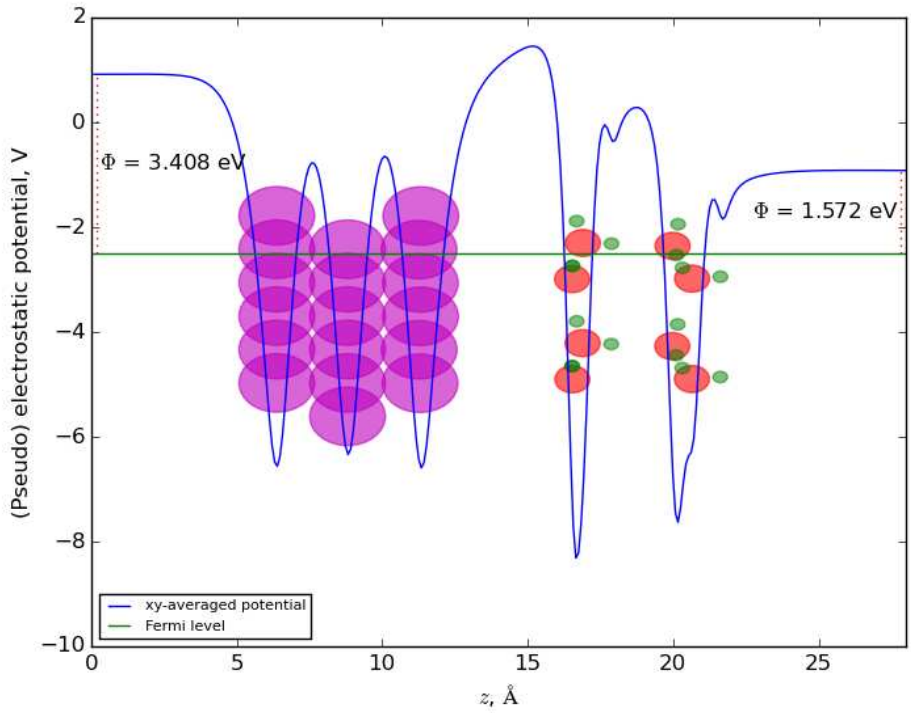

Fig. 4.1: (111)-terminated Li with two bilayer thick water film (H_up structure) as metal-water interface. Electrostatic potential profile is also shown.

electrolyte. For this water film, all out of plane water molecules are pointing away from metal slab, which I have called complete H_up structure in the previous chapter. This electrode-electrolyte system is shown Fig. 4.1. This system is fairly unrealistic as this particular interface is expected to be highly unstable since Li reacts with water. A more relevant example would probably be a metal-oxide contact interface, however, from a discussion point of view, it will serve the purpose here. For this system, the workfunction, which is a measure of electrode potential, cannot be changed by adding hydrogen to the water bilayers. In order to understand, why potential cannot be tuned for this system, we have to go bit deep in the discussion of energy levels at the interface. The energy levels at the interface might result in a significant electronic charge transfer between electrode and electrolyte (but the electrolyte is not

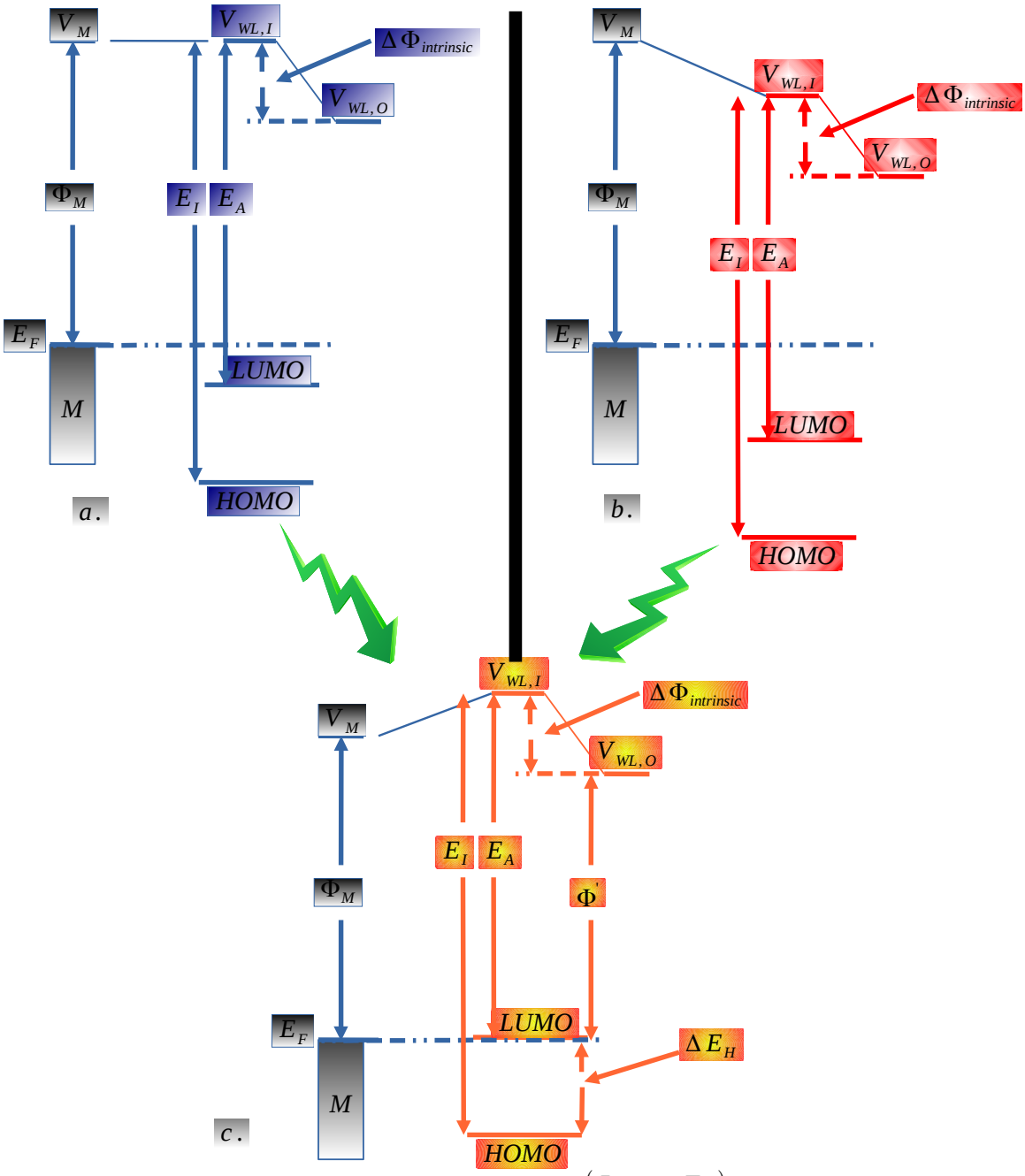

Fig. 4.2: Metal-solution interface belonging to region I $(\Phi_M \lesssim E_A)$. *It shows how two systems end up with the same workfunction despite having different surface charge densities.*

suppose to conduct electrons; an unrealistic phenomenon), so the resulting interface might not be proper electrochemical interface.

The isolated energy levels of metal and solution for such a system before equilibrium will be look like

as drawn on the upper side of Fig. 4.2. The upper left and upper right side Fig. 4.2 shows the electronic energy levels of the system in Fig. 4.1 before equilibrium, without and with added hydrogen to the water bilayer, respectively. We can see clearly that these systems belongs to region I, where $\Phi_M \prec E_A$. If we add hydrogen to the first water layer (for the purpose to change surface charge), then just before equilibration starts, energy levels of the electrolyte will be shifted down relative to metal energy levels as shown in the upper right side of Fig. 4.2 (red background). When these isolated electrode and electrolyte are brought into contact in order to form interface, metal will donate electrons to the LUMO level of the electrolyte during equilibration due to the fact that it has many empty states. It will does so until LUMO will be pinned to Fermi level of metal, so, after equilibrium has been established, the Fermi level will therefore be pinned to states close to the LUMO. Both the system with and without added hydrogen, will result in a similar energy level alignment after equilibrium has been established due to significant charge transfers between metal and electrolyte as shown in the bottom of Fig. 4.2.

Consequently, a change in surface charge density will not affect Φ' much; it stays essentially fixed as it will be given roughly by the constant difference between the LUMO and $V_{wL,O}$, the near-field vacuum level outside the electrolyte. This kind of energy alignment is observed for (111)-terminated Li artificially constrained to the fcc structure, with a two bilayer thick hydrogen-pointing-up water film adsorbed on top [cf. Fig. 4.1]. This system is fairly unrealistic, however, We note that this example gives a clear illustration of the typical Fermi level pinning in region I. DFT's tendency to place LUMO levels too far below the vacuum level could easily result in pinning to LUMO derived states even in systems where this is not supposed to occur. This means that if we somehow know the atomic configurations from experiments, and model our system with the same atomic configurations, even then we are not sure that our system will behave like a true electrochemical interface. Fig. 4.3a demonstrates the response of Φ' to a change in surface charge density for the system belonging to region I, also shown in Fig. 4.1. Here, in contrast to adding hydrogen to the water-bilayer, a change in surface charge density is obtained by explicit injection of fractional charges into the metal slab. As expected, Φ' is almost insensitive to the surface charge density. A small reduction of Φ' might still be observed upon charging of the metal surface due to the slightly increased occupation of the LUMO in the combined system.

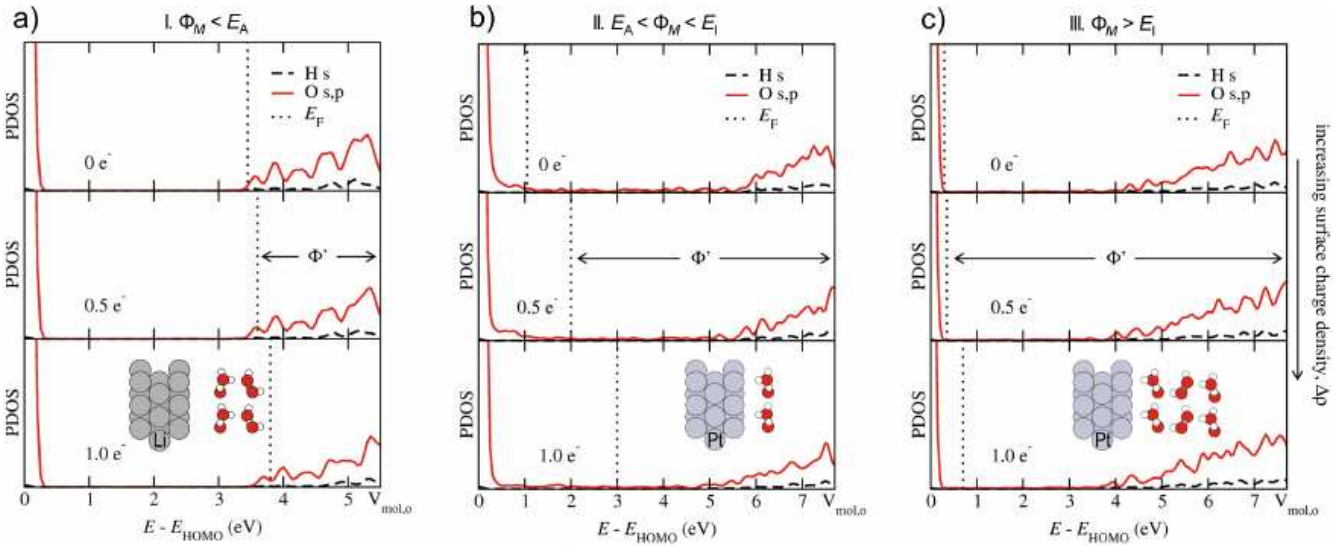

Fig. 4.3: Energy level alignment for the electrode-electrolyte systems belonging to regions I, II and III as a function of surface charge density. Region I is represented by Li-water artifical system with $\Phi_M \approx 3.4\ \text{eV}$, $E_A \approx 5.1\ \text{eV}$. *and* $E_I \approx 7.9\ \text{eV}$. *Region II is represented by Pt-water system with* $\Phi_M \approx 5.6\ \text{eV}$, $E_A \approx 1.2\ \text{eV}$. *and* $E_I \approx 6.4\ \text{eV}$, *and region III is again represented by Pt-water system, but with* $\Phi_M \approx 5.6\ \text{eV}$ *and* $E_I \approx 2.1\ \text{eV}$. *The number of extra electrons added per 12 surface metal atoms, is added in each panel. As a result of the essentially constant HOMO offset in region I and III, a change in surface charge density will not effect the workfunction* Φ'. *However, in region II, HOMO level is not longer pinned relative to the Fermi level and an increase/decrease of the surface charge density will be reflected in a resulting* Φ'.

4.2.2 Region II: True electrochemical interface $(E_A \lesssim \Phi_M \lesssim E_I)$

Fig. 4.4 shows another example of an electrochemical metal-water interface but it falls in this region II. The xy-averaged electrostatic potential (EP) energy has been plotted also for two different proton concentrations. It is seen that an increase in proton concentration, and concomitant increase in surface charge density, reduces the EP energy in the vacuum region outside the electrolyte, relative to the Fermi level; that is, it reduces the work function Φ' which is a measure of the electrode potential[107],[118],[115]. This interface model thus behaves as a proper electrochemical interface and allows the bias to be varied so that electrochemical reactions can be studied at different potentials. The explanation as to why Φ' can be varied in the above system is found in the relative size of the metal work function, Φ_M, compared to the electron affinity, E_A, and ionization potential, E_I, of the electrolyte. So, lets consider the energy levels for such a system, for which the workfunction, which is

a measure of the potential can be tuned.

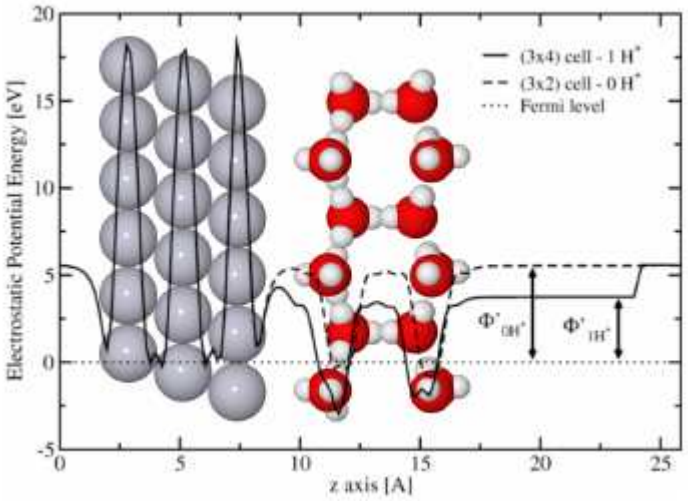

Fig. 4.4: A proper electrochemical Pt-water interface, showing the variation of the electrostatic potential energy averaged parallel to the surface corresponding to the two different proton concentrations.

The isolated energy levels of metal and solution for such a system are shown in Fig. 4.5. The left and right side of Fig. 4.5 shows the energy levels of the system similar to the one shown in Fig. 4.4, without and with the added hydrogen to the water bilayer, respectively. Again, if we add hydrogen to the first water layer (for the purpose to change surface charge), then just before equilibration starts, energy levels of the electrolyte will be shifted down relative to metal energy levels as shown in the right side of Fig. 4.5 (red background). We can see that the model electrochemical interface displayed in Fig. 4.4 belongs to region II $\left(E_A \lesssim \Phi_M \lesssim E_I\right)$ upon vacuum level alignment. For this considered system, $\Phi_M \succ E_A$, which means that the energy cost of removing an electron from the metal is larger than the energy gained by adding it to the electrolyte. Likewise, since $E_I \succ \Phi_M$, the cost of removing an electron from the electrolyte will not be compensated by the energy gained when adding it to the metal. Consequently, there will be no spontaneous charge transfer across the interface when the metal and electrolyte are brought into contact to form the interface and the energy levels of the both systems(with and without added hydrogen) after equilibration will stay more or less at the same level as shown in Fig. 4.5. It also means that no additional dipole will build up at the interface and the metal and

electrolyte vacuum levels will therefore stay aligned upon formation of the interface, as illustrated in Fig. 4.5. As a direct result of the vacuum level alignment, the electrolyte HOMO and LUMO levels straddle the Fermi level in the combined system. For such systems, a subsequent increase/decrease of the charge density on the metal surface, for instance in response to an applied electrode potential, adds an extra contribution $(\Delta\Phi_{polar} = V_M - V_{wL,I})$ to the surface dipole energy, which shifts the electronic energy levels of the electrolyte relative to the Fermi level (see Fig. 4.5 red lines). This shift should be reflected in a corresponding change of Φ' (also indicated by Φ' in red), something that can be verified and quantified by DFT calculations.

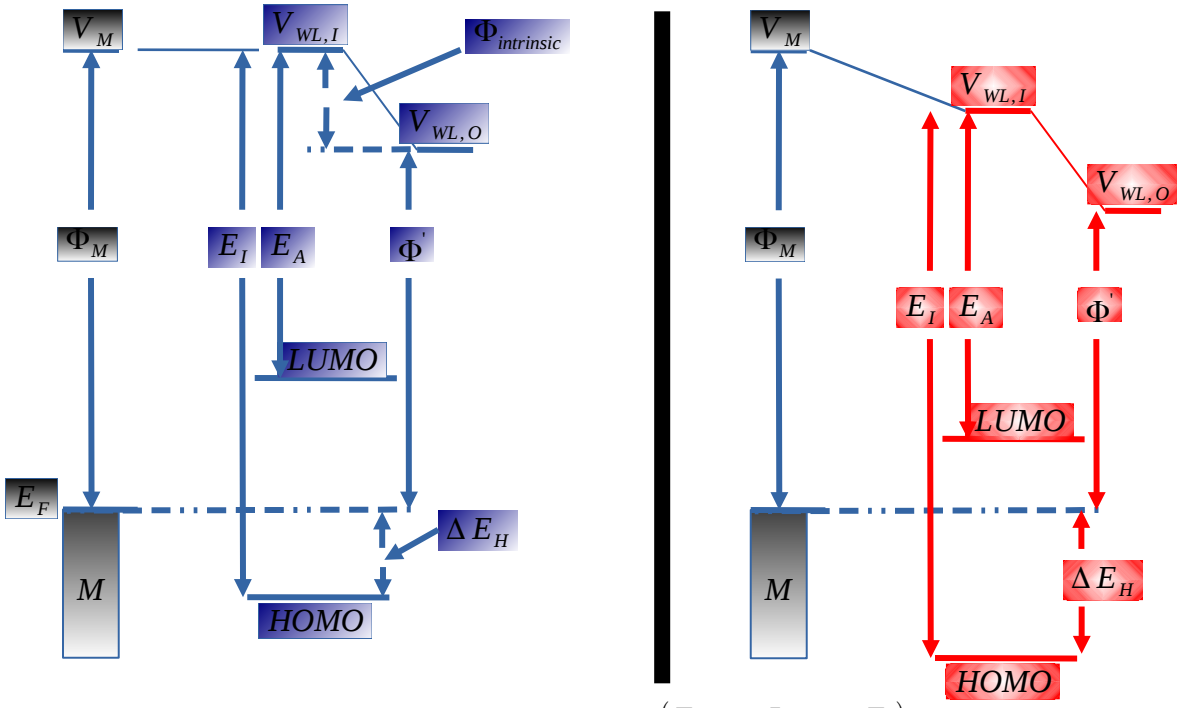

Fig. 4.5: Metal-solution interface belonging to region II $(E_A \lesssim \Phi_M \lesssim E_I)$. *It shows two systems having different surface charge densities will result in different workfunctions.*

Fig. 4.3b demonstrates the response of Φ' to a change in surface charge density for another system belonging to region II, a Pt(111) surface covered with a single water bilayer with complete H_down structure. Here, we have explicitly injected fractional charges into the metal slab in order to have different surface charge density in contrast to Fig. 4.4, where we have added hydrogen. As expected, Φ' depends sensitively on the surface charge density. Addition of 0.5 electrons to the uncharged cell

with 12 surface atoms reduces Φ' with approximately 1 eV, and addition of another half electron reduces it 1 eV further. This is the property of a proper electrochemical interface, where the potential can be changed by changing the surface charge density.

4.2.3 Region III: $(\Phi_M \gtrsim E_I)$

The model electrochemical interface shown in Fig. 4.6 belongs to region III $\Phi_M \gtrsim E_I$. A Pt(111)

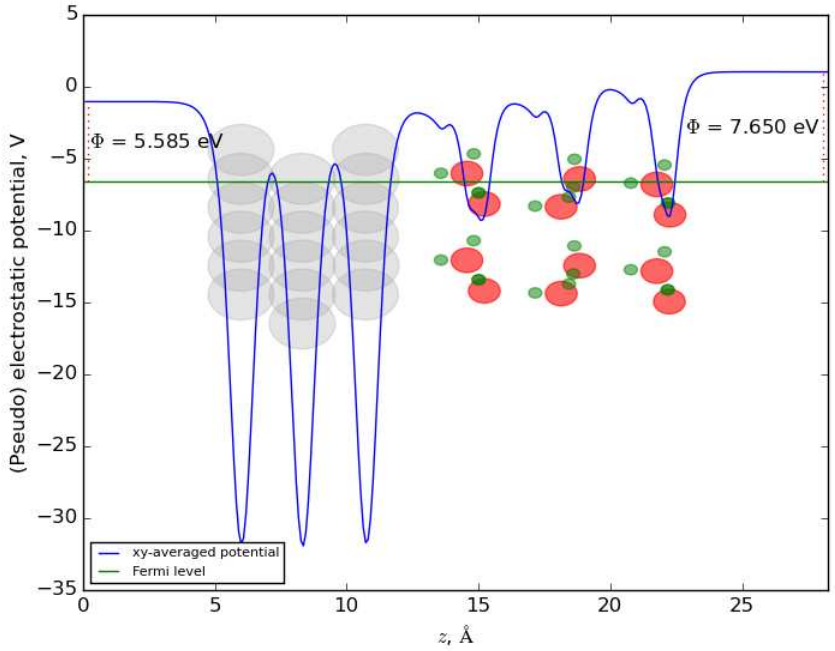

Fig. 4.6: Atomic-scale model of a Pt-water interface belonging to region III. The electrostatic potential energy parallel to the surface is also plotted.

slab with three bilayer thick water film, where all out of plane water molecules are pointing down towards the metal surface (complete H_down structure), is used to define the electrochemical interface. This H_down structure will result in a larger workfunction, even larger than the ionization potential of the electrolyte. I have explained in previous chapter that the workfunction is larger for the systems where the water is pointing towards metal slab (H_down), relative to the one where water is pointing away from the metal slab. Again, similar to the case for region I (although for different reason), potential can not be tuned by adding/subtracting hydrogen to/from the water bilayers. A change in surface charge density will not be reflected in the measured workfunction. It also means that systems

with electrochemical interfaces that fall in this region do not have proper electrochemical interface, so, lets consider the energy levels for such a system.

The energy levels of the isolated electrode-electrolyte for both the systems without and with added proton are shown in upper left and upper right of Fig. 4.7, respectively (blue and red background). We can see that for these system, $\Phi_M \succ E_I$. The added hydrogen will shift the energy levels of the electrolyte relative to metal Fermi level as shown in Fig. 4.7b. When isolated electrode and electrolyte are brought into contact in order to form interface, charge will flow from the HOMO of the electrolyte to the Fermi level of the electrode during equilibration due to the fact that metal have a lot of empty states. The shallow positive states thus created in the electrolyte will pin the Fermi level once the interface has been formed. So, for both the systems, with and without added proton, HOMO will be pinned to the Fermi level after the equilibration has been established. In other words, we will get similar alignment of energy levels for both the systems with and without added hydrogen and both the system will result in a more or less same workfunction. So, for the systems in this region, electronic charge is transferred between metal and electrolyte as was for the systems belonging to region I, electrolyte is again conducting electrons, which is an un physical phenomenon.

We can also re-affirm this conclusion, by explicitly injecting electrons to the metal slab, and hence changing the surface charge density as demonstrated in Fig. 4.3c. As expected, Φ' is almost insensitive to the change in the surface charge density upon addition of 0.5 electrons to the metal. However, upon further charging, the energy levels of the electrolyte will move enough down relative to the metal Fermi level, that HOMO-LUMO gap will tend to straddle Fermi level. This will stop the further transfer of charge at the interface, hence we will begin to observe the change in Φ' as suggested by Fig. 4.3c. However, for the systems belonging to region III, resulting HOMO offset, ΔE_H , which is a HOMO position relative to metal Fermi level for the system in equilibrium is small and virtually unaffected by a change in the surface charge density due to the fact that HOMO is pined to the Fermi level.

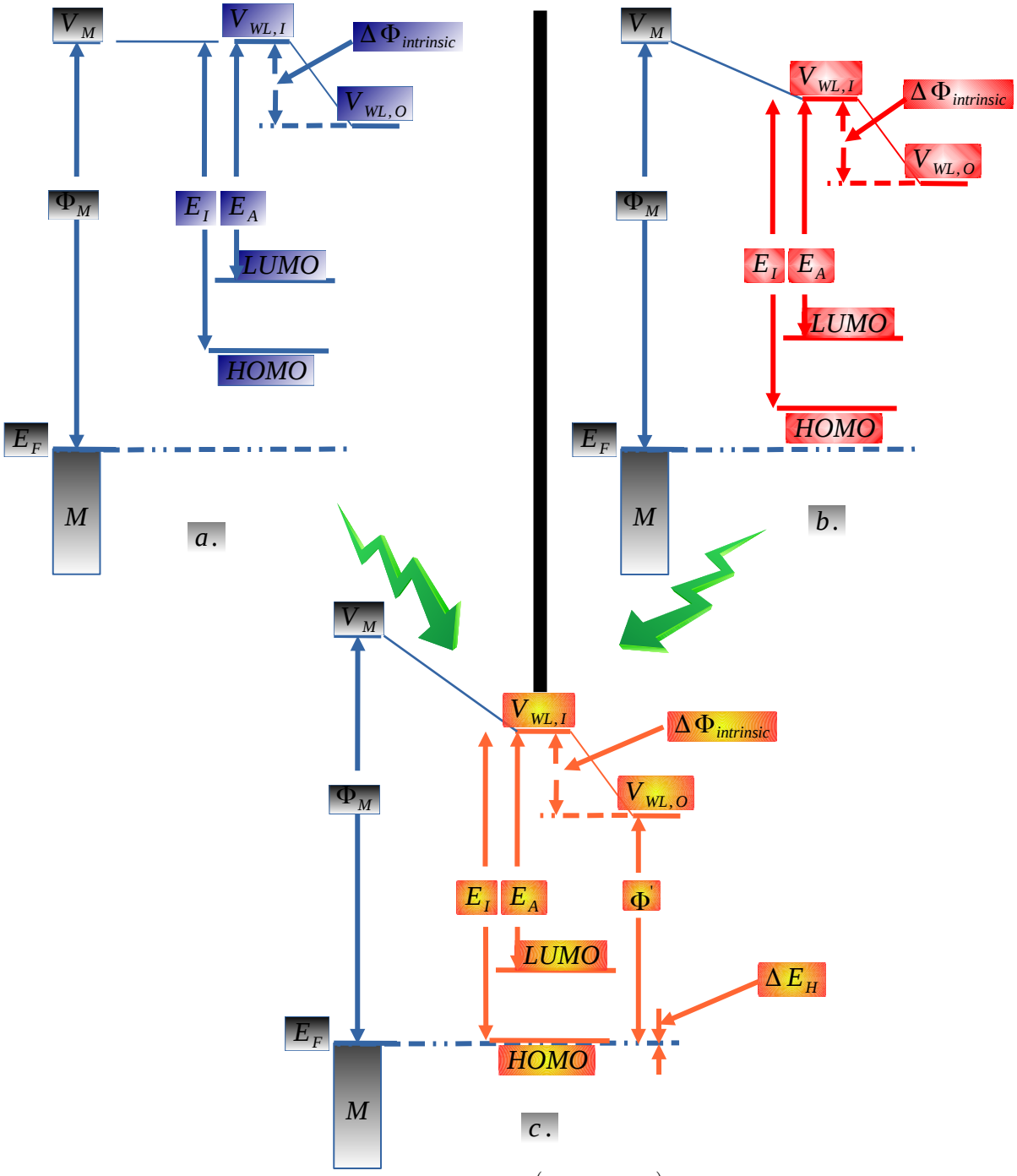

Fig. 4.7: Metal-solution interface belonging to region III $(\Phi_M \gtrsim E_I)$. *It shows how two systems end up with the same workfunction despite having different surface charge densities.*

4.3 Relationship between ΔE_H and $\Phi_M - E_I$

The energy level alignment at interface can be further quantified by more, explicit, electronic structure calculations. Greiner *et al.* recently demonstrated a strong interdependence between ΔE_H and $\Phi_M - E_I$ based on experimental data, in systems of organic molecules adsorbed on metal oxides[126]. Our metal- electrolyte interface (Skúlason's model for the interface) exhibit a similar relationship as shown in Fig. 4.8, which reports ΔE_H *vs.* $\Phi_M - E_I$ for a large set of metal-water interfaces. We have used various metals together with different orientations of water molecules in order to model the electrochemical interfaces. A few metal-oxide (Ni- YSZ) interfaces are also reported.

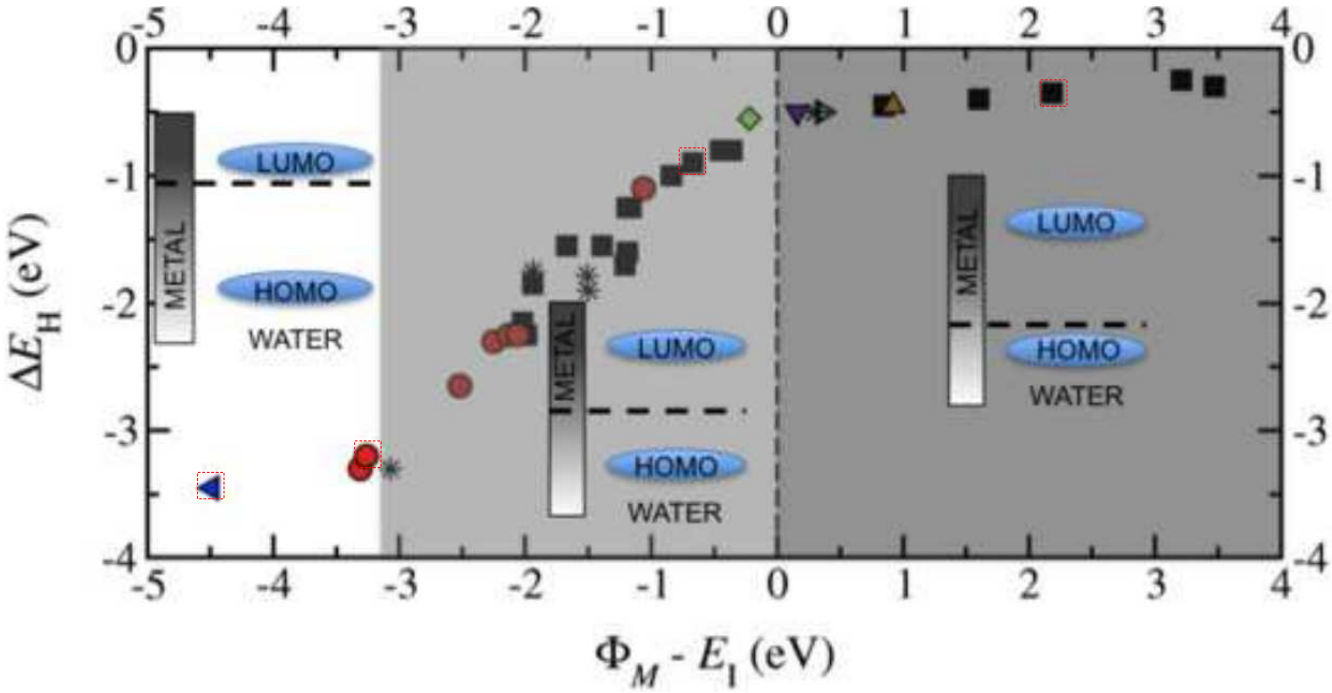

Fig. 4.8: The ΔE_H as a function of $\Phi_M - E_I$, where the data points cover three qualitatively different regimes: I. $\Phi_M \prec E_A$, II. $E_A \prec \Phi_M \prec E_I$ and III. $\Phi_M \succ E_I$. RPBE calculations of (■) Pt-water, (●) Ag-water, (♦) Au-water, (▲) Ir-water, (◀) Li-water, (▼) Pd-water, (►) Re-water, (+) Rh-water, (×) Ru-water and (∗) Ni-YSZ. Only systems in region II are suitable for theoretical studies of potential dependent electrochemical properties.

As suggested already by Fig. 4.2c, Fig. 4.3a and Fig. 4.8, ΔE_H is large in region I, which is roughly equal to the HUMO-LUMO gap due to the LUMO pinning to Fermi level. For the region II, where the

metal Fermi level is straddle by HOMO-LUMO gap (see Fig. 4.5, Fig. 4.3b and Fig. 4.8), ΔE_H , is roughly given by $\Phi_M - E_I$, and varies linearly with a slope of one in this region. Since HOMO is pinning to metal Fermi level in region III, ΔE_H is very small as can be seen from Fig. 4.7c, Fig. 4.3c and Fig. 4.8. The border between region II and III is universal as can be seen from Fig. 4.8, since it is defined by $\Phi_M - E_I = 0,$ but the border between regions I and II is not universal, since it is defined by $\Phi_M \simeq E_A$ and E_A may vary from one electrolyte to another. So, the exact location of border between regions I and II, depends on the particular electrolyte. The width of region II is approximately equal to the HOMO-LUMO gap. If the entire curve in Fig. 4.8 had been mapped out using only one specific electrolyte but different electrodes, covering a large range of Φ_M values, then the width of region II would have been about the same as the HOMO-LUMO gap of that electrolyte. A closer look at Fig. 4.8 revels, that actual border between regions II and III (if defined as the point of transition between a linearly varying and constant ΔE_H) is actually located at a slightly negative $\Phi_M - E_I$, as the cost to remove an electron from the electrolyte and to form an electronically and geometrically fully relaxed state is smaller than measured E_I [113]. For similar reasons, the border between regions I and II will be located to the right of the position suggested by E_A . These effects will further narrow the region II. Nevertheless, despite conventional DFT severely underestimates the width of the HOMO-LUMO gap, we still expect that most Pt-water systems belong to region II in reality.

4.4 PBE vs. RPBE interface charge transfer

At the electrochemical interface, significant charge redistribution is frequently observed when metal-water systems are modeled using PBE (or similar exchange-correlation functional) as shown in Fig. 4.9 [119]. We know that PBE, usually overestimates the binding energies compared to RPBE[127]. Compared to RPBE, PBE yields smaller separation and stronger interaction between metal and water as can be seen from Fig. 4.9. This strong interaction and small separation between metal and electrolyte might sometimes be true electrochemical phenomenon (e.g. hydrogen bonding between adsorbates and electrolyte), however, the relation between ΔE_H and $\Phi_M - E_I$, shown in Fig. 4.8, with a sharp transition close to $\Phi_M - E_I \simeq 0$, holds only as long as the chemical interaction between electrode

and electrolyte is weak [119] . The picture becomes blurred if chemical bonds start forming between them because of the accompanying charge redistribution at the interface[110]. However, in case the strong metal- water interaction is unrealistic, a U term is added to the PBE calculation, and gradually increased, the metal-water interaction will steadily weaken and the metal-water separation will expand

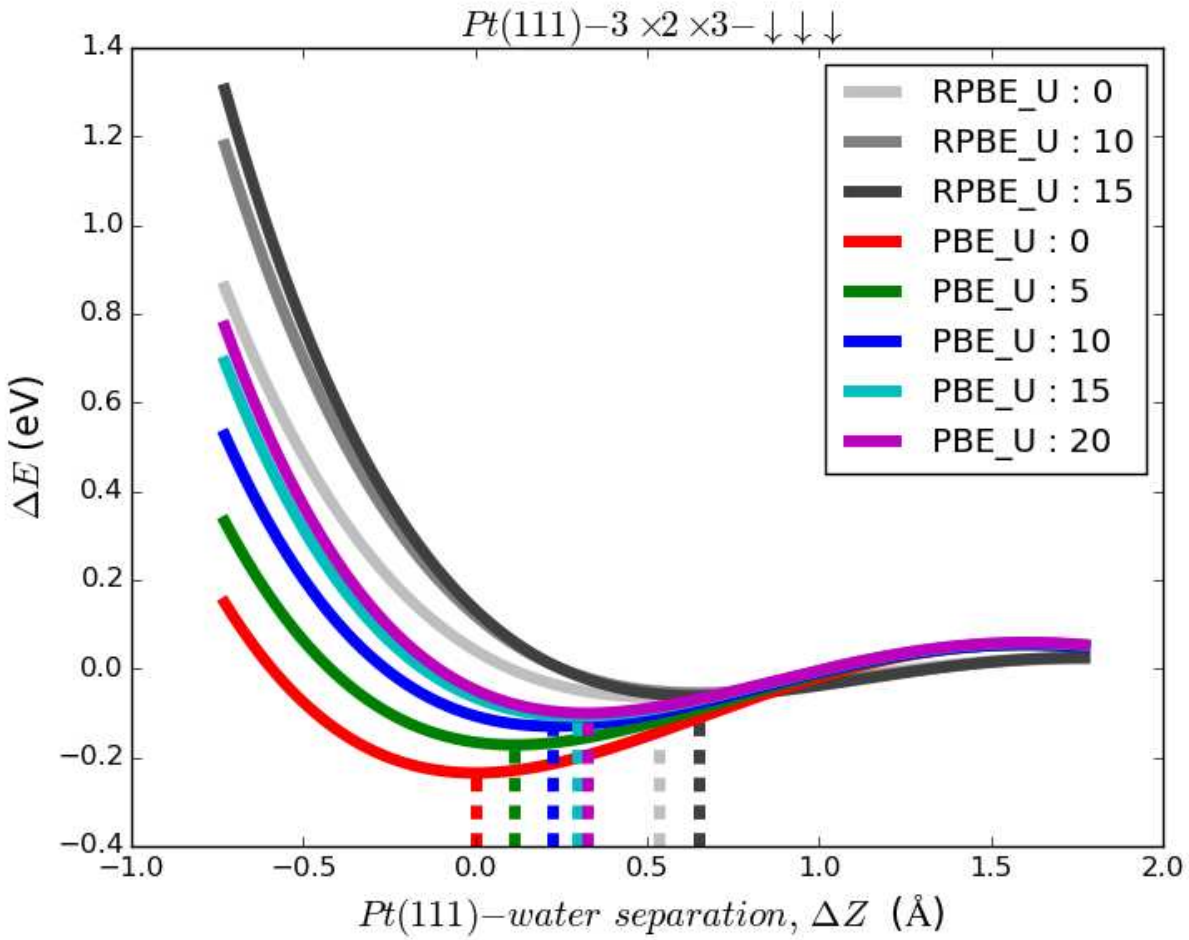

Fig. 4.9: Comparison of metal-water interaction and separation for two exchange-correlation functionals: PBE and RPBE. Vertical dash lines show minima for each curve. The values at x-axis show the extra added/removed separation (Z') compared to fully relaxed structure at U = 0 using PBE. PBE yields strong interaction and less separation compared to RPBE between metal and water, but at hight values of U, it more or less reproduces RPBE results.

as shown in Fig. 4.9. Eventually the distance and interaction will saturate to the RPBE level. So the RPBE results will be more or less recovered using PBE and the main features of the curve in Fig. 4.8 will be reproduced. This means that the artificially high HOMO level in water is directly responsible for many theoretical reports of charge transfer between neutral water films and metals.

4.5 Addressing short-comings of interface modeling:

For the cases (systems in regions I and region III) where Φ' is virtually unaffected by charging, it is possible to change the free energy of a charge transfer reaction without altering the electrode potential. Additionally, a small change in potential can change the free energy of the interface dramatically, so the interface capacitance becomes unrealistically large. An electrochemical model that behaves like that is clearly unphysical. The problem, however, can often be addressed by turning individual dipoles of water molecules in the electrolyte (H-up to H_down or vice versa), so that HOMO-LUMO gap straddles Fermi level. A minor change in the atomic geometry might be enough to shift the systems from regions I and III to region II. Particularly the systems belonging to region I, can often be addressed by flipping the whole electrolyte over z-direction. For example, considering the energy levels in Fig. 4.2, where the system originally belongs to region I. Flipping of the electrolyte, will result in an exchanged values of $V_{wL,O}$ and $V_{wL,I}$, where now aligning the V_M and $V_{wL,I}$ (vacuum levels) will result in a system belonging to region II. However, if the system belong to region III, it can actually still have experimentally correct atomic configuration. It means using an experimentally correct atomic configuration does not guarantee that the system will end up in region II due to the self-interaction problem faced by electrons in standard DFT. So, the necessary requirements on the electronic structure might still not be met due to limitations of DFT and more advanced electronic descriptions eats up a prohibitive number computational resources. So, if one does not like to change the atomic configuration (water dipoles) for some reasons, or he/she is sure about the experimentally correct structure, he/she can use GGA+U calculations.

It is mainly the artificial self-interaction faced by electrons in conventional DFT leading to the HOMO levels of the water films being too high in energy. This high HOMO level will result in a smaller E_I and often even smaller than the Φ_M. DFT might treat the system as this belong to region III $(\Phi_M \succ E_I)$, because the calculated $E_I's$ too small in conventional DFT calculations. For bulk water the discrepancy between DFT[128] and experimental[129] estimates of the HOMO level position is typically several eV and there is similar difference in the estimation of the band gap[108], [130]. This is the reason that experimentally correct atomic structure does not even guarantee that the system will

end up in region II.

In DFT, however, $GGA + U$ calculations[131], [132] can be performed on systems, where the orbital-dependent interactions that push the HOMO down are introduced, so the positioning of the HOMO level can be improved. We have performed $GGA + U$ calculations at the RPBE level for four different metal-water systems belonging to different regions highlighted in Fig. 4.8 (dashed red squares). For each system, five different $U's$, $U \in \{0,\ 5,\ 10,\ 15,\ 20\}$, have been applied to the oxygen-2p orbitals and the results are reported in Fig. 4.10.

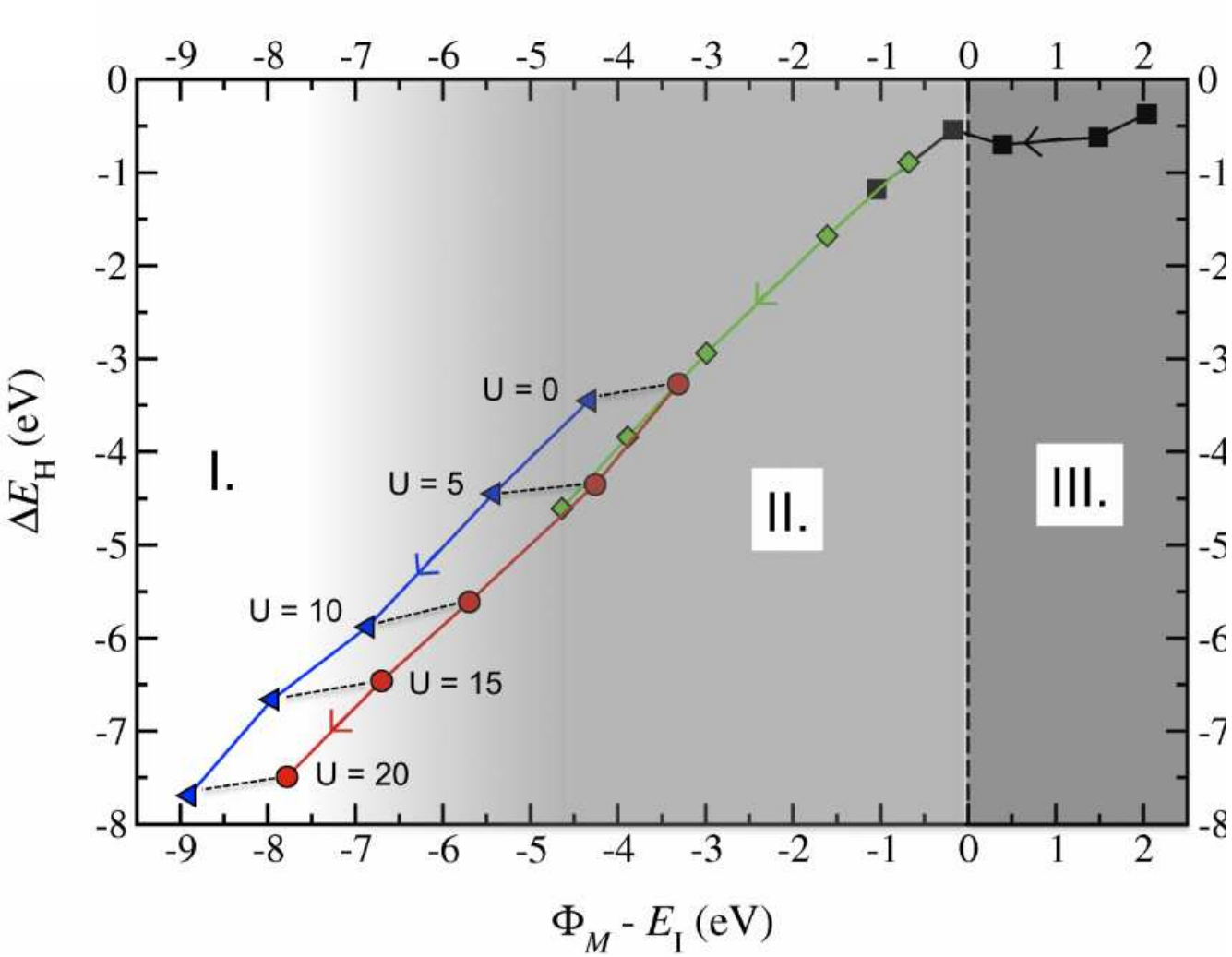

Fig. 4.10: RPBE + U calculations of the four systems highlighted in Fig. 4.8: (■) Pt-dd, (♦) Pt-du, (●) Ag-uu and (◄) Li-uu (d (u) denotes a water bi-layer with a net dipole pointing down (up), toward (away from) the metal surface]. The arrows indicate the translation of the data points when U is increased from 0 to 20 through the set {0,5,10,15,20}.

As the U term in calculations push the HOMO down and increases the HOMO-LUMO gap, so the width of region II will expand, which is roughly equal to the HOMO-LUMO gap. The width of region II will be widen by an equal amount as the change in the HOMO-LUMO gap. For a value of U, which will make $E_I \succ \Phi_M$, the data points which were in region III, can be shifted in region II. The systems originally in region III are mainly Pt based, can moved into region II as a result of the increased ionization potential $(\Phi_M \prec E_I)$ as shown in Fig. 4.10. However, in a real physical system, when the water film approaches the metal, the dynamic image charge effect, not captured by DFT, will move the HOMO level up and the LUMO level down[133]. So in reality the width of region II will be slightly narrow. So, the value of U that positions the HOMO level correctly in water layers far from the metal surface, the $GGA + U$ calculations will likely overestimate the width of region II, since in reality LUMO level will also be bit down due to the image charge effect.

4.6 Summary:

In this chapter, I have explained the alignment of electronic energy levels at metal-water electrochemical interfaces in detail. Three different regimes: LUMO pinning, vacuum alignment and HUMO pinning have been observed. Only vacuum aligned systems, qualify, electronically, as electrochemical interfaces. In particular, we have shown that the HOMO and LUMO levels of the isolated electrolyte have to straddle the Fermi level of the metal electrode in order for the combined system to behave as an electrochemical interface.

As a direct consequence of conventional DFT's notorious under- estimation of the HOMO-LUMO gap of the electrolyte, electrode-electrolyte interface models constructed without special care could exhibit an unphysical charge transfer between the two neutral components. In such systems the key feature of a proper electrochemical interface, a tunable electrode potential, is lost. The spurious charge transfer also has implications beyond electrochemical interface modeling. It affects the calculated work function which could otherwise be used to distinguish between potential adsorbate structures.

Chapter 5 : pH and potential in electrochemical interface modeling

5.1 Introduction:

In chapter 3, I have discussed the two levels of complexity for the simulations of electrocatalysis, the thermochemical level and the level where the interface is explicitly included. The thermochemical simulations address free energy differences between reaction intermediates and ignore the Helmholtz-plane and the field from the interface, which means that this level of simulations are fast to perform[134]. The effect of the potential, relative to RHE reference is simply added a posteriori[135]. However, this framework cannot deal with neither barriers of charge transfer reactions nor the effect of pH. The thermochemistry is independent on pH, that's why the effect of pH per definition not included.

Simulations including the interface can also be divided into two sub level: constant charge and constant electrode potential calculations/constant workfunction calculations, as the workfunction is a measure of the electrode potential[136],[137],[138],[139],[140]. The constant electrode potential calculations are believed to be more realistic, but are also at least an order of magnitude more computational demanding. There are methods to inter- and extrapolate a series of simulation done at constant charge to an analysis of the constant workfunction. This is a major step forward as the series of atomic scale calculations done with a constant number of atoms and electrons can be translated to an analysis of the constant electrode potential. However, it is still not a constant electrochemical potential as the chemical potential of protons is completely ignored. State-of-the art *ab initio* simulations of the metal-solution interface have only focused on the effects of the electrode potential, while the influence of pH has not been addressed.

At constant electrochemical potential, the electrode potential and the pH, both, have to be fixed. It is a great challenge for DFT modeling to do simulations at constant electrochemical potential, where electrode potential (chemical potential of electrons) together with pH (corresponding to the chemical

potential of protons) is considered. The reference very often referred to as the computational standard hydrogen electrode is really not a standard hydrogen electrode but rather a reversible hydrogen electrode reference. No existing approach addresses the effect of pH on the interfacial structure. Electrochemical reaction rates can, however, be strongly affected by solution pH, and there is increasing interest in the development of efficient electrocatalysts for alkaline environments[141], [142],[143],[144]. Consideration of pH is thus a crucial challenge in *ab initio* simulations.

5.1.1 Fundamental challenge:

The fundamental challenge is that DFT simulations presently are limited to system sizes of ~1000s of atoms. The number of charge carries per water unit is so small that even at pH=0 (1 molar of additional protons) it takes 55 water molecules to get the corresponding concentration for just one proton in bulk water. As the pH scale is exponential there is no hope to address pH of bulk water at anything near neutral conditions by directly modeling the water molecules. We need 550 million water molecules for just one proton in bulk water in order to explicitly simulating the bulk solution for the pH = 7, which is quite unrealistic. Furthermore, pH's influence on energy is entropic and it is very computational demanding. In bulk water many structure configurations are close to equal in energy and therefore many of them are needed to calculate the partition function. However, we can circumvent these difficulties where a Helmholtz metal-solution interfacial model is valid, i.e. highly charged interfaces and/or concentrated solutions.

5.1.2 Solid-liquid interfaces:

Fortunately, the solid/liquid interface might be easier than bulk water. The protons/hydroxyl (H^+/OH^-) and H*/OH* (adsorbed on surface) interact strongly with each other and with the conducting electrode. The difficulty in explicitly simulating the bulk solution and the corresponding entropic effects with DFT can be avoided due to the strong interaction. The strong interaction with the electrode has the consequence that a big part of the solvation energy is taken care of by the electrode. This means that less water molecules are needed in the simulations. The strong interaction between the charge-carries

means that the free energy is dominated by enthalpy, the entropy from rotation and translation is relatively small. The vibrational degrees of freedom can easily be included. In other words: the ground state structure is > O(*KT*) lower in energy than those of excited states and therefore it dominates the partition function. With surface and bulk protons at electrochemical equilibrium, i.e. $\mu_{H^+ + e^-} = \mu_{H^+(bulk) + e^-} = \mu_{H^+(surf) + e^-}$,the entropic contribution to free energy in solution is mostly translated into enthalpy at the interface. What is entropy in bulk water is mainly enthalpy at the interface. Furthermore, the field of the charged interface is virtually fully screened by 1-2 water layers for system sizes treatable with DFT [136] . This leaves hope that it is possible to model the solid-liquid interface at realistic concentrations of charge carriers and get accurate free energies by only considering the ground state structure (including the hessian if the vibrational entropy is important) within the system sizes that can be treated with DFT.

Skúlason et. al. have developed a method keeping the electrode potential constant relative to the reversible hydrogen electrode [141]. In this chapter, however, I will explain a method to get a constant electrochemical potential relative to both the standard and the reversible hydrogen electrode. I will explain the method for obtaining results for *ab initio* simulation at constant electrochemical potential and thereby opening the studies of the pH effect at the quantum mechanical level. This is solely based on thermochemical arguments where the dipole of the simulated interface is controlling the pH. We limit the analysis to a Helmholtz model of the interface. Temperature is only included in the free energies, the structure of the water is only allowed to relax to the local energy minimum meaning that it is an ice-like structure. This is to our knowledge the first time pH is included in analysis of atomic scale simulations. This opens for *ab initio* simulations for studying the effect of pH on structures and electrocatalytic activity of electrochemical interface.

5.2 The computational reversible hydrogen electrode reference*:*

I have discussed in chapter 2, the theoretical standard hydrogen electrode (SHE) in some detail, which depends on the pH. Here, I will just review the theoretical reversible hydrogen electrode (RHE), which is actually the same, but pH independent. The relation between these two will be clear soon. The zero

point of the reversible hydrogen electrode is defined by the equilibrium of equation (5.1) at an arbitrary pH. It means that this reaction (5.1) is in equilibrium at O V vs. RHE.

$$\frac{1}{2}H_2(g) \quad \Leftrightarrow \quad H^+(aq) + e^- \tag{5.1}$$

The reversible hydrogen electrode is independent on pH. Reaction free energies at zero potential vs. RHE for any reaction involving the same number of protons (H^+) and electrons (e^-) can be calculated by substituting the free energy of the proton and electron pair ($H^+ + e^-$) by the free energy of half a hydrogen molecule in gas-phase. The reaction energy will therefore be independent on pH as the change in chemical potential of the proton taking part in the reaction is balanced by an equal change in the reference. The reaction free energy at finite potentials vs. RHE can be calculated simply by equation (5.2).

$$\Delta G(U_{RHE}) = \Delta G(0_{RHE}) - eU_{RHE} \tag{5.2}$$

In this way the thermochemical reaction free energies can be calculated with reference to gas phase molecules instead of ions in solutions. This is an extremely powerful approach within DFT simulations of electrocatalytic process, since it often only takes a few simple calculations of the adsorbed intermediates to map out the reaction free energies for the relevant range of potentials. The limitation is, however, as we know that barriers for the actual charge transfer reactions cannot be addressed. It is also important to note that pH is not included as protons and electrons ($H^+ + e^-$) are treated together. The thermochemical reaction free energies were considered pH independent, whereas the reaction barriers probably depend on pH. Only considering reaction free energies, therefore peer definition means that pH is not part of the analysis, whereas in order to calculate barriers the solid/liquid interface has to be explicitly included in the simulations.

5.3 Born-Haber Cycle:

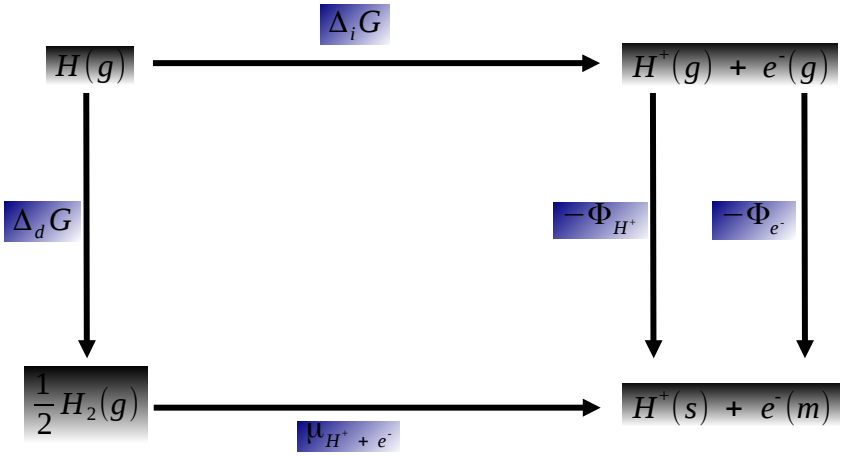

Fig. 5.1: The Born-Haber cycle for hydrogen oxidation. adapted from [137].

Now let's review the Born-Haber cycle for hydrogen oxidation. Consider the free energies of the Born-Haber cycle[145] shown in Fig. 5.1, which gives the relation among electrode potential U, pH and the electrochemical potential of protons and electrons, $\mu_{H^+ + e^-}$. With the chemical potential of $H_2(g)$ as the zero reference point, the free energy of the reaction can be written as

$$\mu_{H^+ + e^-} = \Delta_d G + \Delta_i G - \Phi_{H^+} - \Phi_{e^-}, \tag{5.3}$$

where $\Delta_d G$ is the dissociation energy for dissociating $\frac{1}{2}H_2(g)$ and $\Delta_i G$ is the ionization energy for ionizing $H(g)$, and Φ_{H^+} and Φ_{e^-} are the respective workfunctions of proton (H^+) in solution and electron (e^-) in metal, measure with respect to vacuum just outside the solution phase. If vacuum far from the electrode surface is used the energies are actually not well defined.

Now, lets consider the equation (5.1) is in equilibrium at zero potential with respect to reversible hydrogen electrode (RHE) potential. The RHE potential corresponds to electrochemical equilibrium, $\mu_{H^+ + e^-} = 0$, at arbitrary pH, so equation (5.3) at RHE potential becomes

$$0 = \Delta_d G + \Delta_i G - \Phi_{H^+} - \Phi_{e^-}, \tag{5.4}$$

where the dissociation energy, $\Delta_d G$ and the ionization energy, $\Delta_i G$ are both independent of pH. It follows that the sum of Φ_{H^+} and Φ_{e^-} will also be constant in order to meet the equilibrium condition in equation (5.1). However, we know that Φ_{H^+} depends linearly on pH with the slope of $-K_B T \ln(a[H^+])$, which is 0.059 eV/pH at room temperature and standard pressure. So, the proton solvation energy or the proton workfunction can be expressed as

$$\Phi_{H^+} = \Phi^0_{H^+} + 2.3 K_b T * pH, \tag{5.5}$$

where K_b , T and $\Phi^0_{H^+}$ are the Boltzmann's constant, temperature and proton solvation energy (or workfunction) at pH = 0, respectively. So, as the pH changes, proton solvation energy, Φ_{H^+} , changes and electron workfunction Φ_{e^-} , will therefore changes with the same, but opposite value peer pH. As pH increases, the energy moves from being related to the chemical potential of the electron to being associated with the solution energy of the proton.

5.4 Addressing pH and potential

Now, if we consider the standard hydrogen electrode (SHE) conditions, which is a special case of RHE with pH=0. The corresponding workfunction, $\Phi_{e^-}(SHE)$, of the SHE interface has an experimentally determined value of 4.44 eV [137].

$$\Phi_{e^-}(SHE) = \Delta_d G + \Delta_i G - \Phi^0_{H^+} - 2.3 K_b T * 0, \tag{5.6}$$

$$\Phi_{e^-}(SHE) = \Delta_d G + \Delta_i G - \Phi^0_{H^+}, \tag{5.7}$$

Now we can put back this constant in equation (5.3), in order to re-write the electrochemical potential of proton and electron simply in terms of $\Phi_{e^-}(SHE)$, pH, and Φ_{e^-} as shown in equation (5.8).

$$\mu_{H^+ + e^-} = \Phi_{e^-}(SHE) - 2.3 K_b T * pH - \Phi_{e^-}, \tag{5.8}$$

So, for any metal-solution interface, if we know the workfunction (Φ_{e^-}), and the electrochemical potential of proton and electron $(\mu_{H^+ + e^-})$, which are easy to calculate, then by using the experimental value for $\Phi_{e^-}(SHE)$ the corresponding pH can also be calculated via equation (5.8). For any metal-solution interface, if unit cell is large, $\mu_{H^+ + e^-}$ can be estimated by calculating the differential energy of $H^+ + e^-$ as described in equation (5.9). Where n is the number of hydrogen atoms, N is the number of metal surface atoms, G(n, N) is the free energy of the system of interest, and G(n+1, N) is the free energy of the system with extra added hydrogen in the water structure, and $G_{H_2(g)}$ is the free energy of half a gas phase hydrogen molecule.

$$\mu_{H^+ + e^-} = G(n+1, N) - G(n, N) - \frac{1}{2} G_{H_2(g)} \tag{5.9}$$

It is important to note that $\Phi_{e^-}(SHE)$ is really a work function of the SHE and it is independent on the electrode material. This fix point makes it possible to get an absolute scale and link a work function to potentials vs. SHE. The electrode potential, U, which is determined by the dipole of the interface in the computational model, is directly proportional to Φ_{e^-} and relative to SHE reference, it can be written as shown in equation (5.10) [137],[146].

$$U_{SHE} = \frac{\Phi_{e^-} - \Phi_{e^-}(SHE)}{e} \tag{5.10}$$

Now, by using the equation (5.8), we can deduce the relation between potential vs. RHE reference (U_{RHE}), and potential vs. SHE reference, which is given by equation (5.11).

$$U_{SHE} = U_{RHE} - 2.3 K_b T * pH \tag{5.11}$$

5.4.1 Pourbaix Diagram for Pt(111)

For any metal-solution interface with n hydrogens (as protons and electrons or as adsorbed hydrogen), N surface metal atoms, and workfunction Φ_{e^-}, the free energy per surface metal atom at electrochemical equilibrium can be calculated as

$$G^{\text{int}}\left(\mu_{H^+ + e^-} = 0,\ \Phi_e^-\right) = \frac{G(n,N) - G(0,N)}{N} - \frac{1}{2}\frac{n}{N} G_{H_2(g)} \tag{5.12}$$

where G(n, N) is the free energy of metal-solution system of interest, G(0, N) is the free energy of a reference system with no ions nor adsorbates, and $G_{H_2(g)}$ is the free energy of gas phase hydrogen molecule at standard conditions. The reference system was taken to be a bare slab with water layer(s)of neutral dipole orientations. The neutral dipole orientation can be obtained by having an equal amount of H_up and H_down water orientations in the water structure. All these quantities are straight forward to obtain via DFT and using standard tables. Some of the reported calculation in this chapter were performed using Dacapo instead of GPAW code, integrated with the Atomic Simulation Environment [147],[148],[149],[150]. However, RPBE functional was used for exchange and correlation[151]. To obtain free energies, G, the zero point energies and entropies of proton and adsorbed hydrogen were taken from ref [135, 141]. If OH^- and/or OH* are present, n can be negative. The free energy per surface metal atom for the non-equilibrium case is given by

$$G^{\text{int}}\left(\mu_{H^+ + e^-} \neq 0,\ \Phi_e^-\right) = \frac{G(n,N) - G(0,N)}{N} - \frac{1}{2}\frac{n}{N} G_{H_2(g)} - \frac{n}{N}\mu_{H^+ + e^-}, \tag{5.13}$$

where $\mu_{H^+ + e^-}$ can be calculated with equation (5.9) which will ultimately give us the pH for that metal-solution interfacial structure by using equation (5.8). Nothing is pre-assumed about G(n, N) and G(0, N) in equation (5.13) and that's why his analysis is general and it places no restrictions on the considered atomic interface model. Any atomic scale simulations of the electrochemical interface must

include this analysis in order to explicitly and correctly account for potential and pH. With surface and bulk protons at electrochemical equilibrium, $\mu_{H^+(bulk)+e^-} = \mu_{H^+(surf)+e^-}$, we can avoid the bulk electrolyte modeling and can consider the limited number of water bilayers, provided that they fully screen the interface electric fields [136],[152].

In order to demonstrate the application of the above scheme, we apply it to a variety of Pt(111)-water interfacial structures and then determine the corresponding Pourbaix diagram. In order to construct the Pourbaix diagram, we need to collect the ground state metal-solution interfacial structure as a function of pH and potential. At any given Φ_{e^-} and $\mu_{H^++e^-}$ (or pH), a representative set of interfacial structures of varying charge density, adsorbate coverage and water dipoles should be considered. Therefore, we consider 1–2 water bilayers of ice-like hexagonal water structures [136],[140],[153] of a range of dipole orientations, adsorbate coverages (Had-covered, bare Pt, a 1/2 dissociated water layer), and H^+ concentrations. All model systems were charge neutral, such that the positive charge of the protons was balanced by a negative surface charge on the metal. The total number of systems was limited to ~110. Ideally, many more structures should be calculated to sample the corresponding partition function. An extended set of potentially relevant structures could be generated by performing molecular dynamics simulations, starting from different low energy structures. This is however beyond the scope of the present study, since the focus of the present work is on the illustration and formulation of method concepts, and not on the detailed simulation of the Pt(111) Pourbaix diagram.

For the construction of the Pourbaix diagram, the value of $\mu_{H^++e^-}$ was not calculated explicitly for the equation (5.13). The value of G^{int} was linearly extrapolated for varying $\mu_{H^++e^-}$ at a calculated Φ_{e^-} of the corresponding interface structure. Fig. 5.2 shows the difference in the extrapolation scheme of the present work (Fig. 5.2a, blue arrows) and the computational hydrogen electrode (Fig. 5.2b, green arrows)(same as RHE) [135]. Computational hydrogen electrode calculations do not consider the Φ_{e^-} and value of G^{int} is extrapolated along $\mu_{H^++e^-}$ in order to account for the potential, which is given by, $\mu_{H^++e^-} = -eU_{RHE}$. So, the physical interface dipole was not used to calculate the potential, but the effect of the potential is only considered a posteriori. Therefore, impact of the

adsorbate interactions with the field and water was not considered while calculating G^{int}.

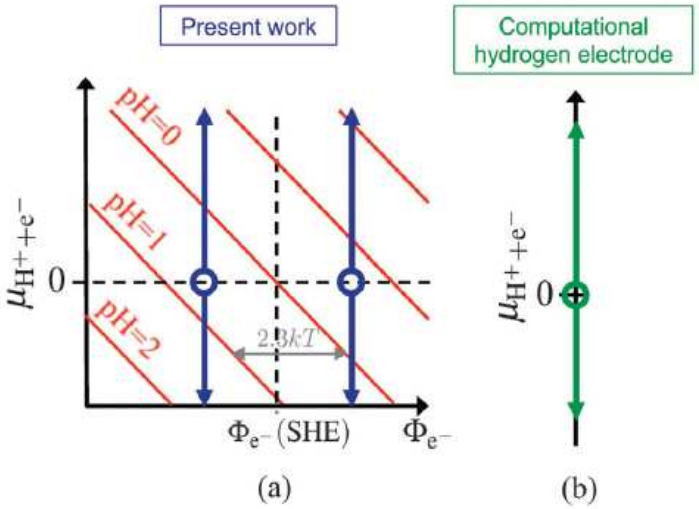

Fig. 5.2: Extrapolated G^{int} vs. $\mu_{H^+ + e^-}$ (a) for the present work in blue arrows, where Φ_{e^-} is determined explicitly by the interfacial structure, red iso-pH lines are also shown for plane $(\Phi_{e^-}, \mu_{H^+ + e^-})$ (b) for CHE (RHE) in green arrows, where Φ_{e^-} is not considered [135].

Fig. 5.2a shows the relationship between Φ_{e^-} and $\mu_{H^+ + e^-}$ as related by equation (5.8). The iso-pH lines are also plotted in red on the $(\Phi_{e^-}, \mu_{H^+ + e^-})$ plane. Fig. 5.2a illustrates the extrapolation of two interface structures, having different Φ_{e^-}, on the $(\Phi_{e^-}, \mu_{H^+ + e^-})$ plane shown by the blue arrows. One can see that the extrapolations are performed at constant Φ_{e^-}, i.e. the variations in $\mu_{H^+ + e^-}$ are due to the change in pH. The workfunction, Φ_{e^-}, is calculated explicitly from the interface dipole and kept fixed while extrapolating G^{int} on the $(\Phi_{e^-}, \mu_{H^+ + e^-})$ plane. This approach, therefore distinguishes contributions of potential and pH to $\mu_{H^+ + e^-}$. Water structures and electric fields that are consistent with the pH and potential are automatically included.

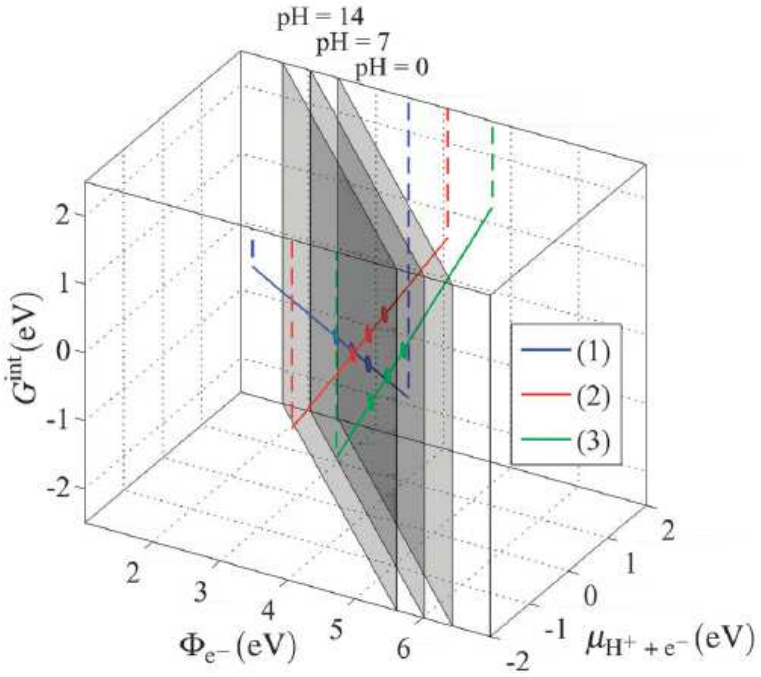

Fig. 5.3: Extrapolated G^{int} vs. Φ_{e^-} and $\mu_{H^+ + e^-}$ for Pt(111)-solution interfacial structures: (1) Φ_{e^-} = 3.48eV, n/N = 0.98, (2) Φ_{e^-} = 4.06eV, n/N = -0.22, (3) Φ_{e^-} = 4.72eV, n/N = -0.44. Dashed lines are shown as guides for the eye. Intersections of G^{int} with constant pH = 0, 7, 14 planes are marked with circles, indicating G^{int} at those particular pH.

The extrapolated G^{int} for the three sample Pt(111)-water structures is shown in Fig. 5.3. At the three corresponding Φ_{e^-}, G^{int} was linearly extrapolated at varying $\mu_{H^+ + e^-}$ with slope n/N as related in equation (5.13). Constant pH planes are mapped out perpendicular to the $(\Phi_{e^-}, \mu_{H^+ + e^-})$ plane as related by equation (5.8). Intersections of the 3 lines with the pH planes are highlighted with flat circles, making the G^{int} of the 3 structures at those particular pH and $\mu_{H^+ + e^-}$ values.

The projections of G^{int} for the full set of metal-solution interface structures onto pH = 0 and pH = 14 planes are shown in Fig. 5.4a and Fig. 5.4b, respectively. The potential against SHE (U_{SHE}) and RHE (U_{RHE}) are shown along the bottom and top x-axes, respectively. The dipole orientation of the water structure is also mentioned in the legend, H_up water dipole is indicated by ↑ and H_down water dipole

is indicated by ↓. Many of the minimum G^{int} structures are > O(KT) ~ 0.026eV lower in energy than those corresponding to the excited states, which suggest they dominate in the partition function.

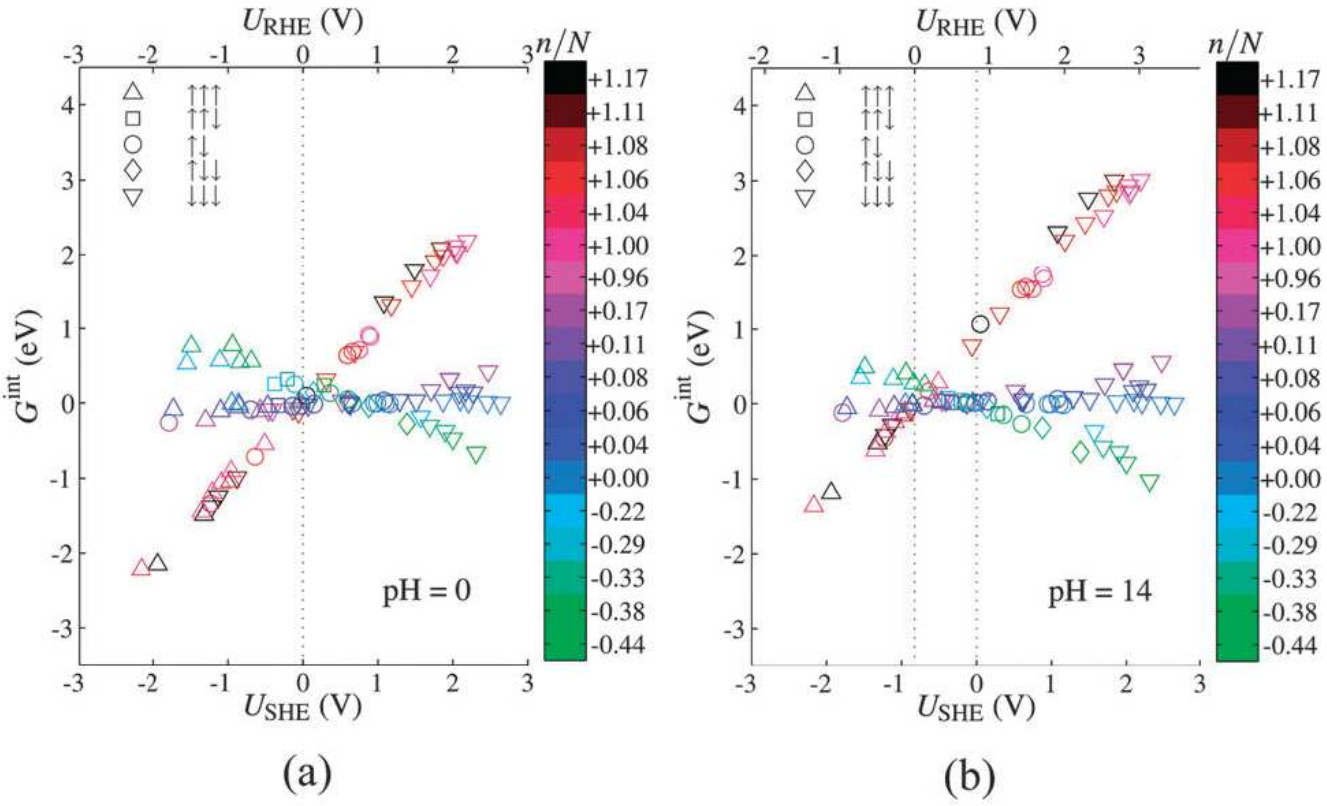

Fig. 5.4: Calculated G^{int} vs. *U* (vs. U_{SHE} and U_{RHE}) for all considered Pt(111)-solution interfacial structures, as projected onto (a) pH = 0 and (b) pH = 14 planes. The arrows in the legend show water dipole and the coverage, n/N, is indicated by the color bar.

We can collect the ground state structures at corresponding pH and potential in the Pourbaix diagram.

Ground state energy structures at selected proton/adsorbate coverages, n/N = -0.33, 0, 0.17, 1, 1.17, are collected in a Pourbaix diagram in Fig. 5.5, showing the variation of coverage and water orientation as a function of U_{SHE} and *pH*. For these coverages, both the G^{int} and the dipole orientation are linearly interpolated for U_{SHE} and *pH* = 0 and 14. Then for every value of U_{SHE} and *pH*, the most stable structure is collected in Pourbaix diagram. Simulated Pourbaix diagram suggests that Increasing U leads to a shift from a H_{ad} to OH_{ad} covered surface, which is consistent with experimental cyclic voltammograms and Pourbaix diagrams [154],[155]. The -2.3kT/pH ~ -0.059eV/pH slope in the dotted lines dividing

regions of different coverages show the expected U_{RHE} dependence of adsorbate coverages. The U_{RHE} dependence is also reflected in Fig. 5.4, where the crossing of the high (H_{ad}-covered) and low (OH_{ad}-covered) n/N points occur at $U_{RHE} \sim 0$V.

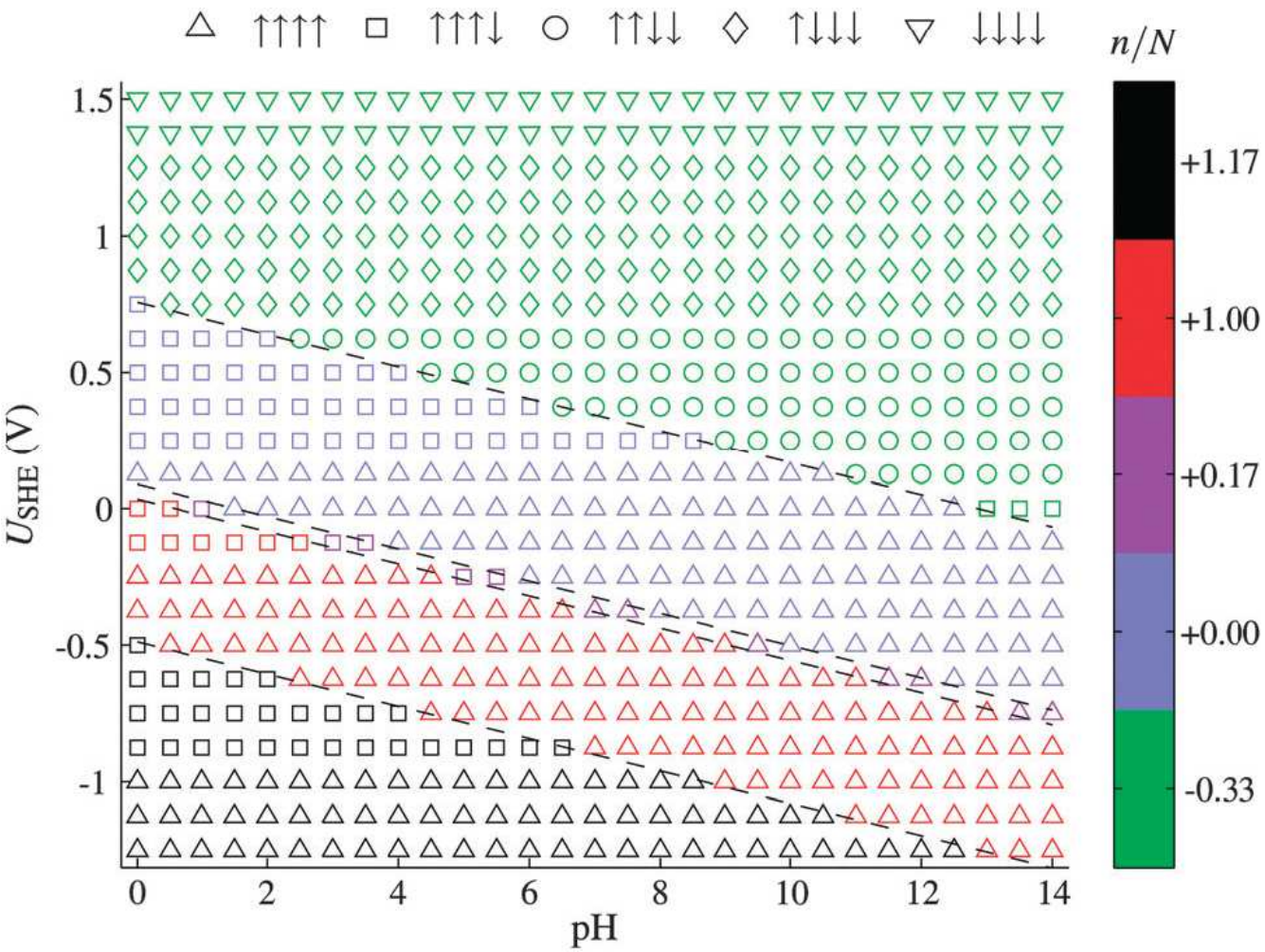

Fig. 5.5: Simulated Pourbaix diagram for Pt(111), showing the minimum energy structures as a function of pH and U_{SHE} for selected coverages, n/N. Dotted lines dividing regions of different coverages have a -0.059eV/pH slope, indicating the expected U_{RHE} dependence of adsorbate coverage.

Generally, as U increases, surface transitions from H_{ad} covered to OH_{ad} covered, and the water orientation also tends to shift from H-up to H-down in order to maximize the hydrogen bonding between the adsorbates and water layer [156],[157]. Water reorients from H-down to H-up as pH increases. At low pH, H's tend to point toward the Pt surface, away from the bulk electrolyte with high proton concentration. This trend is in agreement with that suggested by impedance spectroscopy[158].

In essence, the above analysis elucidates how U and pH affect the metal-solution interfacial structure. The electrochemical potential of proton and electron, $\mu_{H^+ + e^-}$, both are essential in order to determine the ground state interfacial structure. Any U can be set up by a variety of adsorbate coverages, surface charge densities, and water dipole orientations. The *pH or the electrochemical potential of protons* picks out the relevant minimum energy structure for a given U. The workfunction calculated with DFT is usually associated with a slight error, which introduces an uncertainty in the exact position of the system relative to U_{RHE} and U_{SHE}. Accounting for this error will move the system along its corresponding coverage line in Fig. 5.4. However, it will not change the trends observed in Fig. 5.5, it could change the potential at which certain coverage or water orientation starts to dominate. The precision of the method strongly correlated with DFT accuracy, but in any case, the trends allow us to at least distinguish between acidic, neutral, and alkaline conditions.

This new insight into the effect of pH on the interfacial structure does not necessarily invalidate past thermochemical studies. As long as electric fields and hydrogen bonding with water have little or no effect on adsorbate free energies, the previous conclusion remains valid [134],[159]. In this case, for a given adsorbate coverage, only differences in the water orientation contribute to the variation of G^{int} with Φ_{e^-}, and such contributions are negligible compared to those of adsorbate binding energies. This can be understood by considering how G^{int} varies with $\mu_{H^+ + e^-}$ and Φ_{e^-}. Usually a computational RHE reference was assumed, so that reaction free energies were extrapolated as a function of U, $f(-eU_{RHE})$, along a constant pH plane, instead of as a, $f(\mu_{H^+ + e^-})$ along a constant Φ_{e^-} plane, as done in Fig. 5.3. However, field and water structure-independent adsorption energies depend only on $\mu_{H^+ + e^-}$ and not on Φ_{e^-}, i.e. $G^{\mathrm{int}} \approx f(\mu_{H^+ + e^-}) = f(-eU_{RHE})$. This leads to a simple U_{RHE} dependence of adsorbate coverage, as is the case for H_{ad} and OH_{ad} on Pt, considered above. G^{int} obtained via a computational hydrogen electrode and the present extrapolation (cf. Fig. 5.2a) would then be very similar. Therefore, while the water structures considered previously, were likely not consistent with ground state structures at the assumed pH and U, the calculated free energies would still remain a good approximation. Where adsorbates are highly affected by field and/or water structure, e.g. adsorbates with substantial dipole moments, and/or where adsorbate coverages do not show a simple

U_{RHE} dependence[160], the present analysis is required.

As the Pourbaix together with impedance spectroscopy suggest that water structure at the interface might change with the change in *pH*. So, while studying reaction barriers, pH can have an important effect as the charge transfer barriers may be highly dependent on the metal-solution interfacial structure. The ground state structures determined above could, for instance, explain the dramatically higher rates of hydrogen evolution on Pt in acidic solution than in basic ones[139],[138]. At relevant electrode potentials and low pH, some water molecules have H_down structure where the hydrogen point toward the surface, which results in a very small barrier for proton transfer. At higher pH, the complete H_up, where hydrogen point away from the surface, as suggested by the Pourbaix diagram, may gives rise to an extra barrier required for reorientation for proton transfer.

5.5 Summary:

In this chapter, I have presented the scheme to correctly account for potential and *pH* in the *ab initio* calculations. I have explained a novel generalization of the computational hydrogen electrode to explicitly capture the respective *pH* and potential effects on the interface structure and its corresponding free energy. Based on the simple thermodynamic arguments, the method determines ground state interface structures as a function of *pH* and potential.

The only required inputs to the method are the electronic workfunction and the integral free energy for any interfacial structure containing any reaction intermediate of interest. The electronic workfunction and the integral free energy, both, can be easily calculated using standard DFT. As an example, the method was applied to a set of Pt(111)water structures in order to determine the corresponding Pourbaix diagram. The Pourbaix suggests that water structure at the interface might change with *pH*, so *pH* is expected to have an important impact on charge transfer barriers. This method opens up the possibility for theoretical studies of pH effects on the structure and electrocatalytic activity of electrochemical interfaces.

Chapter 6 :Influence of the Electrochemical Interface on adsorbed H

6.1 Introduction

At present a comprehensive atomic–level picture of the electrochemical interface is lacking. So, electrochemical interface was the main concern of my research, as most of the calculations reported throughout the thesis are done at the level where interface is explicitly included in the simulations. In the previous chapter, I have explained a model to address pH and potential in atomic scale simulations for metal-solution interfaces. In this chapter, I have studied electrochemical hydrogen adsorption from first principles using that model, which accounts for potential and pH and explicitly treats the atomic structure of the electrode-electrolyte interface.

We know that by using computational reversible hydrogen electrode (CHE), the chemical potential of protons and electrons can be substituted with that of hydrogen molecules, which means that protons solvated in water never have to be explicitly calculated, as it is instead possible to refer to gas phase hydrogen[161]. Hydrogen adsorption has been intensively studied applying the CHE approximation, [162][163] whereas this approach is likely to provide insight into trends in adsorption and activity it is clear that the effect of the interface is totally neglected and the role of the electrochemical interface on the hydrogen adsorption is out of the scope of this type of simulations. I have used different names for CHE (reference hydrogen electrode (RHE), reversible hydrogen electrode, and computational hydrogen electrode) on various occasions, but they all refer to CHE. It is possible to qualitatively test the effect of the interface by adding a field and/or include water either explicitly or as a medium. The former type of calculations suggests that hydrogen on a Pt surface only very weakly feels the effect of the electrochemical interface, which explains why the CHE approach actually works[161]. However, recent modeling contradicts this and suggests that the hydrogen adsorption on Pt(111) is dependent on pH.[164]

The aim of this paper is to investigate the effect of the electrochemical interface, including pH, on hydrogen adsorption over Pt(111) and Pt(100). I have previously presented a method for including pH and electrode potential in atomic-scale simulations[165]. The analysis performed in this paper is based on that method. I find that hydrogen adsorption is totally dominated by the electrode surface, and the interface barely influences the results. This shows that in the case of hydrogen the interaction between the surface and the electrolyte is negligible and the effect of pH is not visible in the results. I have also calculated the pseudo capacitances for Pt(100) and Pt(111) surfaces for hydrogen adsorption region, which agrees to the experiments. Most of the written contents for this chapter are actually taken from the draft attached in the end of thesis.

6.2 Metal-water interface calculations

I have performed simulations on Pt(100) and Pt(111) covered with 0-2 monolayers of hydrogen in the presence of an explicitly treated bi-layer of water. The energy per surface Pt, accumulated at the interface as hydrogen is adsorbed, can be calculated according to equation (6.1), where G(n,N) is the energy of the interface with N surface Pt atoms and n hydrogen adsorbed and $G(H_2(g))$ is the energy of a hydrogen gas molecule at standard pressure and temperature. ΔG^{int} calculated this way is therefore the Gibbs-isotherm at zero vs. the computational hydrogen electrode (CHE).

$$\Delta G^{\text{int}} = \frac{G(n,N) - G(0,N) - \frac{1}{2}nG(H_2(g))}{N}, \tag{6.1}$$

Fig. 6.1 shows the integral adsorption energy of hydrogen, $\Delta G^{int}(\phi, \theta)$, as a function of the work function, ϕ, of the interface for different hydrogen coverages, $\theta = n/N$. The different work functions originate from different orientations of the individual water molecules and hence their dipoles[166]. The energy of the hydrogen changes within a few hundreds of an eV as the orientations of the water dipoles change. This small variation is in agreement with previous simulations with a field added

across the interface[164],[167] and consistent with the small dipole moment of H* perpendicular to the surface.

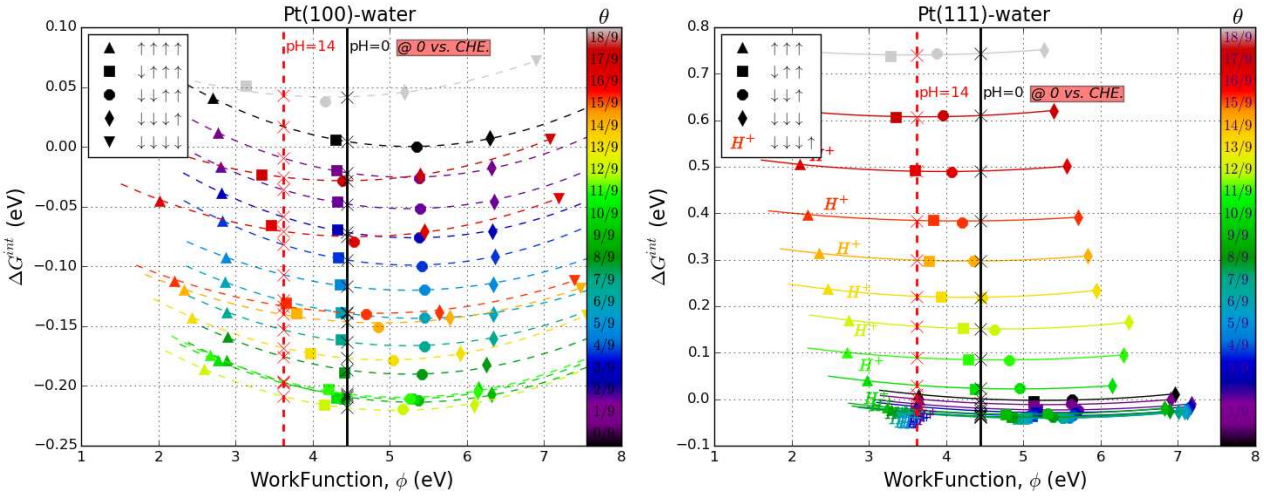

Fig. 6.1: ΔG^{int} for a) Pt(100) and b) Pt(111), plotted against the work function, ϕ , for different coverage of adsorbed hydrogen θ (indicated by the color). The legend shows the dipole orientation of the water structure, with H_up water indicated by ↑ and H_down by ↓. The black vertical line is the work function at zero potential vs. CHE for pH= 0 (ϕ = 4.44 V) and the red vertical line is the work function at zero potential vs. CHE for pH =14 (ϕ = 3.61 V).

6.2.1 Proton adsorption at the interface:

Protons solvated in the water layer (WL) at the electrochemical interface might also interact strongly, at the same time with the metal surface, which will result in enthalpy gain and a barrier for it to reach the surface. However, for Pt surface, the calculations suggest [168],[169],[170],[171],[172],[173],[174] that as soon as the structure is relaxed, proton is transferred to the Pt surface except for the cases where the proton reacts with adsorbed hydrogen in order to make molecular hydrogen. Here I will also report a case, where the proton is more stable at the interface, being co-adsorbed between Pt(111) surface and WL, where it interacts strongly with the Pt(111) surface by pulling up a Pt atom from the surface (similar to the case where it is adsorbed on an on-top). The corresponding atomic structure relaxed by

using RPBE, is shown in Fig. 6.2a in comparison to another system where this proton is replaced by H* (adsorbed on the surface), cf. Fig. 6.2b. For the former case, the metal-water separation is considerably reduced due the proton being stable in the outer Helmholtz plane (OHP).

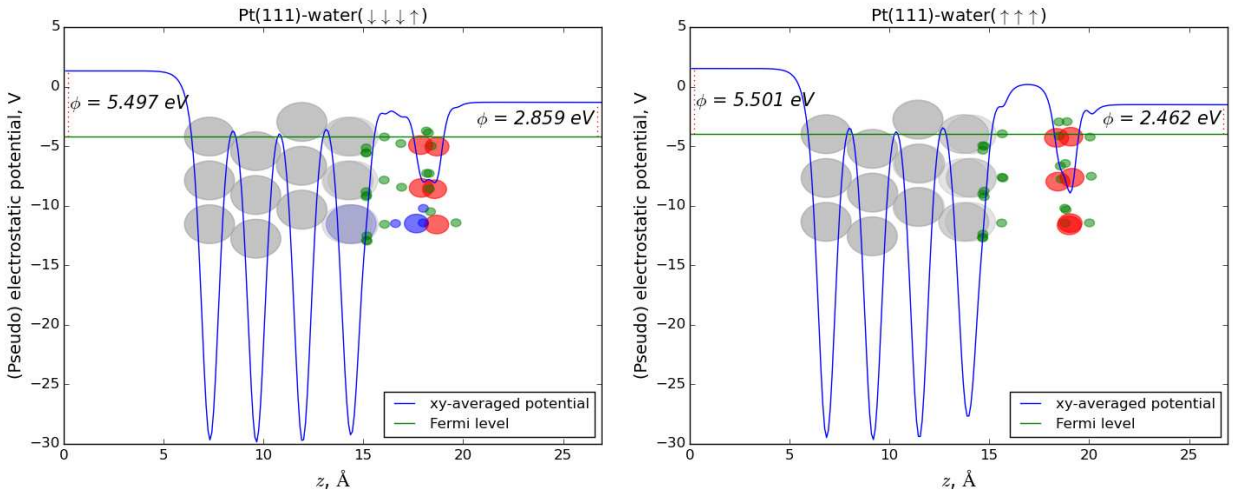

(a). *(b).*

Fig. 6.2: Pt(111)-water interfacial atomic structures for a) Pt(111)_12H_{ad} - WL,H^+ and b) Pt(111)_13H_{ad} - WL. Both the sysems have equal number of atoms, but former system have proton which is co-adsorbed between water and metal electrode shown by the corresponding oxygen atom in blue shade.

This proton is more stable at the interface between WL and Pt(111) surface for the coverages (θ) less than 13/9 ML of hydrogen as suggested by H^+ symbols in Fig. 6.1b, but only for a specific dipole of water layer (WL) as mentioned on top of Fig. 6.2a. This WL has thrice number of (out of plane) water molecules pointing down than pointing up, but still results in a workfunction which is more or less the same which one get with complete H_up WL as shown in Fig. 6.2b. So, the proton in the OHP, causes big change in the electrostatic environment in electric double layer (EDL). However, for coverages above 13/9 ML, this proton still hangs in the WL, where it is less stable than the being adsorbed on the surface.

6.2.2 Metal-water separation for PBE and RPBE functionals:

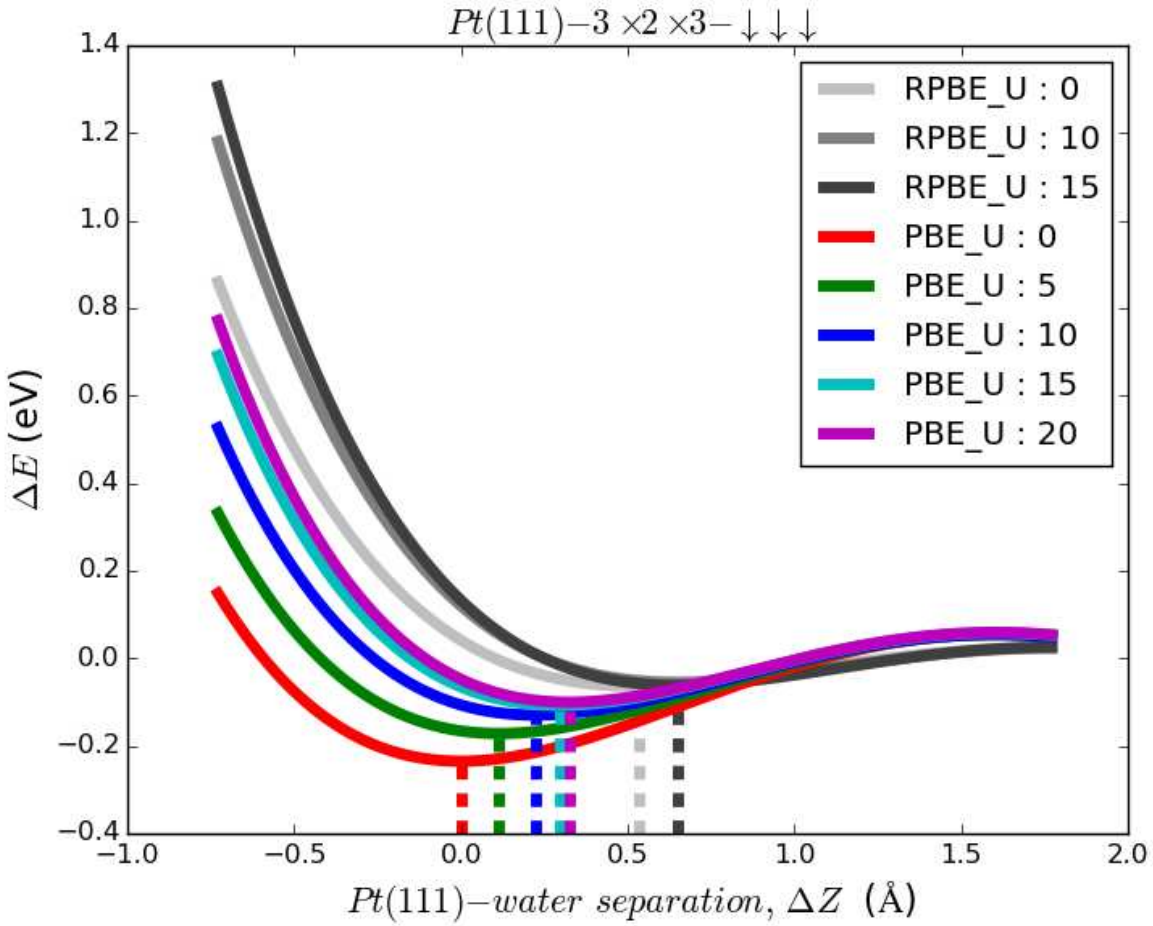

Fig. 6.3: Comparision of metal-water interaction and separation for: PBE and RPBE. Vertical dash lines show minima for each curve. The value at x-axis show the extra added/removed separation compared to fully relaxed structure at U=0 using PBE.

RPBE usually suggest larger metal-water separation, and less chemical interaction between these two, compared to PBE functional as suggested by the Fig. 6.3. Significant charge transfer at the interface is frequently observed, when PBE functional is used to model metal-water interface. It is due to the position of the HOMO level for the water (electrolyte), which is being too high in energy, when PBE functional is used.[175] However, if we add a U term, the PBE calculations suggest that metal-water interaction will decrease and separation between these two will increase. At higher values of U, PBE will more or less produce the RPBE results as shown by Fig. 6.3. The metal-water interfaces modeled here use RPBE functional, and lies in the middle regime, where metal Fermi level is straddle by HOME-LUMO gap of the electrolyte, hence avoid the pitfalls mentioned in the [163].

6.2.3 pH and field dependence of hydrogen adsorption

I want to compare the hydrogen adsorption on Pt(111) and Pt(100) at pH=14 and pH=0, at constant potential vs. the computational hydrogen electrode (CHE), which means at constant chemical potential

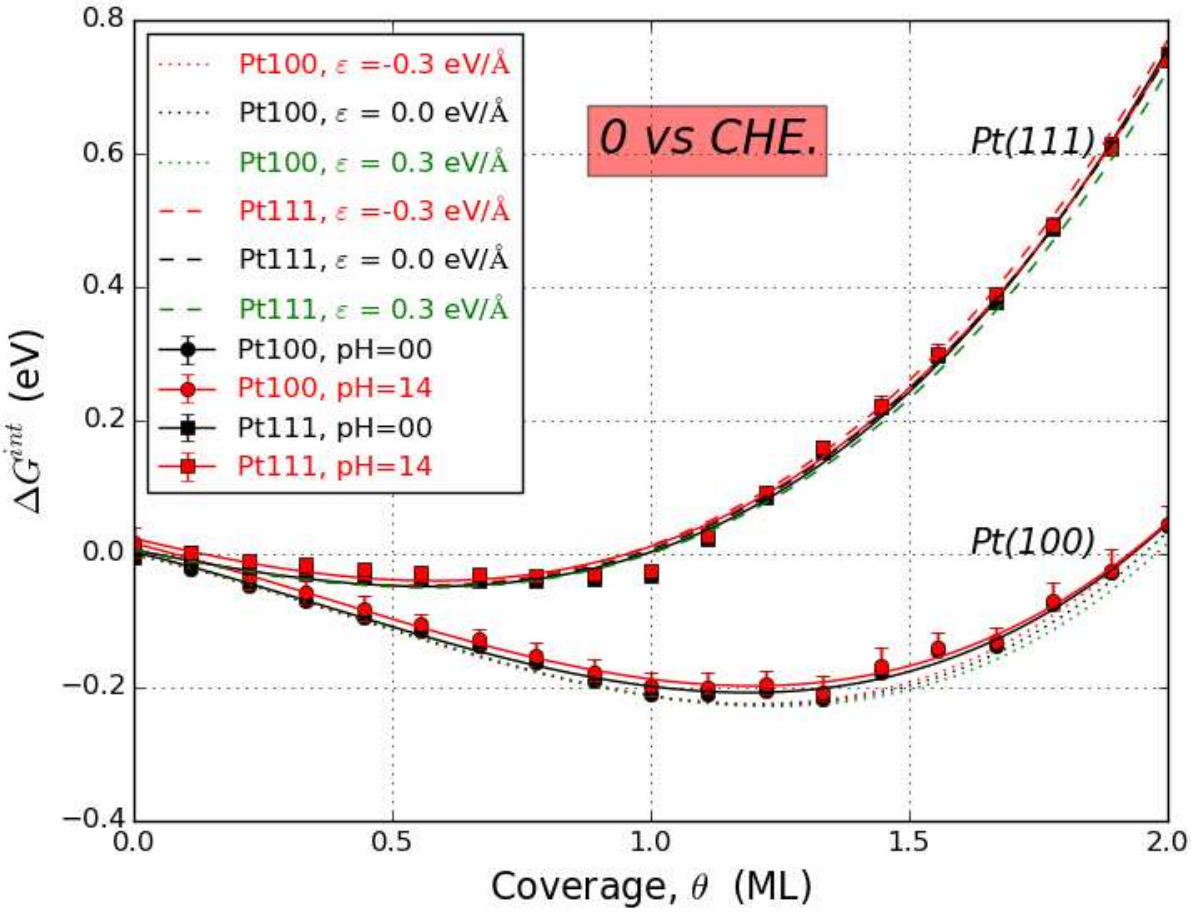

Fig. 6.4: ΔG^{int} plotted as a function of the hydrogen coverage. The black and red points correspond to the crossings of the black and red vertical lines with the different coverage lines in Fig. 6.1 (indicated by the x'es in Fig. 6.1). The dashed and dotted curves represent the results without water, with or without an electric field.

for $H^+ + e^-$. Therefore the value of ΔG^{int} at the work function corresponding to 0 vs. CHE is needed for all the coverages shown in Fig. 6.1. The energies are found by reading off the crossing with the two vertical lines in Fig. 6.1a and 6.1b. The solid black line at ϕ = 4.44 V corresponds to the work function of the standard hydrogen electrode defined at pH=0 and zero potential vs. CHE. The dashed red line at ϕ = 3.61 (=4.44 V -14*0.059 V/pH) indicates the work function at zero potential vs. CHE at pH=14.

Fig. 6.4 reports the interpolated values of ΔG^{int} from Fig. 6.1, plotted as a function of the hydrogen coverage. Two distinctly different curves are shown for Pt(100) and Pt(111). These represent the energies of the interfaces when $H^+ + e^-$ is in equilibrium with hydrogen. The difference between the two curves reflects the difference in binding energy and the difference in interaction between the hydrogen atoms adsorbed on the surface. The repulsion is larger on Pt(111) than on Pt(100) because of the close-packed structure of the (111) surface. In addition, Fig. 6.4 reports results obtained in the absence of water, with and without a field. Comparing the different curves, it is obvious that for the surfaces investigated here neither pH nor water or electric field has any discernable influence on the adsorption. This strongly suggests that the interaction between hydrogen on the Pt surface and the electrolyte is very weak. This in turn means that hydrogen on Pt does not depend on the pH. This is a consequence of the very small dipole of hydrogen on Pt and the lack of any specific interaction between the electrolyte and the surface. In this study I have not pre-assumed any particular behavior of the energy with respect to the field, it is measured in the calculations. A change in work function does not necessarily give rise to a change in energy, thus there is no or very little influence of the pH and the nature of the electrolyte.

This study does not include any other possible ions than protons. However, those could only change the above results if they directly interact with the surface. Simply a change in the field will not influence the results reported here.

It is worth noticing that for stepped Pt a pH dependence in the hydrogen potential region has been observed experimentally[176]. This could be caused by hydrogen that on stepped surfaces gains a specific interaction with water or an interaction with the field. However, we do not consider that very plausible, as above one monolayer, where hydrogen adsorbs atop Pt atoms, they are still not interacting with the electrolyte. It is more likely that other species such as O*, HO* or water are strongly and specifically adsorbed on the defect sites. If these adsorbates interact strongly with the electrolyte, which is likely as they can form hydrogen bonds, the binding energy of these species becomes dependent on pH. The potential for hydrogen adsorption on defect sites therefore, indirectly, also becomes dependent on pH as the hydrogen has to replace e.g. adsorbed water, which is pH dependent. In principle this effect could also play a role for Pt(100) and Pt(111) if the water molecules are specifically adsorbed,

however, this is not seen in the simulations, except for the case where proton is more stable in the water layer for Pt(111). It should be noted that the description of water with standard GGA functionals could be debated; especially the too high position of the HOMO level can give rise to charge transfer from the water to the Pt surface [163]. However, this artifact is not present in the simulations presented here as discussed above. Moreover, the lack of vdW interactions could change the adsorption energy, but it has to be very large to give rise to a strong adsorption of water on the low index facets of Pt

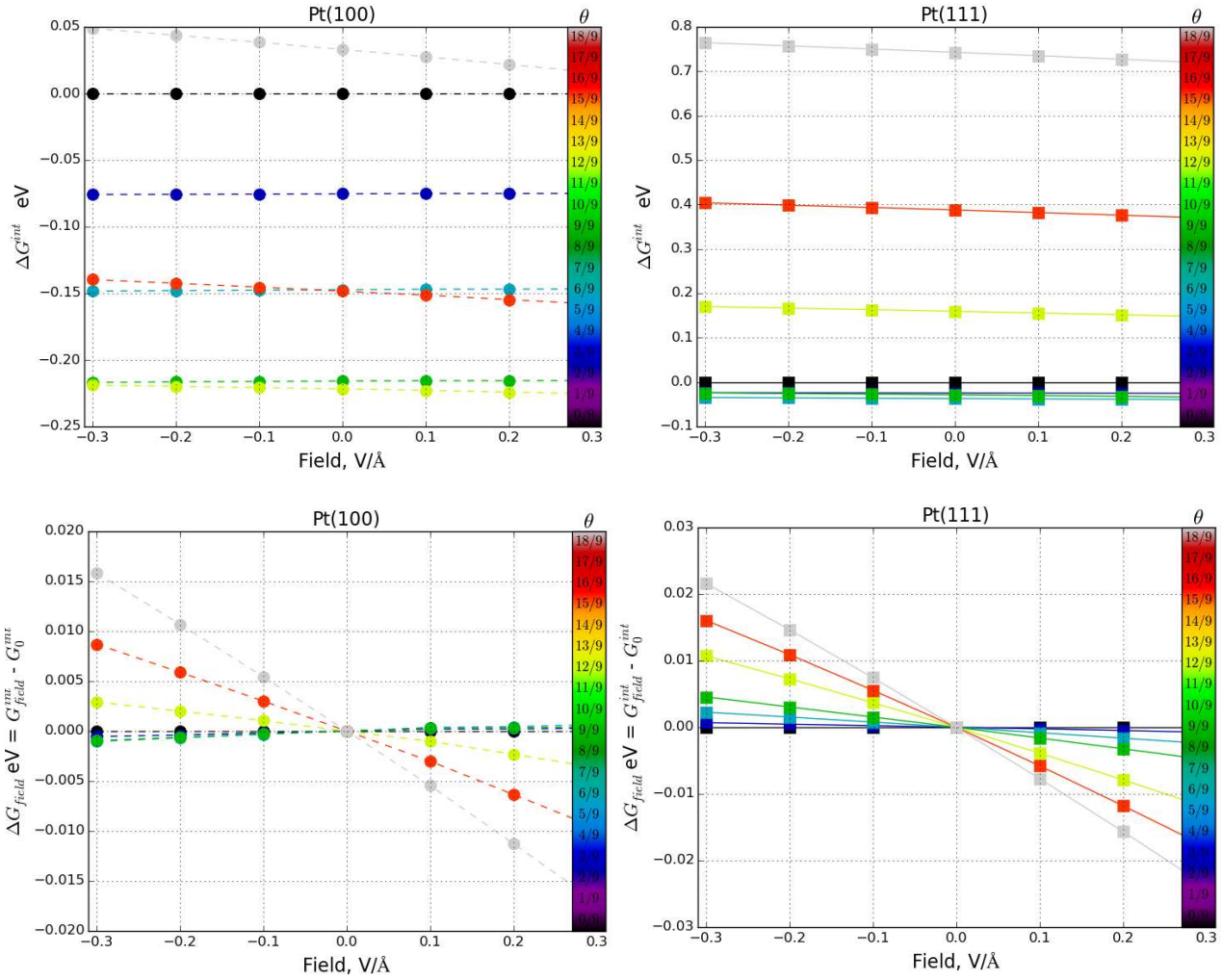

Fig. 6.5: Change in G^{int} with respect to external applied field.

Fig. 6.5 reports the results where I have explicitly applied the external field instead of using water layers to set up a field at the interface. These results are also reported in Fig. 6.4.

6.3 Capacitances and phase diagrams

In the previous section I have studied hydrogen adsorption at zero potential vs. CHE as I used standard gas phase hydrogen as reference. By a slight modification of Eq. (1) it is possible to extend the analysis to any computational reversible hydrogen potential. ΔG^{int} then becomes a function of the chemical potential of the hydrogen atoms as shown in equation (6.2).

$$\Delta G^{\text{int}} = \frac{G(n,N) - G(0,N) - \frac{1}{2}nG(H_2(g))}{N} + \frac{n}{N}eU_{CHE} \tag{6.2}$$

Where $eU_{CHE} = -\mu_{H^+ + e^-}$ is the potential vs. CHE. Equation (6.2) then can be presented in a 3D plot with ΔG^{int}, ϕ and U_{CHE} as the three axes, cf. Fig. 6.6. Instead of having a line of pH = 0 for $U_{\text{CHE}} = 0$ we now get a plane for pH = 0 and ΔG^{int} as function of U_{CHE}.

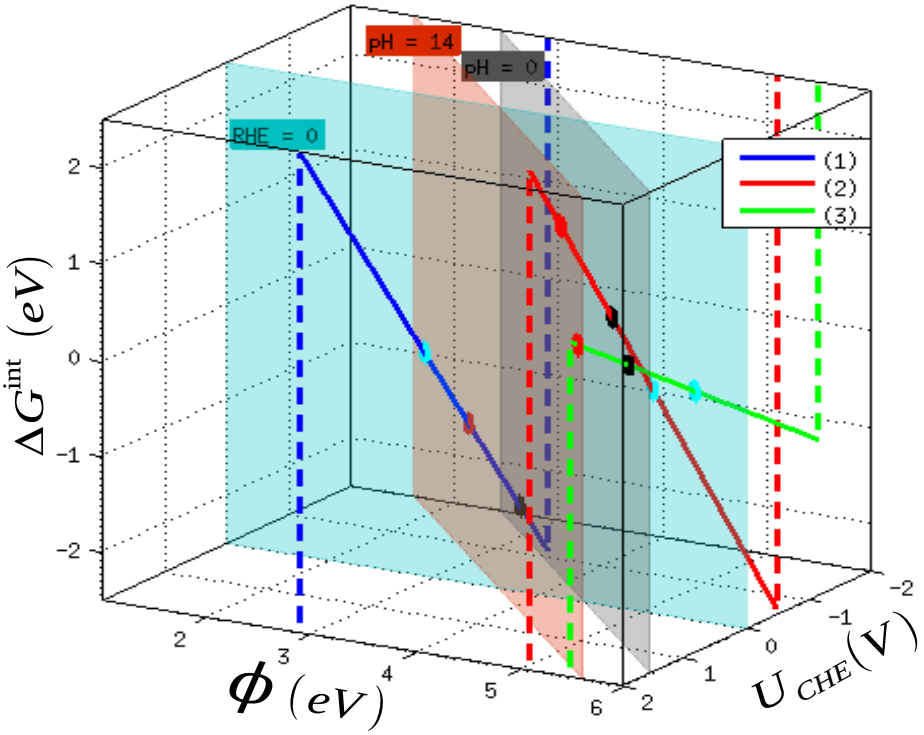

Fig. 6.6: ΔG^{int} as function of ϕ and U_{CHE} for exemplary metal-solution interfacial structures for Pt(100): (1) ϕ =2.9, θ=1.33, (2) ϕ=5.1, θ=1.44, (3) ϕ=5.5, θ=0.55. Colored marked circles on the lines show the projection of ΔG^{int} on the pH=0, pH=14 and CHE=0 planes. Dashed lines are shown as guides for the eye.

The CHE=0 plane intersects pH=0 and pH=14 planes at ϕ=4.44 eV and ϕ=3.61 eV, respectively. So, values of ΔG^{int} can be extrapolated for ϕ=4.44 eV and ϕ=3.61 eV using all the possible orientations of water mentioned in Fig. 6.1 in order to calculate ΔG^{int} values at pH=0 and pH=14 for U_{CHE} = 0 shown in Fig. 6.4.

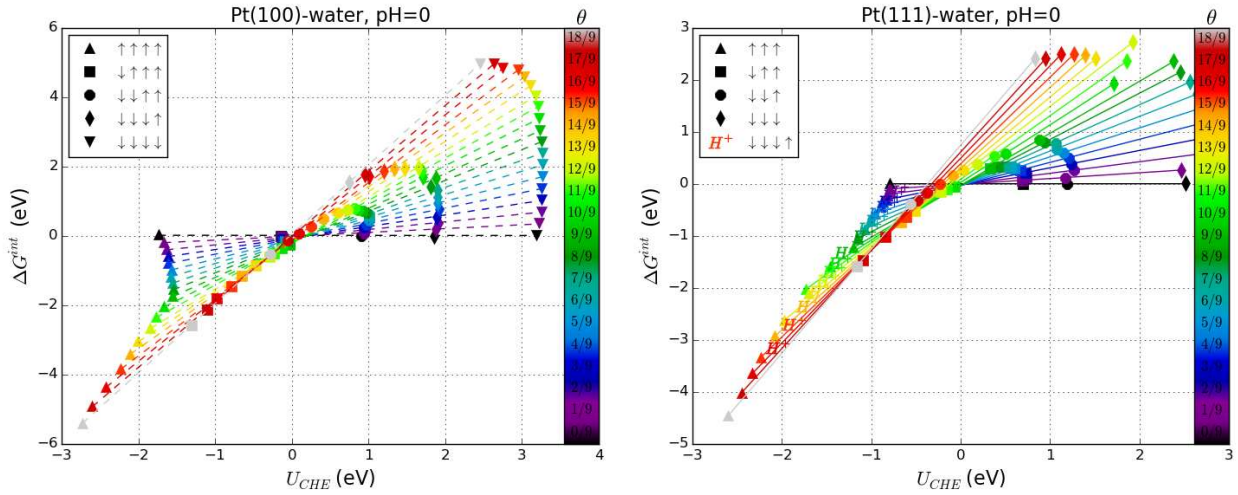

(a). *(b).*

Fig. 6.7: Phase diagrams for a) Pt(100) and b) Pt(111).

The ΔG^{int} projections on pH=0 plane against corresponding U_{CHE} values for Pt(100) and Pt(111) are plotted in Error: Reference source not found. These are the phase diagrams for hydrogen on Pt(100) and Pt(111). The first thing we note is that the coverage of hydrogen is increased as U_{CHE} is decreased. For Pt (111) hydrogen adsorbs in the FCC-hollow site until the coverage of 1 ML is reached, and upon further reduction of the potential the top sites start to be occupied. Ontop hydrogen is reactive and can form molecular hydrogen either with hydrogen atoms from neighboring hollow sites or with other ontop hydrogen. This means that in experiments it is impossible to accumulate two full monolayers of hydrogen on the surface. However, the simulations allow us to estimate the capacitance, when hydrogen atoms or protons and electrons are added to the interface.

In Fig. 6.8 the results from Error: Reference source not found have been summarized and fitted to parabolas as shown above each plot. As before, there is no clear difference between the results at pH=0 and pH=14. The configuration and coverage with the lowest G^{int} for a given U_{CHE} defines the most

stable structure of the interface. I will refer to this lower bound of G^{int} as G^{int}(min). In the simulations the coverage can only be varied in steps defined by the number of surface atoms in the slab. However, by means of interpolation, I did in Fig. 6.4, it is possible to obtain a continuous curve for $G^{int}(\theta)$ that can be directly translated into a continuous G^{int}(min), cf. Fig. 6.8.

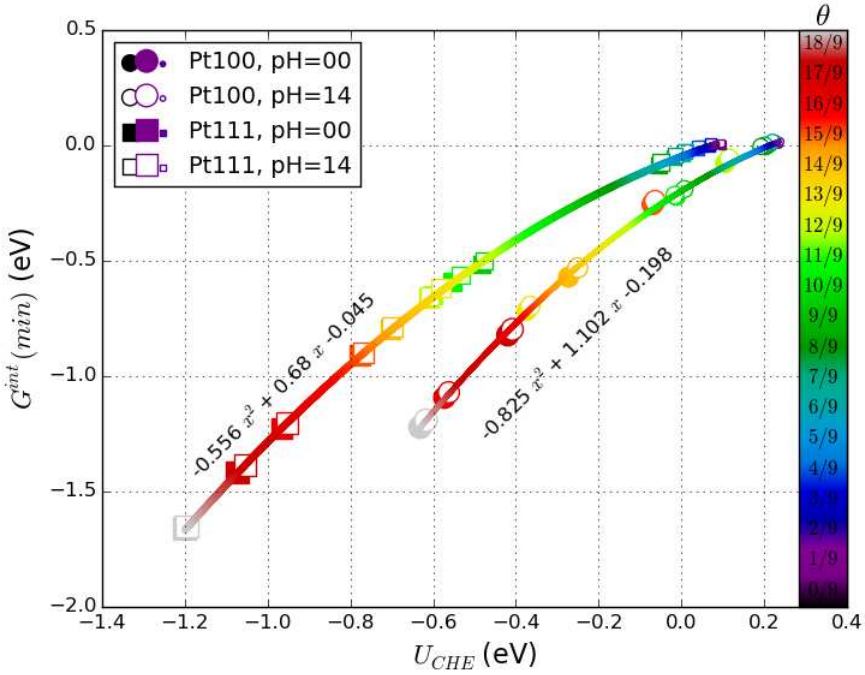

Fig. 6.8: The phase diagrams from Error: Reference source not founda and Error: Reference source not foundb showing $G^{int}(min)$ as function of U_{CHE}.

The curve in Fig. 6.8 represents the minimum of G^{int} as a function of CHE potential. G^{int}(min) is made up by lines of the different coverages with the slopes θ. These lines can be viewed as tangents $T(\theta,U)$ to G^{int}(min). If the function of $G^{int}(\theta)$ as function of coverage is known then G^{int}(min) can also be calculated as discussed in derivations. One can write the equation for tangent having slope θ *as*

$$T(\theta,\ U) = \theta(U - U_0) + G^{int}(\theta,\ U_0) \tag{6.3}$$

At G^{int}(min),

$$T(\theta,\ U) \approx T(\theta+\delta\theta,\ U) \tag{6.4}$$

$$\theta(U - U_0) + G^{int}(\theta, U_0) = (\theta+\delta\theta)(U - U_0) + G^{int}(\theta+\delta\theta, U_0) \quad (6.5)$$

$$\theta(U - U_0) - (\theta+\delta\theta)(U - U_0) = G^{int}(\theta+\delta\theta, U_0) - G^{int}(\theta, U_0) \quad (6.6)$$

$$-\delta\theta(U - U_0) = \delta G^{int}(\theta, U_0) \quad (6.7)$$

$$(U - U_0) = -\frac{\delta G^{int}(\theta, U_0)}{\delta\theta} \quad (6.8)$$

As G^{int}(min) is the intercept of tangents with the slopes $\theta + d\theta$. In other words, at the intercept,

$$T(\theta, U) = G^{int}(min)(U) \quad (6.9)$$

So, calculating G^{int} at the intercepts,

$$G^{int}(min)(U) = -\theta\frac{\delta G^{int}(\theta, U_0)}{\delta\theta} + G^{int}(\theta, U_0) \quad (6.10)$$

Considering the above equation (6.10), I have assumed U_0 (CHE potential) to be 4.44 and 3.614 for pH=0 and pH=14 respectively. I have calculated U vs. CHE for each coverage, where this coverage-line (tangents as mentioned by equation (6.9)) will give us G^{int}(min). So, we have set of points (each for every coverage), having values (U vs. CHE, G^{int}(min)). So, plotted circles and squares are for Pt100 and Pt111 surfaces respectively, where the filled symbols are for pH=0 and empty symbols are for pH=14 shown in Fig. 6.8.

I have interpolated all these points with parabolic fit, in such a way that the color of the line, which is showing the coverage, is also interpolated. It shows where each coverage starts to dominate as we change potential. So, this way I have get the G^{int}(min) for continuous coverage, instead of discrete coverage values. Parabolic equation from each parabola fit is also plotted over each parabola.

The curvature of G^{int}(min) shown in Fig. 6.8, is related to the capacitance. The capacitance is

dominated by adsorption of hydrogen on the surface. The work function only plays a negligible part. We know that parabolic equation for G^{int}(min) can be written as equation (6.11). So from the curvature of these parabolas one can calculate capacitance for each surface (Pt100, Pt111). The DFT calculated pseudo capacitance from curvature for Pt(111) is ~257 uF/cm^2, which is to be compared with experiments. In order to get experimental reference, I used experimental cyclic voltammogram as shown in Fig. 6.9. Considering the cyclic voltammogram, the current density for only the hydrogen adsorption or desorption region (half of the total width) can be divided with sweep rate, in order to get pseudo capacitance. By accounting for background double layer capacitance, one can get pseudo capacitance for H adsorption, which is around ~500 uF/cm^2 for Pt(111)[177],[178],[179],[180] I have

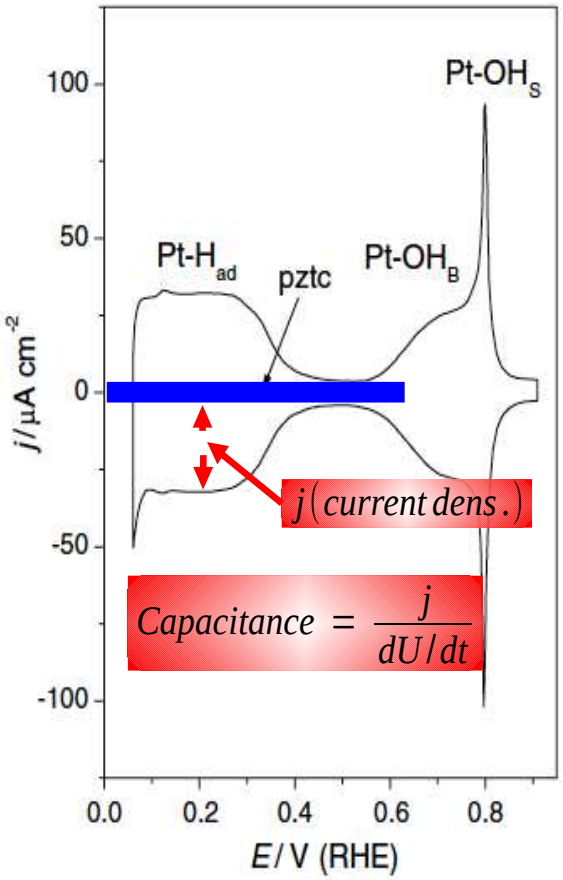

Fig. 6.9: State of the art Pt(111) cyclic voltammogram in 0.1 $HClO_4$ M solution at 50 mV^{-1}. Adapted from [25].

deduced this value from voltammogram, where the current density is almost flat with respect to potential and capacitance is given by j/(dU/dt).3 This is the potential region where most of the

3
dU/dt is the sweep rate

hydrogen is adsorbed on the FCC-hollow site (just before hydrogen evolution region). DFT overestimates the distance among metal atoms, and I have used optimized lattice constant which is 4.02 Å, which is different than experimentally known value of ~3.92 Å. The capacitances are reported in uF/cm^2, which is part of reason that DFT suggest slightly less capacitance. For Pt(111), it is unlikely that other ions are co-adsorbed in this potential range. However, for Pt(100), other ions might also be co-adsorbed in the hydrogen adsorption region, but a deduced value of ~425 uF/cm^2 can be compared with DFT calculated pseudo capacitance ~331 uF/cm^2 [162],[181].

$$G^{int}(min)(U) = -\frac{1}{2}CU^2 + bU + c \tag{6.11}$$

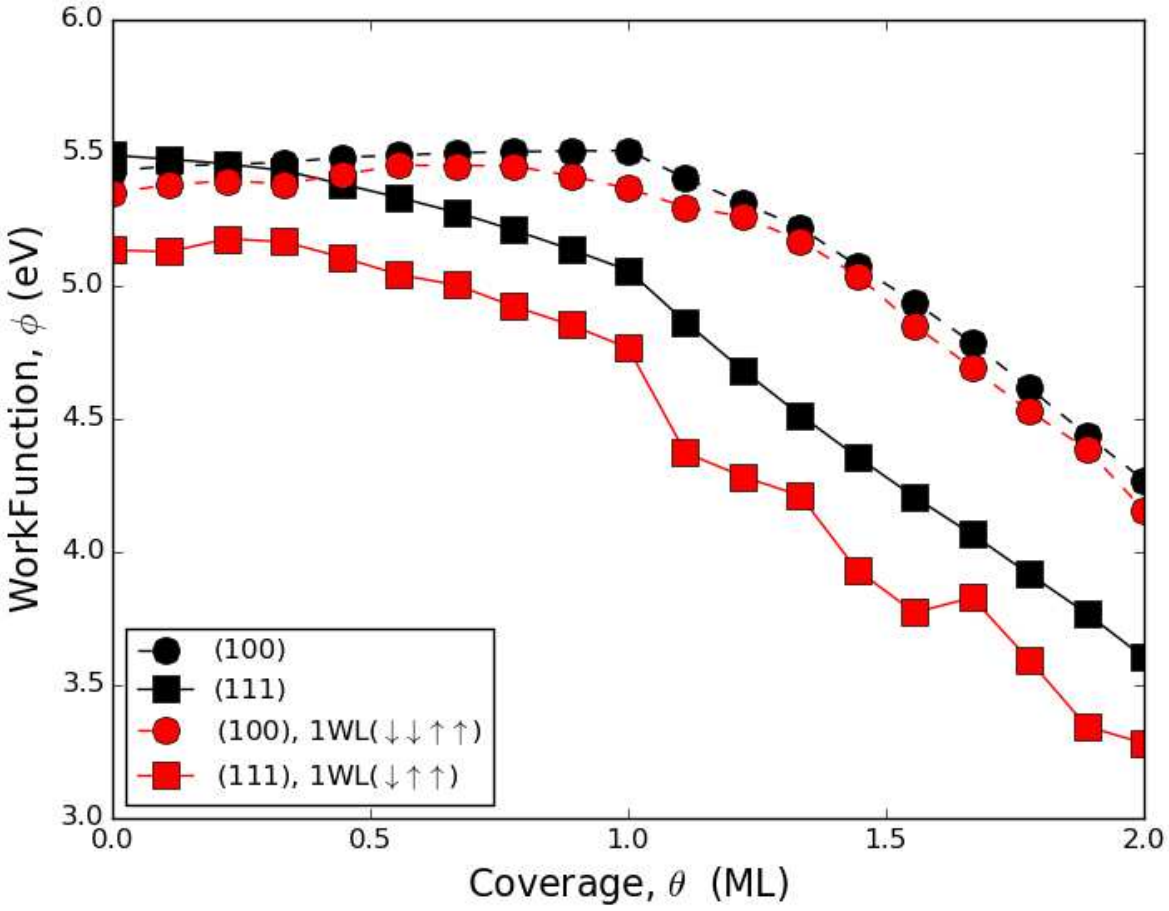

Fig. 6.10: : Change in workfunction, ϕ, as a function of coverage, θ.

The Fig. 6.10 shows, how the workfunction change as we increase the coverage for both Pt(100) and Pt(111) surfaces. Results with and without water layer are reported, however, for Pt(111) surface, the modeled water layer has a finite dipole as shown in the legend.

6.4 Summary

I have shown that on low index Pt facets, electrochemical hydrogen adsorption is totally dominated by the electrode surface, the interface barely influences the results. This shows that in the case of hydrogen the interaction between the surface and the electrolyte is negligible and the effect of pH is not visible in the results.

Previous studies have found the same, except studies where an energy dependency on the work function is assumed a priori e.g. with a capacitor model. In this study I do not assume any energy dependencies on the work function, however, it is calculated to be very small.

The simulations only contain a single water layer, however, as this layer does not play a role additional water layer cannot do that either. The description of water is based on standard GGA. This is probably fine for the hydrogen covered surfaces, but the results for clean surfaces could change slightly if higher-level functionals were used. This could give rise to a small pH dependence if the adsorption energy of physisorbed water changes with the work function. However, the major limitation of the analysis presented in the current paper is probably related to the lack of counter ions. This could influence the structure.

Chapter 7 :Summary and Outlook

In this thesis, I have looked beyond the CHE model, and focused on the simulations which treats the electrode-electrolyte interfaces explicitly. Since the electrode-electrolyte interface modeling is far from realistic, I aimed to address various challenges regarding first principle electrochemical interface modeling in order to bridge the gap between the model interface used in simulations and real catalyst at operating conditions..

First principle methods have limitations due to the various approximations in implementations and may sometimes lead to incorrect electronic structure at the electrochemical interface, which can result in a improper/ill-defined electrochemical interface. Considering the electronic structure of the interface, I have mentioned some of the pitfalls in modeling electrochemical interfaces, and I have also shown how to avoid these pitfalls. The electrode-electrolyte interface models constructed without care for electronic structure, could exhibit an unphysical charge transfer due to the DFT's notorious under-estimation of the HUMO-LUMO gap. For such systems, electrode potential cannot be tuned. I have shown that the HOMO-LUMO gap of the electrolyte have to straddle the metal Fermi level, in order for the whole system to qualify as a proper electrochemical interface. However, most of the Pt-water system, will qualify as proper electrochemical interface models.

I have also contributed to the model, which addresses pH in the first principle simulations of the electrochemical interfaces. This is an important step forward, since electrochemical reaction rate and barrier for charge transfer can strongly dependent on pH. I have shown that pH can have influence over the interface structure, and hence can influence the adsorbate free energies with direct hydrogen bonding or chemical interactions with the electrolyte dipole. Therefore, in order to study the reactions at constant electrochemical potential, pH has to be kept constant together with the chemical potential of protons and electrons. We note that some of the calcuations reported in the literature for constant electrocehmical potential, are not really done at constant electrochemical potential, as the chemical potential of proton (or pH) was not considered. However, in most of the cases, the effect of pH was negligible. We have applied this developed model to Pt(111)-water interface as an example, and

constructed the corresponding Pourbaix diagram, which shows the effect of pH and potential on adsorbate coverage and interface structure.

I have also investigated the pH effect on the electrochemical adsorption of hydrogen for Pt(100) and Pt(111) surfaces by applying the above model that account for pH in the simulations. As a consequence of negligible interaction between electrolyte and adsorbed hydrogen, I found that modeled electrochemical interface and pH have no influence over hydrogen adsorption energy. In fact, hydrogen adsorption is well defined by considering just CHE model. However, barrier for charge transfer, can depend on the pH, as pH can influence the water structure at the interface. I have also discussed a scenario, where proton is more stable at the electrochemical interface, where the water layer is almost chemi-adsorbed at the surface. This is an interesting case as proton being stable in the OHP, significantly change the electrostatic potential in the double layer region. This might also have an impact over barrier for charge transfer considering hydrogen evolution reaction (HER). I have also calculated the pseudo-capacitances for hydrogen adsorption region for both surfaces, which agrees with experiments.

Simulations differ with experiments in the sense that final optimized atomic structure is used to calculate potential and pH, where in experiments, one sets potential and pH, which then in return setup the corresponding atomic structure. In the first principle calculations, we feed an atomic structure, which has fixed number of atoms and a fix total charge. Then the potential, surface charge, pH, optimized atomic structure and other informations can be obtained as posteriori. This is in contrast to experiments, where potential and pH setup the corresponding interfacial atomic structure as shown in Fig. 7.1.

The chemical potential and pH may change during structural optimizations or dynamic simulations. In a dream scenario, chemical potential and pH must stay the same during structural optimization in contrast to perform normal constant charge calculations and then from the interfacial structure measure the potential and pH. However, this is still a challenge present for the electrochemical interface simulations that needed to be solved.

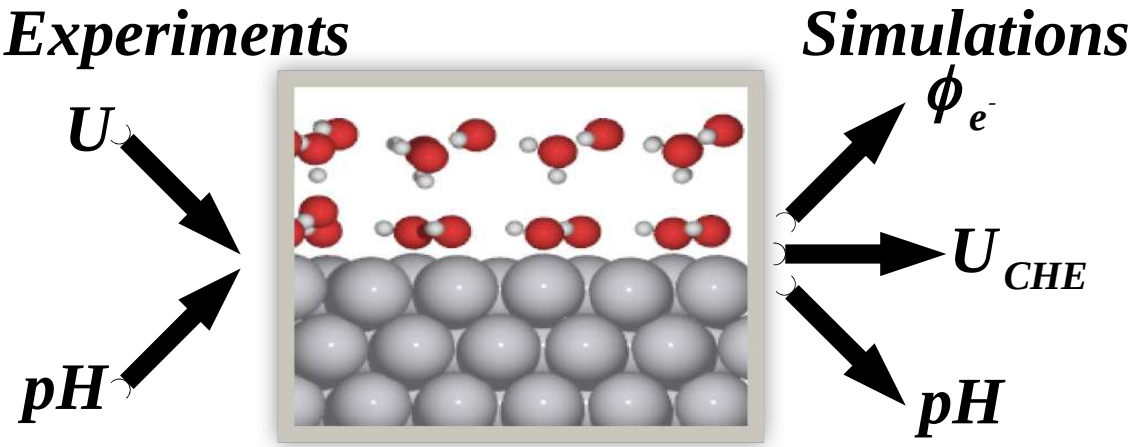

Fig. 7.1: Simulations in contrast to experiments

[1] All fossil fuel reserve and consumption data from CIA World Factbook.

[2] http://www.iea.org/publications/insights/global_value_of_coal.pdf

[3] U.S. department of energy, sustainability and maintaining US competitiveness (June 2010), p. 4

[4] http://www.euchems.eu/fileadmin/user_upload/highlights/Euchems_Roadmap_gesamt_final2.pdf

[5] www.theglobaleducationproject.org/earth/energy-supply.php

[6] Earth Policy Institute (www.earthpolicy.org)

[7] http://en.wikipedia.org/wiki/Mauna_Loa_Observatory

[8] http://en.wikipedia.org/wiki/Ocean_heat_content#cite_note-1

[9] www.skepticalscience.com/graphics.php?g=12

[10] IPCC AR5 WG1 (2013). PDF "Summary for policymakers"

[11] http://en.wikipedia.org/wiki/Effects_of_global_warming_on_oceans

[12] www.skepticalscience.com

[13] Perez et al., 2009, "A Fundamental Look At Energy Reserves For The Planet", p.3, PDF (wikipedia)

[14] J. Rossmeisl, Á. Logadóttir, J. K. Nørskov, *Chem. Phys.* 319 (2005) 178.

[15] http://en.wikipedia.org/wiki/Catalysis#cite_note-IUPACc-1

[16] Nicéphore Bonnet and Nicola Marzari, *PRL 110*, 086104 (2013)

[17] http://en.wikipedia.org/wiki/Catalysis#cite_note-2

[18] L.E. Ballentine. *Quantum Mechanics a Modern Development*. World Scientific, corrected printing edition, 1998.

[19] P. Hohenburg, W. Kohn, Phys. Rev. **136**, B864 (1964).

[20] W. Kohn and L. J. Sham, Phys. Rev. **140**, A1133 (1965).

[21] W. Kohn, Reviews of Modern Physics **71**, 1253 (1999).

[22] P. Hohenburg and W. Kohn. Inhomogenous electron gas. Phys. Rev. **136**, B864-B871, (1964).

[23] W. Kohn. Nobel lecture: Electronic structure of mater-wave functions and density functionals. Rev. Mod. Phys., 71(5):1253, (1999).

[24] E. H. Lieb. Density functionals for coulomb-systems. *Int. J. Quant. Chem*., 24(3):243-277, (1983).

[25] M. Levy. Electron-densities in search of hamiltonians. *Phys. Rev. A*, 26(3):1200-1208, (1982).

[26] W. Kohn and L.J. Sham. Self-consistent equations including exchange and correlation effects.

Phys. Rev., 140:A1133-A1138, (1965).

[27] D. M. Ceperly and B. J. Alder. Ground state of the electron gas by a stochastic method. J. Chem. Phys., 45:566–569, 1980.

[28] L. Wilk, S.J. Vosko, and M. Nusair. Accurate spin-dependent electron liquid correlation energies for local spin density calculations: a critical analysis. Can. J. Phys , 58:1200, 1980.

[29] J.P. Perdew and A. Zunger. Self-interaction correction to density-functional approximations for many-electron systems. Phys. Rev. B , 23:5048, 1981.

[30] Y. Wang and J.P. Perdew. Correlation hole of the spin-polarized electron-gas, with exact small-wave-vector and high-density scaling. Phys. Rev. B, 44(24):13298–13307, 1991.

[31] M. Ernzerhof and G.E. Scuseria. Assesment of perdew burke ernzerhof exchange-correlation functional. J. Chem. Phys. , 110(11):5029, 1999.

[32] J.P. Perdew, K. Burke, and M. Ernzerhof. Generalized gradient approximation made simple. Phys. Rev. Lett., 77(18):3865, 1996.

[33] B. Hammer, L.B. Hansen, and J.K. Nørskov. Improved adsorption energetics within density functional theory using revised perdew-burke-ernzerhof function-als. Phys. Rev. 59(11):7413–7421, 1999.

[34] T. Van Voorhis and G.E. Scuseria. A never form for the exchange-correlation energy functional. J. Chem. Phys., 109(2):400–410, 1998.

[35] V.N. Staroverov, G.E. Scuseria, J.M. Tao, and Perdew JP. Comparative assessment of a new nonempirical density functional: Molecules and hydrogen-bonded complexes. J. Chem. Phys., 119(23):12129–12137, 2003.

[36] P. E. Blöchl, *Phys. Rev. B* **50** (1994) 17953−17979.

[37] B. Hammer, L. B. Hansen and J. K. Nørskov, *Phys. Rev. B* **59** (1999) 7413−7421.

[38] J. J. Mortensen, L. B. Hansen and K. W. Jacobsen, *Phys. Rev. B* **71** (2005) 035109.

[39] J. Enkovaara, C. Rostgaard, J. J. Mortensen, J. Chen, M. Dułak, L. Ferrighi, J. Gavnholt, C. Glinsvad, V. Haikola, H. A. Hansen, H. H. Kristoffersen, et al., *J. Phys.: Condens. Matter* **22** (2010) 253202.

[40] Atomic Simulation Environment (ASE), [https://wiki.fysik.dtu.dk/ase], Center for Atomic-scale Materials Design (CAMD), Technical University of Denmark.

[41] L. Bengtsson, *Phys. Rev. B* **59** (1999) 12301−12304.

[42] J. Greeley, I. E. L. Stephens, A. S. Bondarenko, T. P. Johansson, H. A. Hansen, T. F. Jaramillo, J.

Rossmeisl, I. Chorkendorff and J. K. Nørskov, Nat. Chem., 2009, 1, 552–556.

[43] J. K. Nørskov, T. Bligaard, J. Rossmeisl and C. H. Christensen, Nat Chem, 2009, 1, 37–46.

[44] F. Calle-Vallejo and M. T. Koper, Electrochim. Acta, 2012, 84, 3–11.

[45] Behler et al, 2005

[46] Bucko et al.,2005

[47] Hensen et al.,2005

[48] Honkala et al.,2005

[49] Kieken et al., 2005

[50] Xu et al., 2005

[51] Zellner et al., 2005

[52] J. Rossmeisl, E. Skúlason, M. E. Björketun, V. Tripkovic and J. K. Nørskov, Chem. Phys. Lett., 2008, 466, 68–71.

[53] M. Otani and O. Sugino, Phys. Rev. B, 2006, 73, 115407.

[54] C. D. Taylor, S. A. Wasileski, J.-S. Filhol and M. Neurock, Phys. Rev. B, 2006, 73, 165402.

[55] J. K. Nørskov, J. Rossmeisl, A. Logadóttir, L. Lindqvist, J. R. Kitchin, T. Bligaard, and H. Jónsson, J. Phys. Chem. 108, 17886 (2004).

[56] Andrzej Wieckowski. *Fuel Cell Catalysis: A Surface Science Approach*. Wiley-Interscience. p64-p65 (2009).

[57] Hoogers, G.; Thompsett, D. CATTECH 1999, 3, 106

[58] J. Greeley, I. E. L. Stephens, A. S. Bondarenko, T. P. Johansson, H. A. Hansen, T. F. Jaramillo, J. Rossmeisl, I. Chorkendorff and J. K. Nørskov, Nat. Chem., 2009, 1, 552–556

[59] J. K. Nørskov, T. Bligaard, J. Rossmeisl and C. H. Christensen, Nat Chem, 2009, 1, 37–46.

[60] F. Calle-Vallejo and M. T. Koper, Electrochim. Acta, 2012, 84, 3–11.

[61] Luigi Galvani, wikipedia

[62] Alessandro Volta, wikipedia

[63] O. Stern, Z. Electrochem. 30, 508 (1924)

[64] Egill Skúlason, Ph.D. Thesis, Technical University of Denmark, Lyngby (July 2009).

[65] Atkins, P. W. Physical Chemistry , 10th ed., Oxford University Press: Oxford, U.K., 1998.

[66] H. von Helmholtz, Ann. Phys. 89 (1853) 211.

[67] Vladimir Tripković, Ph.D. Thesis, Technical University of Denmark, Lyngby (July 2010).

[68] G. Gouy, Compte. Rend. 149 (1910) 654.

[69] D. Chapman, Philos. Mag. 25 (1913) 475.

[70] D. Grahame, Chem. Rev. 41 (1947) 441.

[71] H. Ogasawara, B. Brena, D. Nordlund, M. Nyberg, A. Pelmenschikov, L. G. M. Petterson, A. Nilsson, Phys. Rev. Lett. 89 (2002) 276102.

[72] P. J. Feibelman, Science 295 (2002) 99.

[73] C. Clay, S. Haq, A. Hodgson, Phys. Rev. Lett. 92 (2004) 46102.

[74] G. Held, D. Menzel, Surf. Sci. 92 (1994) 316.

[75] A. Michaelides, P. Hu, J. Am. Chem. Soc. 123 (2001) 4235 .

[76] G. S. Karlberg, G. Wahnström, Phys. Rev. Lett. 92 (2004) 136103

[77] A. Michaelides, V. A. Ranea, P. L. de Andres, D. A. King, Phys. Rev. Lett. 90 (2003) 216102

[78] J. Carrasco, A. Michaelides, M. Scheffler, J. Chem. Phys. 130 (2009) 184707.

[79] S. Schnur, A. Groβ, New J. Phys. 11 (2009), 125003.

[80] A. Roudgar, A. Groβ, Chem. Phys. Lett. 409 (2005) 157.

[81] A. Michaelides, A. Alavi, D. A. King, Phys Rev. B 64 (2004) 113404.

[82] P. J. Feibelman, Science 295 (2002) 99.

[83] S. Haq, J. Harnett, and A. Hodgson, Surf. Sci. 505 (2002) 171.

[84] M. Morgenstern, T. Michely, G. Comsa, Phys. Rev. Lett. 77 (1996) 703.

[85] M. Morgenstern, J. Muller, T. Michely, G. Comsa, Z. Phys. Chem. 198 (1997) 43.

[86] S. Izvekov, A. Mazzolo, K. Van Opdorp, G. A. Voth, J. Chem. Phys. 114 (2001) 3284.

[87] S. Izvekov and G. A. Voth, J. Chem. Phys. 115 (2001) 7196.

[88] S. Meng, L. F. Xu, E. G. Wang, and S. W. Gao, Phys. Rev. Lett. 89 (2002) 176104.

[89] S. Meng, E. G. Wang, S. Gao, Phys. Rev. B 69 (2004) 195404.

[90] M. Otani, O. Sugino, Phys. Rev. B 73 , (2006) 115407.

[91] O. Sugino, I. Hamada, M. Otani, Y. Morikawa, T. Ikeshoji, Y. Okamoto, Surf. Sci. 601 (2007) 5237.

[92] M. Otani, I. Hamada, O. Sugino, Y. Morikawa, Y. Okamoto, T. Ikeshoji, Phys. Chem. Chem. Phys. 10 (2008) 3609.

[93] J.-S. Filhol, M. Neurock, Angew. Chem. Int. Ed . 45 (2006) 402.

[94] C. D. Taylor, S. A. Wasileski, J.-S. Filhol, M. Neurock, Phys. Rev B 73 (2006) 165402.

[95] M. J. Janik, C. D. Taylor, M. Neurock, J. Electrochem. Soc. 156 (2009) B126.

[96] S. Trasatti, Electrochim. Acta 36 (1991) 1659.

[97] Y. Cai, A. B. Anderson, J. Phys. Chem. B 108 (2004) 9829. 114

[98] E. Skúlason, G.S. Karlberg, J. Rossmeisl, T. Bligaard, J. Greeley, H. Jónsson and J.K. Nørskov, Phys. Chem. Chem. Phys. , 9 (2007) 3241.

[99] J. Rossmeisl, J. Nørskov, C. Taylor, M. Janik, and M. Neurock, J. Phys. Chem. B 110, 21833 (2006)

[100] T. Rod, Ph.D. Thesis, Technical University of Denmark, Lyngby (February 2000).

[101] K. N. Kudin and R. Car, J. Am. Chem. Soc. 130, 3915 (2008).

[102] J. Rossmeisl, E.Skúlason, M. E. Björketun, V. Tripković and J. K. Nørskov, Chemical Physics Letters, 466 68-71 (2008)

[103] G. Zundel, H. Metzger, Z. Physik. Chem. (N.F.) 58 (1968) 225.

[104] M. Eigen, Angew. Chem. Int. Ed. 3, 1 (1964).

[105] E. Skúlason, V. Tripković, M. E. Björketun, S. Guðmundsdóttir, G. Karlberg, J. Rossmeisl, T. Bligaard, H. Jónsson, J. K. Nørskov, J. Phys. Chem. 114 (2010), 18182-18197

[106] T. Pajkossy , D.M. Kolb, Electrochem. Acta 46 (2001) 3063.

[107] Y. Cai, A. B. Anderson, J. Phys. Chem. B 108 (2004) 9829.

[108] J.-S. Filhol, M. Neurock, Angew. Chem. Int. Ed. 45 (2006) 402.

[109] M. Otani, O. Sugino, Phys. Rev. B 73 (2006) 115407.

[110] P. Vassilev, R. A. van Santen, M. T. M. Koper, J. Chem. Phys. 122 (2005) 054701.

[111] J. Rossmeisl, E. Skúlason, M. E. Björketun, V. Tripković, J. K. Nørskov, Chem. Phys. Lett. 466 (2008) 68.

[112] R. Jinnouchi, A. B. Anderson, Phys. Chem. C 112 (2008) 8747.

[113] S. Schnur, A. Groß, New J. Phys. 11 (2009) 125003.

[114] M. J. Janik, C. D. Taylor, M. Neurock, J. Electrochem. Soc. 156 (2009) B126.

[115] E. Santos, A. Lundin, K. Pötting, P. Quaino, W. Schmickler, Phys. Rev. B 79 (2009) 235436.

[116] E. Skúlason, V. Tripković, M. E. Björketun, S. Gudmundsdóttir, G. S. Karlberg, J. Rossmeisl, T. Bligaard, H. Jónsson, J. K. Nørskov, J. Phys. Chem. C 114 (2010) 18182.

[117] J. Cheng, M. Sprik, Phys. Rev. B 82 (2010) 081406.

[118] S. Schnur, A. Groß, Catal. Today 165 (2011) 129.

[119] J. Cheng, M. Sulpizi, J. VandeVondele, M. Sprik, ChemCatChem 4 (2012) 636.

[120] S. Trasatti, Pure & Appl. Chem. 58 (1986) 955.

[121] A. Y. Lozovoi, A. Alavi, J. Kohanoff, R. M. Lynden-Bell, J. Chem. Phys. 115 (2001) 1661.

[122] V. Tripković, M. E. Björketun, E. Skúlason, J. Rossmeisl, Phys. Rev. B 84 (2011) 115452.

[123] H. Ishii, K. Sugiyama, E. Ito, K. Seki, Adv. Mater. 11 (1999) 605.

[124] J. Cheng, M. Sprik, Phys. Chem. Chem. Phys. (2012) DOI: 10.1039/C2CP41652B.

[125] S. Braun, W. R. Salaneck, M. Fahlman, Adv. Mater. 21 (2009) 1450.

[126] M. T. Greiner, M. G. Helander, W.-M. Tang, Z.-B. Wang, J. Qiu, Z.-H. Lu, Nature Mater. 11 (2012) 76.

[127] B. Hammer, L. B. Hansen, J. K. Nørskov, Phys. Rev. B 59 (1999) 7413.

[128] K. Laasonen, M. Sprik, M. Parrinello, R. Car, J. Chem. Phys. 99 (1993) 9080.

[129] R. Seidel, S. Thürmer, B. Winter, J. Phys. Chem. Lett. 2 (2011) 633.

[130] A. Bernas, S. Ferradini, J.-P. Jay-Gerin, Chem. Phys. 222 (1997) 151.

[131] V. I. Anisimov, F. Aryasetiawan, A. I. Lichtenstein, J. Phys.: Condens. Matter 9 (1997) 767.

[132] J. Enkovaara, C. Rostgaard, J. J. Mortensen, J. Chen, L. F. M. Dulak, J. Gavnholt, C. Glinsvad, V. Haikola, H. A. Hansen, H. H. Kristoffersen, M. Kuisma, A. H. Larsen, L. Lehtovaara, M.Ljungberg, O. Lopez- Acevedo, P. G. Moses, J. Ojanen, T. Olsen, V. Petzold, N. A. Romero, J.Stausholm-Møller, M. Strange, G. A. Tritsaris, M. Vanin, M. Walter, B. Hammer, H. Häkkinen, G. K. H. Madsen, R. M. Nieminen, J. K. Nørskov, M. Puska, T. T. Rantala, J. Schiøtz, K. S. Thygesen, K. W. Jacobsen, J. Phys.: Condens. Matter 22 (2010) 253202.

[133] J. M. Garcia-Lastra, C. Rostgaard, A. Rubio, K. S. Thygesen, Phys. Rev. B 80 (2009) 245427.

[134] G. S. Karlberg, T. F. Jaramillo, E. Skúlason, J. Rossmeisl, T. Bligaard and J. K. Nørskov, *Phys*. *Rev*. *Lett*., *2007,* 99, 126101.

[135] J. K. Nørskov, J. Rossmeisl, A. Logadottir, L. Lindqvist, J. R. Kitchin, T. Bligaard and H. Jonsson, *J. Phys. Chem. B*, 2004, 108, 17886–17892.

[136] C. D. Taylor, S. A. Wasileski, J.-S. Filhol and M. Neurock, *Phys. Rev. B: Condens. Matter Mater. Phys.*, 2006, 73, 165402.

[137] J. Rossmeisl, E. Skúlason, M. E. Björketun, V. Tripkovic and J. K. Nørskov, *Chem. Phys. Lett.*, 2008, 466, 68–71.

[138] M. Otani and O. Sugino, *Phys. Rev. B: Condens. Matter Mater. Phys.*, 2006, 73, 115407.

[139] J. Cheng and M. Sprik, *Phys. Chem. Chem. Phys.*, 2012, 14, 11245–11267.

[140] S. Schnur and A. Groß, *Catal. Today*, 2011, 165, 129–137.

[141] N. M. Markovic, S. T. Sarraf, H. A. Gasteiger and P. N. Ross, *J. Chem. Soc., Faraday Trans.*, 1996, 92, 3719–3725.

[142] R. Subbaraman, D. Tripkovic, D. Strmcnik, K.-C. Chang, M. Uchimura, A. P. Paulikas, V. Stamenkovic and N. M. Markovic, *Science*, 2011, 334, 1256–1260.

[143] W. Sheng, H. A. Gasteiger and Y. Shao-Horn, *J. Electrochem. Soc.*, 2010, 157, B1529–B1536.

[144] R. Gisbert, G. García and M. T. M. Koper, *Electrochim. Acta*, 2011, 56, 2443–2449.

[145] S. Trasatti, *Pure Appl. Chem.*, 1986, 58, 955–966.

[146] V. Tripkovic, M. E. Björketun, E. Skúlason and J. Rossmeisl, *Phys. Rev. B: Condens. Matter Mater. Phys.*, 2011, 84, 115452

[147] *Dacapo pseudopotential code*, URL: https://wiki.fysik.dtu.dk/dacapo, Center for Atomic-scale Materials Design (CAMD), Technical University of Denmark, Lyngby, 2010.

[148] J. J. Mortensen, L. B. Hansen and K. W. Jacobsen, *Phys. Rev. B: Condens. Matter Mater. Phys.*, 2005, 71, 035109.

[149] J. Enkovaara, C. Rostgaard, J. J. Mortensen, J. Chen, L. F. M. Dułak, J. Gavnholt, C. Glinsvad, V. Haikola, H. A. Hansen, H. H. Kristoffersen, M. Kuisma, A. H. Larsen, L. Lehtovaara, M. Ljungberg, O. Lopez-Acevedo, P. G. Moses, J. Ojanen, T. Olsen, V. Petzold, N. A. Romero, J. tausholm-Møller, M. Strange, G. A. Tritsaris, M. Vanin, M. Walter, B. Hammer, H. Häkkinen, G. K. H. Madsen, R. M. Nieminen, J. K. Nørskov, M. Puska, T. T. Rantala, J. Schiøtz, K. S. Thygesen and K. W. Jacobsen, *J. Phys.: Condens. Matter*, 2010, 22,253202.

[150] S. R. Bahn and K. W. Jacobsen, *Comput. Sci. Eng.*, 2002, 4, 56–66.

[151] B. Hammer, L. B. Hansen and J. K. Nørskov, *Phys. Rev. B: Condens. Matter Mater. Phys.*, 1999, 59, 7413–7421.

[152] E. Skúlason, V. Tripkovic, M. E. Björketun, S. Gudmundsdóttir, G. S. Karlberg, J.Rossmeisl, T. Bligaard, H. Jónsson and J. K. Nørskov, *J. Phys. Chem. C*, 2010, 114, 18182–18197.

[153] H. Ogasawara, B. Brena, D. Nordlund, M. Nyberg, A. Pelmenschikov, L. G. M. Pettersson and A. Nilsson, *Phys.Rev. Lett.*, 2002, 89, 276102.

[154] M. Pourbaix, *Atlas of electrochemical equilibria in aqueous solutions*, Pergamon Press, 1966.

[155] N. Garcia-Araez, V. Climent, E. Herrero, J. M. Feliu and J. Lipkowski, *Electrochim. Acta*, 2006,

51, 3787–3793.

[156] A. Peremans and A. Tadjeddine, *Phys. Rev. Lett.*, 1994, 73, 3010–3013.

[157] G. Jerkiewicz, G. Vatankhah, S.-i. Tanaka and J. Lessard, *Langmuir*, 2011, 27, 4220–4226.

[158] K. J. P. Schouten, M. J. T. C. van der Niet and M. T. M. Koper, *Phys. Chem. Chem. Phys.*, 2010, 12, 15217–15224.

[159] J. Rossmeisl, J. K. Nørskov, C. D. Taylor, M. J. Janik and M. Neurock, *J. Phys. Chem. B*, 2006, 110, 21833–21839.

[160] M. van der Niet, N. Garcia-Araez, J. Hernandez, J. M. Feliu and M. Koper, *Catal. Today*, 2013, 202, 105–113.

[161] J. K. Nørskov, J. Rossmeisl, A. Logadottir, L. Lindqvist, J. R. Kitchin, T. Bligaard and H. Jónsson, *J. Phys. Chem. B* **108** (2004) 17886−17892.

[162] J. Greeley, T. F. Jaramillo, J. Bonde, I. Chorkendorff and J. K. Nørskov, *Nature Mater.* **5** (2006) 909−913.

[163] M. E. Björketun, A. S. Bondarenko, B. L. Abrams, I. Chorkendorff and J. Rossmeisl, *Phys. Chem. Chem. Phys.* **12** (2010) 10536−10541.

[164] N. Bonnet and N. Marzari, *Phys. Rev. Lett.* **110** (2013) 086104.

[165] Rossmeisl, J., Chan, K., Ahmed, R., Tripkovic, V., & Björketun, M. E. (2013). pH in atomic scale simulations of electrochemical interfaces. *Physical Chemistry Chemical Physics*, *15*(25), 10321-10325. 10.1039/c3cp51083b

[166] S. Schnur and A. Groβ, *New J. Phys.* **11** (2009) 125003.

[167] G. S. Karlberg, T. F. Jaramillo, E. Skúlason, J. Rossmeisl, T. Bligaard and J. K. Nørskov, *Phys. Rev. Lett.* **99** (2007) 126101.

[168] E. Skúlason, V. Tripkovic, M .E. Björketun, S. Gudmundsdóttir, G. S. Karlberg, J Rossmeisl, T. Bligaard, H Jónsson and J. K. Nørskov, *J. Phys. Chem. C* 114, 18182-18197 (2010).

[169] E. Skúlason, G. S. Karlberg, J. Rossmeisl, T. Bligaard, J. Greeley, H. Jónsson and J.K. Nørskov, *Phys. Chem. Chem. Phys.* 9, 3241 (2007).

[170] M. Otani, I. Hamada, O. Sugino, Y. Morikawa, Y. Okamoto and T. Ikeshoji, *J. Phys. Soc. Jpn.* 77, 024802 (2008).

[171] C. D. Taylor, S. A. Wasileski, J.-S. Filhol and M. Neurock, *Phys. Rev. B* 73, 165402 (2006).

[172] R. Jinnouchi and A. B. Anderson, *J. Phys. Chem. C.* 112, 8747-8750 (2008).

[173] M. J. Janik, C. D. Taylor and M. Neurock, *J. Electrochem. Soc.* 156, B126-B135 (2009).

[174] J. S. Filhol and M. Neurock, Angew. *Chem. Int. Ed.* 45, 402 (2006).

[175] Björketun, M., Zeng, Z., Ahmed, R., Tripkovic, V., Thygesen, K. S., & Rossmeisl, J. (2013). Avoiding pitfalls in the modeling of electrochemical interfaces. *Chemical Physics Letters*, *555*, 145-148. 10.1016/j.cplett.2012.11.025

[176] J. Durst, A. Siebel, C. Simon, F. Hasch, J. Herranz and H. A. Gasteiger, *Energy Environ. Sci.* **7** (2014) 2255−2260.

[177] Alexander S. Bondarenko, Ifan E. L. Stephens, Heine A. Hansen, Francisco J. Perez-Alonso, Vladimir Tripkovic, Tobias P. Johansson, Jan Rossmeisl, Jens K. Nørskov, and Ib Chorkendorff, *Langmuir* 2011, 27(5), 2058–2066

[178] Antonio Berná, Víctor Climent, Juan M. Feliu, *Electrochemistry Communications* 9 (2007), 2789– 2794

[179] D. Strmcnik, D. Tripkovic, D. van der Vliet, V. Stamenkovic, N.M. Marković, *Electrochemistry Communications*, 10 (2008) 1602–1605

[180] Marc T.M. Koper, *Electrochimica Acta* 56 (2011) 10645– 10651

[181] DeHao Chen, JinYu Ye, ChangDeng Xu, Xin Li, JunTao Li, ChunHua Zhen, Na Tian, ZhiYou Zhou, ShiGang Sun, *Science China Chemistry*, Volume 55, Issue 11, pp 2353-2358

Included Papers

Paper I

Avoiding pitfalls in the modeling of electrochemical interfaces.

Mårten Björketun, Zhenhua Zeng, Rizwan Ahmed, Vladimir Tripkovic, Kristian S. Thygesen, Jan Rossmeisl

Chemical Physics Letters, Vol. 555, 2013, p. 145-148.

Chemical Physics Letters 555 (2013) 145–148

Contents lists available at SciVerse ScienceDirect

Chemical Physics Letters

journal homepage: www.elsevier.com/locate/cplett

Avoiding pitfalls in the modeling of electrochemical interfaces

Mårten E. Björketun *, ZhenHua Zeng, Rizwan Ahmed, Vladimir Tripkovic, Kristian S. Thygesen, Jan Rossmeisl

Center for Atomic-scale Materials Design, Department of Physics, Technical University of Denmark, DK-2800 Lyngby, Denmark

ARTICLE INFO

Article history:
Received 8 July 2012
In final form 12 November 2012
Available online 24 November 2012

ABSTRACT

Alignment of metal and molecular electronic energy levels at electrode–electrolyte interfaces is investigated using density functional theory. Three different regimes exhibiting qualitatively different energy level alignments are observed. The regimes are roughly defined by the size of the metal work function relative to the ionization potential and/or electron affinity of the electrolyte. It is demonstrated that proper matching of these quantities is essential for successful *ab initio* modeling of electrochemical interfaces and it is further discussed how such matching can be obtained by careful tailoring of the interfacial atomic structure.

Electrochemical cells have a unique capability to perform efficient conversions between free energy stored in chemical fuels and potential differences, which can be transformed into electrical work [1]. The energy conversion occurs through charge transfer reactions taking place over the electrochemical interface, the border region separating the electron-conducting electrode and the electrically insulating but ion-conducting electrolyte. The efficiency of conversion is, to a great extent, determined by the energetics of single charge transfer reactions. Therefore, it is of utmost importance to gain an atomic-level understanding of the electrochemical interface.

In the last decade, density functional theory (DFT) based atomic and electronic structure simulations of electrochemical interfaces have emerged [2–14]. The objective of these simulations is to study charge transfer reactions and electrochemical properties that usually depend on the electrode potential. Hence, a scheme for assessing the potential is indispensable. Most commonly, the work function, evaluated in vacuum outside the electrolyte, is used as a measure of the electrode potential [3,11,15,16].

The DFT methods have indeed proven valuable and promising in providing atomic level descriptions of various properties of the electrochemical interface [4,7,9,11,17]. In this Letter, however, we address a critical issue regarding the electronic structure of the interface, the alignment of metal and molecular electronic energy levels [18], that so far, with a few notable exceptions [12,14,19], has been largely overlooked in *ab initio* electrochemical modeling. We demonstrate that the HOMO and LUMO levels of the isolated electrolyte have to straddle the Fermi level of the metal electrode in order for the combined system to qualify as an adequate model of the electrochemical interface. In particular, we show that when the work function of the bare metal falls outside the HOMO–LUMO range, the interface becomes conductive and charge is transferred between the originally neutral electrode and electrolyte. For such systems it is not possible to model changes in the electrode potential. Although a conductive interface might sometimes be a true physical effect, it is often a consequence of the unphysical self-interaction experienced by electrons in conventional DFT, which introduces errors in calculated electron affinities and ionization potentials. Spurious interfacial charge transfer has implications beyond the field of electrochemical interface modeling. For instance, it will give an additional contribution to work functions calculated for metal–water systems, thus making comparisons between experimental and theoretical structures ambiguous. Finally, aside from pointing out the pitfalls faced when modeling electrochemical interfaces, we also describe how they can be avoided by controlling the atomic configuration and the corresponding electronic structure.

Most of the DFT calculations are performed at the GGA–RPBE [20] level of exchange–correlation, using DACAPO [21], a plane-wave Vanderbilt ultrasoft pseudopotential [22] code. Metal lattice constants are optimized at the RPBE level and are then used in all calculations. Interfaces are modeled by periodically repeated 3×2 unit cells wide and 3 layer thick metal slabs with an electrolyte film adsorbed on top. Periodic images are separated by at least 12 Å of vacuum in the direction perpendicular to the metal surface, a setup that ensures convergence of work functions and energies. When applicable, the dipole correction is used to decouple the electrostatic interaction between periodically repeated slabs [23]. The Kohn–Sham equations are solved using a plane-wave cutoff of 26 Ry, and the k-points are sampled using a $4 \times 6 \times 1$ Monkhorst–Pack k-point grid [24]. In addition, some GGA + U calculations [25] are carried out using GPAW [26,27], a real-space projector-augmented wave (PAW) [28] code, with a grid spacing of about 0.18 Å.

* Corresponding author.
E-mail address: martebjo@fysik.dtu.dk (M.E. Björketun).

0009-2614/$ - see front matter © 2012 Elsevier B.V. All rights reserved.
http://dx.doi.org/10.1016/j.cplett.2012.11.025

Figure 1 shows an example of an electrochemical metal–water interface. The surface charge density and hence the electrode potential can be varied either by injecting (removing) electrons into (from) the metal slab [3] or by adding hydrogen atoms to the first water layer [6,11]. In the former case the additional negative (positive) charge is compensated by a background charge of opposite sign to ensure overall charge neutrality of the computational cell. In the latter case, the additional hydrogen atoms spontaneously separate into protons that become solvated in the water bilayer and electrons that end up on the surface of the metal slab. Again the computational cell remains charge neutral. In the example shown in Figure 1 the latter approach has been adopted. The electrostatic potential (EP) energy has been plotted for two different proton concentrations. It is seen that an increase in proton concentration, and concomitant increase in surface charge density, reduces the EP energy in the vacuum region outside the electrolyte, relative to the Fermi level; that is, it reduces the work function Φ' which is a measure of the electrode potential [3,15,16]. This interface model thus allows the bias to be varied and electrochemical reactions to be studied at different potentials.

The explanation as to why Φ' can be varied in the above system is found in the relative size of the metal work function, Φ_M, compared to the electron affinity, E_A, and ionization potential, E_I, of the electrolyte. Based on the relative size, the so-called integer charge transfer model [29], applicable to interfaces with weak interaction between electrodes and electrolytes, identifies three different regimes, each with a unique alignment of metal and molecular electronic energy levels. More precisely, the three regimes (or regions) are defined by $\Phi_M \lesssim E_A$ (region I), $E_A \lesssim \Phi_M \lesssim E_I$ (region II), and $\Phi_M \gtrsim E_I$ (region III). For a comprehensive discussion of the alignment of electronic levels in these regimes the reader is referred to Refs. [18,29]. Here we will introduce only the bare minimum of quantities and concepts needed for the ensuing discussion.

The model interface displayed in Figure 1 belongs to region II. Since $\Phi_M > E_A$ for this interface, the energy cost of removing an electron from the metal is larger than the energy gained by adding it to the electrolyte. Likewise, since $E_I > \Phi_M$, the cost of removing an electron from the electrolyte will not be compensated by the energy gained when adding it to the metal. Consequently, there will be no spontaneous charge transfer across the interface when the metal and electrolyte are brought into contact to form the interface. It also means that no additional dipole will build up at the interface and the metal and electrolyte vacuum levels will therefore stay aligned upon formation of the interface, as illustrated in Figure 2. As a direct result of the vacuum level alignment, the electrolyte HOMO and LUMO levels straddle the Fermi level in the combined system.

A subsequent increase or reduction of the charge density on the metal surface – for instance in response to an applied electrode potential – adds an extra contribution, $\Delta\Phi_{polar}$, to the surface dipole energy, which shifts the electronic energy levels of the electrolyte relative to the Fermi level (cf. gray lines in Figure 2). This shift should be reflected in a corresponding change of Φ' (also indicated in Figure 2), something that can be verified and quantified by DFT calculations. Figure 3b demonstrates the response of Φ' to a change in surface charge density for another system belonging to region II, a Pt(1 1 1) surface covered with a single water bilayer with hydrogen pointing down. Here, in contrast to the example shown in Figure 1, a change in surface charge density is obtained by explicit injection of fractional charges into the metal slab. As expected, Φ' depends sensitively on the surface charge density. Addition of 0.5 electrons to the uncharged cell with 12 surface atoms reduces Φ' with approximately 1 eV, and addition of another half electron reduces it 1 eV further.

In systems belonging to region I, the metal donates electrons to the LUMO level of the electrolyte when the interface is being formed. After equilibrium has been established, the Fermi level will therefore be pinned to states close to the LUMO. Consequently, a change in surface charge density will not affect Φ' much; it stays essentially fixed as it will be given roughly by the constant difference between the LUMO and $V_{mol,o}$, the near-field vacuum level outside the electrolyte. This kind of energy alignment is observed for (1 1 1)-terminated Li artificially constrained to the fcc structure, with a two bilayer thick hydrogen-pointing-up water film adsorbed on top (see Figure 3a). Upon charging, Φ' is found to decrease somewhat due to slightly increased occupation of the LUMO in the combined system. We note that although this example gives a clear illustration of the typical Fermi level pinning in region I, the system is fairly unrealistic; this particular interface is expected to be highly unstable since Li reacts with water. A more relevant example would probably be a metal–oxide contact. DFT's tendency to place LUMO levels too far below the vacuum level could easily result in pinning to LUMO-derived states even in systems where this is not supposed to occur.

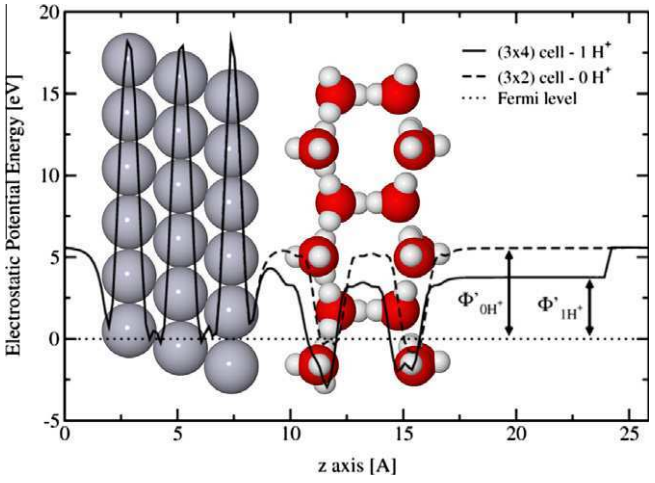

Figure 1. Atomic-scale model of a Pt-water interface, showing the variation of the electrostatic potential (EP) energy averaged parallel to the surface. The EP energy is reported for two different surface charge densities corresponding to two different electrode potentials. The work functions Φ'_{1H^+} and Φ'_{0H^+} measure the absolute value of the EP energy in the vacuum region outside the electrolyte, relative to the Fermi level, for an electrolyte with and without explicit counterions in the outer Helmholtz layer.

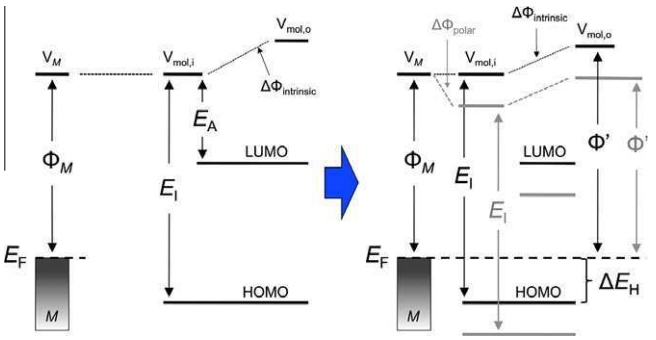

Figure 2. Alignment of metal and molecular energy levels upon formation of an interface characterized by $E_A \lesssim \Phi_M \lesssim E_I$. Isolated systems are shown on the left side and the combined metal-electrolyte system on the right. The near-field vacuum level on the inner side of the electrolyte, $V_{mol,i}$, differs from the level on the outer side, $V_{mol,o}$, if the molecule possesses an intrinsic dipole moment, $\Delta\Phi_{intrinsic}$. The gray lines indicate the shift of molecular levels in response to a change in surface charge density. The HOMO offset ΔE_H as well as the work function Φ' of the combined system change accordingly.

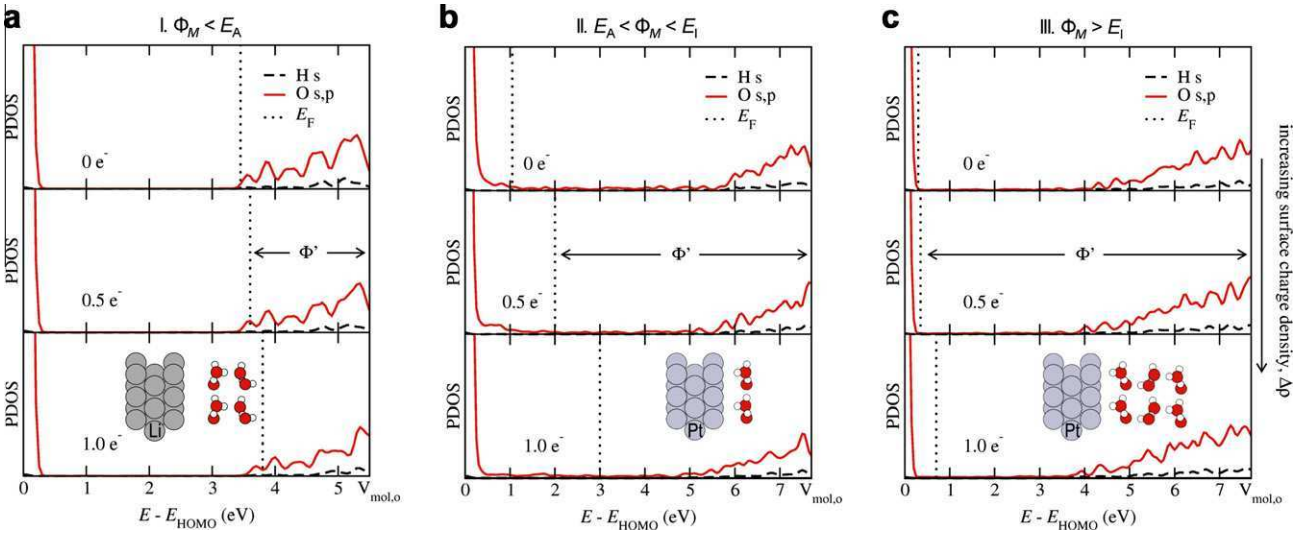

Figure 3. Energy level alignment as a function of surface charge density in electrode–electrolyte systems belonging to regions I, II and III. Region I is represented by a Li-water system with $\Phi_M \approx 3.4$ eV and $E_A \approx 5.1$ eV, region II by a Pt-water system with $\Phi_M \approx 5.6$ eV, $E_A \approx 1.2$ eV and $E_I \approx 6.4$ eV, and region III by a Pt-water system with $\Phi_M \approx 5.6$ eV and $E_I \approx 2.1$ eV. The number of extra electrons added per 12 surface metal atoms is reported in each panel. As a result of the essentially constant HOMO offset in regions I and III, a change in surface charge density will not affect the work function Φ'. In region II, the HOMO level is no longer pinned relative to the Fermi level, and an increase or reduction of the surface charge density will be reflected in a corresponding change of Φ'.

In region III, charge will flow from the HOMO of the electrolyte to the Fermi level of the electrode when the two components are brought into contact. The shallow positive states thus created in the electrolyte will pin the Fermi level once the interface has been formed. The resulting HOMO offset, ΔE_H, (defined in Figure 2) is small and virtually unaffected by a change in the surface charge density. Hence, Φ' is again insensitive to changes in the surface charge density of the electrode. In Figure 3c this is illustrated by a Pt (1 1 1) surface covered with a three bilayer thick water film with hydrogen pointing down in all three layers.

When Φ' is virtually unaffected by charging, as in regions I and III, it is possible to change the free energy of a charge transfer reaction without altering the electrode potential. Moreover, the interface capacitance becomes unrealistically large since a small change in potential can change the free energy of the interface dramatically. An electrochemical model that behaves like that is clearly unphysical. The electronic problem can, however, often be addressed by turning individual dipoles in the electrolyte layer because a minor change in the atomic geometry might be enough to shift the system from region I or III to region II. In connection to this discussion, it is important to note that using an experimentally correct atomic configuration does not guarantee that the system will end up in region II. The necessary requirements on the electronic structure might still not be met due to limitations of DFT. We will discuss these limitations later.

We further quantify the energy level alignment discussed above by more electronic structure calculations. Based on experimental data, Greiner et al. recently demonstrated a strong interdependence between ΔE_H and $\Phi_M - E_I$ in systems of organic molecules adsorbed on metal oxides [30]. Our metal-electrolyte systems exhibit a similar relationship; this is seen in Figure 4, which reports ΔE_H vs. $\Phi_M - E_I$ for a large set of metal-water interfaces (various metals and orientations of the water molecules) and a few metal–oxide (Ni–YSZ) interfaces.

As suggested already by Figures 2 and 3a–c, ΔE_H is large in region I (roughly given by the HOMO–LUMO gap), varies linearly with a slope of one in region II (its size is approximately $\Phi_M - E_I$), and is small and fairly constant in region III. While the border between regions II and III in Figure 4 is universal in the present representation (ΔE_H vs. $\Phi_M - E_I$), the border between

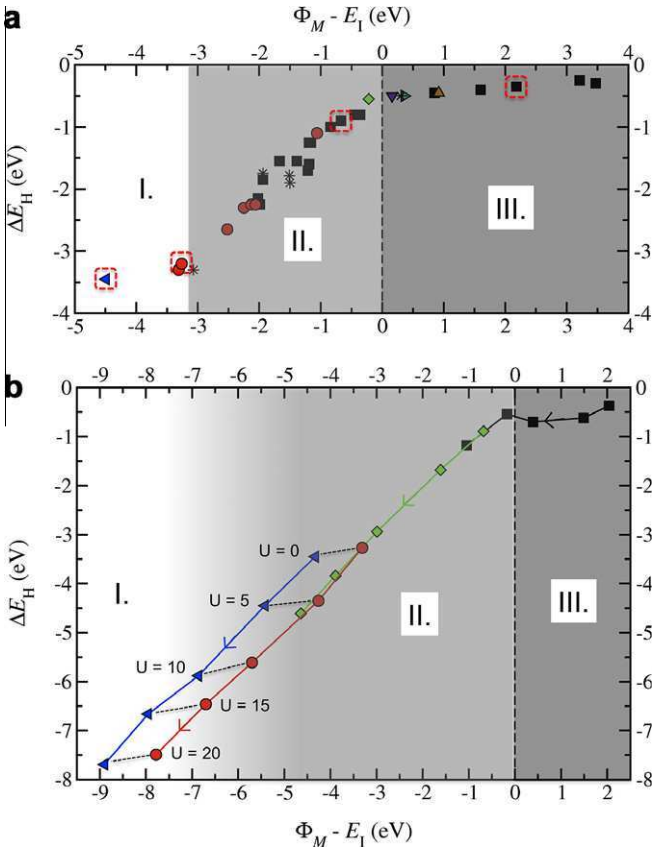

Figure 4. HOMO offset vs. the difference between metal work function and molecular ionization potential. The data points cover three qualitatively different regimes: I. $\Phi_M < E_A$, II. $E_A < \Phi_M < E_I$ and III. $\Phi_M > E_I$. Only systems in region II are suitable for theoretical studies of potential dependent electrochemical properties. (a) RPBE calculations of (□) Pt-water, (○) Ag-water, (◇) Au-water, (△) Ir-water, (◁) Li-water, (▽) Pd-water, (▷) Re-water, (+) Rh-water, (×) Ru-water and (∗) Ni-YSZ. (b) RPBE + U calculations of the four systems highlighted in (a): (□) Pt-dd, (◇) Pt-du, (○) Ag-uu and (◁) Li-uu [d (u) denotes a water bi-layer with a net dipole pointing down (up), toward (from) the metal surface]. The arrows indicate the translation of the data points when U is increased from 0 to 20 through the set {0,5,10,15,20}.

regions I and II is not, since E_A may vary from one electrolyte to another. If the entire curve in Figure 4a had been mapped out using only one specific electrolyte but different electrodes, covering a large range of Φ_M values, then the width of region II would have been about the same as the HOMO–LUMO gap of that electrolyte.

Due to the self-interaction problem in conventional DFT, the HOMO levels of the water films will be too high in energy and hence the calculated E_I's too small. For bulk water the discrepancy between DFT [31] and experimental [32] estimates of the HOMO level position is typically several eV and for the band gap the difference is similar [31,33]. The positioning of the HOMO level can be improved by GGA + U calculations [25], where orbital-dependent interactions that push the HOMO down are introduced. We have performed such calculations at the RPBE level for four different metal–water systems. For each system, five different U's, $U \in \{0, 5, 10, 15, 20\}$, have been applied to the oxygen-2p orbitals. The result is reported in Figure 4b. Clearly, the main effect of the U term is to widen region II by an amount given by the change in the HOMO–LUMO gap, and to shift the data points in region II down by an amount corresponding to the change in E_I. Also, systems originally in region III, which are mainly Pt-based, may move into region II as a result of the increased ionization potential. However, given the use of a U value that positions the HOMO level correctly in water layers far from the metal surface, the GGA + U calculations will likely overestimate the width of region II. In a real physical system, the dynamic image charge effect, not captured by DFT, will move the HOMO level up and the LUMO level down when the water film approaches the metal [34], thus reducing the width of region II.

Furthermore, it should be noted that the true border between regions II and III (if defined as the point of transition between a linearly varying and constant ΔE_H) is actually located at a slightly negative $\Phi_M - E_I$, as the cost to remove an electron from the electrolyte and to form an electronically and geometrically fully relaxed state is smaller than E_I [29]. A closer look at Figure 4a and b revels this offset. For similar reasons, the border between regions I and II will be located to the right of the position suggested by E_A. These effects further narrow region II. Nevertheless, since conventional DFT severely underestimates the width of the HOMO–LUMO gap, we still expect that most Pt-water systems belong to region II in reality.

Finally, we note that the relation between ΔE_H and $\Phi_M - E_I$, shown in Figure 4, with a sharp transition close to $\Phi_M - E_I = 0$, holds only as long as the chemical interaction between electrode and electrolyte is weak [29]. The picture becomes blurred if chemical bonds start forming between them because of the accompanying charge redistribution. Significant charge redistribution is frequently observed when metal–water systems are modeled using PBE or a similar exchange–correlation functional [17]. Compared to RPBE, PBE yields smaller separation and stronger interaction between metal and water [17]. However, if a U term is added to the PBE calculation, and gradually increased, the metal–water interaction will steadily weaken and the metal–water separation will expand. Eventually the distance and interaction will saturate, the RPBE result will be more or less recovered, and the main features of the curve in Figure 4 will be reproduced. This means that the artificially high HOMO level in water is directly responsible for many theoretical reports of charge transfer between neutral water films and metals.

In this Letter, we have analyzed the electronic structure of electrochemical interfaces in detail. In particular, we have shown that the HOMO and LUMO levels of the isolated electrolyte have to straddle the Fermi level of the metal electrode in order for the combined system to behave as an electrochemical interface. As a direct consequence of conventional DFT's notorious underestimation of the HOMO–LUMO gap of the electrolyte, electrode–electrolyte interface models constructed without special care could exhibit an unphysical charge transfer between the two neutral components. In such systems the key feature of a proper electrochemical interface, a tunable electrode potential, is lost. The spurious charge transfer also has implications beyond electrochemical interface modeling. It affects the calculated work function which could otherwise be used to distinguish between potential adsorbate structures.

The CASE initiative is funded by the Danish Ministry of Science, Technology and Innovation. Support from DCSC, DCTI's FTP program and SERC is gratefully acknowledged. The authors thank Joost VandeVondele and Michiel Sprik for fruitful discussions.

References

[1] B.C.H. Steele, A. Heinzel, Nature 414 (2001) 345.
[2] Y. Cai, A.B. Anderson, J. Phys. Chem. B 108 (2004) 9829.
[3] J.-S. Filhol, M. Neurock, Angew. Chem. Int. Ed. 45 (2006) 402.
[4] M. Otani, O. Sugino, Phys. Rev. B 73 (2006) 115407.
[5] P. Vassilev, R.A. van Santen, M.T.M. Koper, J. Chem. Phys. 122 (2005) 054701.
[6] J. Rossmeisl, E. Skúlason, M.E. Björketun, V. Tripkovic, J.K. Nrskov, Chem. Phys. Lett. 466 (2008) 68.
[7] R. Jinnouchi, A.B. Anderson, Phys. Chem. C 112 (2008) 8747.
[8] S. Schnur, A. Gro, New J. Phys. 11 (2009) 125003.
[9] M.J. Janik, C.D. Taylor, M. Neurock, J. Electrochem. Soc. 156 (2009) B126.
[10] E. Santos, A. Lundin, K. Pötting, P. Quaino, W. Schmickler, Phys. Rev. B 79 (2009) 235436.
[11] E. Skúlason et al., J. Phys. Chem. C 114 (2010) 18182.
[12] J. Cheng, M. Sprik, Phys. Rev. B 82 (2010) 081406.
[13] S. Schnur, A. Gro, Catal. Today 165 (2011) 129.
[14] J. Cheng, M. Sulpizi, J. VandeVondele, M. Sprik, ChemCatChem 4 (2012) 636.
[15] S. Trasatti, Pure Appl. Chem. 58 (1986) 955.
[16] A.Y. Lozovoi, A. Alavi, J. Kohanoff, R.M. Lynden-Bell, J. Chem. Phys. 115 (2001) 1661.
[17] V. Tripkovic, M.E. Björketun, E. Skúlason, J. Rossmeisl, Phys. Rev. B 84 (2011) 115452.
[18] H. Ishii, K. Sugiyama, E. Ito, K. Seki, Adv. Mater. 11 (1999) 605.
[19] J. Cheng, M. Sprik, Phys. Chem. Chem. Phys. (2012), http://dx.doi.org/10.1039/C2CP41652B.
[20] B. Hammer, L.B. Hansen, J.K. Nrskov, Phys. Rev. B 59 (1999) 7413.
[21] Dacapo Pseudopotential Code, URL: https://wiki.fysik.dtu.dk/dacapo, Center for Atomic-scale Materials Design (CAMD), Technical University of Denmark, Lyngby, 2010
[22] D. Vanderbilt, Phys. Rev. B 41 (1990) 7892.
[23] L. Bengtsson, Phys. Rev. B 59 (1999) 12301.
[24] H.J. Monkhorst, J.D. Pack, Phys. Rev. B 13 (1976) 5188.
[25] V.I. Anisimov, F. Aryasetiawan, A.I. Lichtenstein, J. Phys.: Condens. Matter 9 (1997) 767.
[26] J.J. Mortensen, L.B. Hansen, K.W. Jacobsen, Phys. Rev. B 71 (2005) 035109.
[27] J. Enkovaara et al., J. Phys.: Condens. Matter 22 (2010) 253202.
[28] P.E. Blöchl, Phys. Rev. B 50 (1994) 17953.
[29] S. Braun, W.R. Salaneck, M. Fahlman, Adv. Mater. 21 (2009) 1450.
[30] M.T. Greiner, M.G. Helander, W.-M. Tang, Z.-B. Wang, J. Qiu, Z.-H. Lu, Nature Mater. 11 (2012) 76.
[31] K. Laasonen, M. Sprik, M. Parrinello, R. Car, J. Chem. Phys. 99 (1993) 9080.
[32] R. Seidel, S. Thürmer, B. Winter, J. Phys. Chem. Lett. 2 (2011) 633.
[33] A. Bernas, S. Ferradini, J.-P. Jay-Gerin, Chem. Phys. 222 (1997) 151.
[34] J.M. Garcia-Lastra, C. Rostgaard, A. Rubio, K.S. Thygesen, Phys. Rev. B 80 (2009) 245427.

Paper II

pH in atomic scale simulations of electrochemical interfaces.

Jan Rossmeisl, Karen Chan, Rizwan Ahmed, Vladimir Tripkovic, Mårten E. Björketun

Physical Chemistry Chemical Physics, Vol. 15, No. 25, 2013, p. 10321-10325.

PCCP

RSC Publishing

COMMUNICATION

pH in atomic scale simulations of electrochemical interfaces

Cite this: *Phys. Chem. Chem. Phys.*, 2013, **15**, 10321

Received 12th March 2013,
Accepted 9th May 2013

DOI: 10.1039/c3cp51083b

www.rsc.org/pccp

Jan Rossmeisl,*[a] Karen Chan,[ab] Rizwan Ahmed,[a] Vladimir Tripković[a] and Mårten E. Björketun[a]

Electrochemical reaction rates can strongly depend on pH, and there is increasing interest in electrocatalysis in alkaline solution. To date, no method has been devised to address pH in atomic scale simulations. We present a simple method to determine the atomic structure of the metal|solution interface at a given pH and electrode potential. Using Pt(111)|water as an example, we show the effect of pH on the interfacial structure, and discuss its impact on reaction energies and barriers. This method paves the way for *ab initio* studies of pH effects on the structure and electrocatalytic activity of electrochemical interfaces.

Electrocatalysis is a central part of research and development in energy conversion technologies. Recent improvements in computational power and theory have allowed for density functional theory (DFT) calculations on electrochemical systems, which have driven the development of new electrocatalysts.[1–3] Currently, there are two main types of *ab initio* studies on electrochemical systems. Catalyst screening/optimization studies focus on adsorption free energies of reaction intermediates. Water and electric fields are often omitted to reduce the computational resources,[4] and the effect of potential is added *a posteriori via* the computational hydrogen electrode.[5] Fundamental studies focus on setting up an explicit electrode potential and electric field at the interface, *via* water layers, excess free charge, counter-ions, and counter electrodes.[6–10]

No existing approach addresses the effect of pH on the interfacial structure. Electrochemical reaction rates can, however, be strongly affected by solution pH, and there is increasing interest in the development of efficient electrocatalysts for alkaline environments.[11–14] Consideration of pH is thus a crucial challenge in *ab initio* simulations.

In this communication, we present a novel generalization of the computational hydrogen electrode to explicitly capture the respective pH and potential effects on the interface structure and its corresponding free energy. Using simple thermodynamic arguments, the method determines ground state interface structures as a function of pH and potential. As an example, we apply the method to a set of Pt(111)|water structures and determine the corresponding Pourbaix diagram. This method opens up the possibility for theoretical studies of pH effects on the structure and electrocatalytic activity of electrochemical interfaces.

We first review the Born–Haber cycle for hydrogen oxidation, shown in Fig. 1, which gives the relation among the electrode potential U, pH, and electrochemical potential of protons and electrons, $\mu_{H^+ + e^-}$.[15] With the chemical potential of gas phase H_2 as the zero reference point, the free energy of the reaction is

$$\mu_{H^+ + e^-} = \Delta_d G + \Delta_i G - \Phi_{H^+} - \Phi_{e^-}, \quad (1)$$

where $\Delta_d G$ is the $1/2H_2$ dissociation energy, $\Delta_i G$ the H ionization energy, and Φ_{H^+} and Φ_{e^-} the respective work functions of H^+ in solution and e^- in metal, measured with respect to vacuum just outside the solution phase. The pH dependence on $\mu_{H^+ + e^-}$ arises from the proton free energy, *i.e.*

$$\Phi_{H^+} = \Phi^0_{H^+} + 2.3\,kT \cdot \mathrm{pH} \quad (2)$$

The standard hydrogen electrode (SHE) potential corresponds to electrochemical equilibrium, $\mu_{H^+ + e^-} = 0$, at pH = 0, and the corresponding work function Φ_{e^-}(SHE) has the experimentally determined value of 4.44 eV.[15] The reversible hydrogen electrode (RHE) corresponds to $\mu_{H^+ + e^-} = 0$ at arbitrary pH.

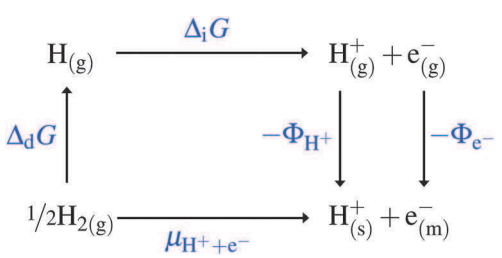

Fig. 1 The Born–Haber cycle for hydrogen oxidation.[15]

[a] *Center for Atomic-scale Materials Design, Department of Physics, Technical University of Denmark, DK-2800 Lyngby, Denmark. E-mail: jross@fysik.dtu.dk; Fax: +45 4593 2399; Tel: +45 4525 3166*
[b] *Department of Chemistry, Simon Fraser University, Burnaby, BC, Canada*

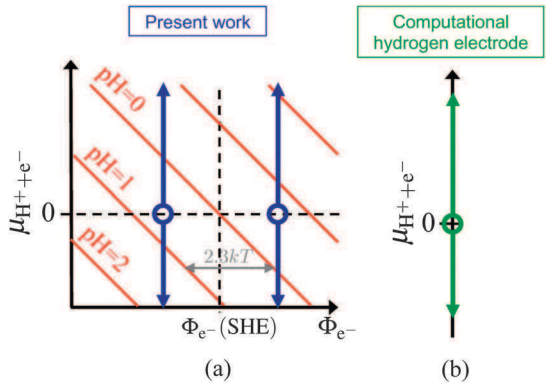

Fig. 2 (a) Eqn (3) mapped as red iso-pH lines on the (Φ_{e^-}, $\mu_{H^+ + e^-}$)-plane. Projections of G^{int} *vs.* $\mu_{H^+ + e^-}$ of the present work in blue arrows, where Φ_{e^-} is determined by the interfacial structure. (b) Projection of G^{int} *vs.* $\mu_{H^+ + e^-}$ of the computational hydrogen electrode in green arrows, where Φ_{e^-} is not considered.[5]

The electrochemical potential can be written simply in terms of Φ_{e^-}(SHE), pH, and Φ_{e^-},

$$\mu_{H^+ + e^-} = \Phi_{e^-}(\mathrm{SHE}) - 2.3\ kT \cdot \mathrm{pH} - \Phi_{e^-}. \quad (3)$$

The electrode potential U, which is determined by the interface dipoles in the computational model, is directly proportional to Φ_{e^-}.[15,16] Relative to, *e.g.*, the SHE reference electrode,

$$U_{\mathrm{SHE}} = \frac{\Phi_{e^-} - \Phi_{e^-}(\mathrm{SHE})}{e}. \quad (4)$$

Fig. 2(a) plots eqn (3) in red iso-pH lines on the (Φ_{e^-}, $\mu_{H^+ + e^-}$)-plane. The core of the method presented here is: for a given metal|solution structure, if Φ_{e^-} and $\mu_{H^+ + e^-}$ are known, the corresponding pH is determined *via* eqn (3).

We now describe an extrapolation scheme to determine the integral free energy, G^{int}, of interfacial structures on the (Φ_{e^-}, $\mu_{H^+ + e^-}$)-plane. For a given structure, Φ_{e^-} and the interface dipole are constant. The free energy per surface metal atom at electrochemical equilibrium, $\mu_{H^+ + e^-} = 0$, is

$$G^{\mathrm{int}}(\mu_{H^+ + e^-} = 0, \Phi_{e^-}) = \frac{G_{N,n} - G_{N,0}}{N} - \frac{1}{2}\frac{n}{N}G_{H_2}, \quad (5)$$

where n is the number of hydrogens (as $H^+ + e^-$, or as adsorbates, H_{ad}, OH_{ad}, and O_{ad}), N the number of surface metal atoms, $G_{N,n}$ the free energy of the metal|solution system of interest, $G_{N,0}$ the free energy of a reference system with no ions or adsorbates, and G_{H_2} the free energy of gas-phase H_2 under standard conditions. All G are straightforward to obtain *via* DFT and standard tables. If oxide species are present, n can be negative. Here, we consider equilibrium with the hydrogen reference electrode. We obtain the energy of this reference state with the computed energy of hydrogen gas. This approach allows us to avoid ill-defined simulations of protons in solution.

The corresponding pH of the given structure can be calculated from eqn (3). G^{int} for the interface at another pH, where $\mu_{H^+ + e^-} \neq 0$, is given by the linear extrapolation,

$$G^{\mathrm{int}}(\mu_{H^+ + e^-}, \Phi_{e^-}) = G^{\mathrm{int}}(\mu_{H^+ + e^-} = 0, \Phi_{e^-}) - \frac{n}{N}\mu_{H^+ + e^-}. \quad (6)$$

Fig. 2(a) illustrates, on the (Φ_{e^-}, $\mu_{H^+ + e^-}$)-plane, the extrapolation for two interface structures of different Φ_{e^-}, in blue arrows. We note that for a specific system, the extrapolation in eqn (6) is performed at constant Φ_{e^-}, *i.e.* the variations in $\mu_{H^+ + e^-}$ are due to changes in pH.

At any given Φ_{e^-} and pH, the relevant ground state structure corresponds to that with minimum G^{int}. To map ground state metal|solution interfacial structures at a range of Φ_{e^-} and $\mu_{H^+ + e^-}$ (or pH) a representative set of interfacial structures of varying charge density, adsorbate coverage, and water dipoles should be considered. Electric fields that are consistent with pH and potential are automatically set up.

Fig. 2 shows the distinction between the G^{int} extrapolations of the present work (a, blue arrows) and the computational hydrogen electrode (b, green arrows).[5] Computational hydrogen electrode calculations do not consider the work function Φ_{e^-}, and extrapolation of G^{int} to $\mu_{H^+ + e^-} \neq 0$ are all done along a single line. The effect of potential is only considered *a posteriori via* $\mu_{H^+ + e^-} = -eU_{RHE}$, not in the physical interface dipole. Effects of water structure and interface electric fields on G^{int} are therefore neglected. In the present analysis, we consider explicitly Φ_{e^-} as fixed by the interface dipole, and map G^{int} on the (Φ_{e^-}, $\mu_{H^+ + e^-}$)-plane at the given Φ_{e^-}. This approach thereby distinguishes contributions of potential and pH to $\mu_{H^+ + e^-}$. Water structures and electric fields that are consistent with the pH and potential are automatically included. We discuss below the implications of the current analysis on previous results.

The present analysis is general in that it places no restrictions on the atomic interface model considered. Nothing is preassumed about $G_{N,n}$ and $G_{N,0}$ in eqn (5) and (6), and any atomic scale simulation of the electrochemical interface must include this analysis in order to explicitly and correctly account for pH and potential. With interface and bulk protons at electrochemical equilibrium, μ_{H^+}(interface) = μ_{H^+}(bulk), we can consider interface models with a limited number of water layers, provided that they fully screen the interface electric fields.[7,17]

To illustrate the method, we apply it to a variety of Pt(111)|water structures and determine the corresponding Pourbaix diagram. We consider 1–2 layers of ice-like hexagonal water structures[7,16,18] of a range of dipole orientations, adsorbate coverages (H_{ad}-covered, bare Pt, a 1/2 dissociated water layer), and H^+ concentrations. All model systems were charge neutral, such that the positive charge of the protons was balanced by a negative surface charge on the metal. The total number of systems was limited to ~110. Ideally, many more structures should be calculated to sample the corresponding partition function. An extended set of potentially relevant structures could be generated by performing molecular dynamics simulations, starting from different low energy structures. This is however beyond the scope of the present study.

DFT calculations were carried out with the Dacapo or GPAW code, integrated with the Atomic Simulation Environment.[19–22] The RPBE functional was used for exchange and correlation.[23] The density cutoff for plane wave Dacapo calculations was 350 eV while the grid spacing for GPAW real-space calculations was 0.2 Å. A Fermi smearing of 0.1 eV was used and energies

were extrapolated to an electronic temperature of 0 K. All systems contained a periodic 3-layer Pt(111) slab and 1–2 water bilayers with at least 12 Å vacuum in the direction perpendicular to the surface. An optimized Pt lattice constant of 4.02 Å was used in all calculations. Unit cells of sizes (3 × 2), (3 × 3), (3 × 4), (3 × 6), and (6 × 4) were sampled with Monkhorst–Pack *k*-point grids (4 × 6), (4 × 4), (4 × 3), (4 × 2), and (2 × 3). In all cases, a dipole correction was applied.[24] The two bottom layers were constrained and all other atoms relaxed until the forces on them were less than 0.05 eV Å^{-1}. To obtain the free energies G, the zero point energies and entropies of protons and adsorbed hydrogens were taken from ref. 5 and 17. The reference energy structure corresponding to $G_{N,0}$ was a bare slab with water layer(s) of equal density of H-up and H-down waters. For each simulation, $G^{\mathrm{int}}(\mu_{\mathrm{H^+}+\mathrm{e^-}} = 0, \Phi_{\mathrm{e^-}})$ was calculated and $\Phi_{\mathrm{e^-}}$ was measured. $G^{\mathrm{int}}(\mu_{\mathrm{H^+}+\mathrm{e^-}}, \Phi_{\mathrm{e^-}})$ was then calculated according to eqn (6).

Fig. 3 shows G^{int} for three sample Pt(111)|water structures. G^{int} was linearly extrapolated at the three corresponding $\Phi_{\mathrm{e^-}}$ with eqn (6). Constant pH = 0, 7, 14 planes are mapped perpendicular to the ($\Phi_{\mathrm{e^-}}$, $\mu_{\mathrm{H^+}+\mathrm{e^-}}$)-plane (eqn (3)). Intersections of the 3 lines with the pH planes are highlighted with flat circles, marking the G^{int} of the 3 structures at those particular pH's.

Fig. 4(a) and (b) show the full set of considered water structures as projections of G^{int} onto the pH = 0 and pH = 14 planes, respectively. The SHE scale is shown along the bottom *x*-axis, and the RHE scale along the top *x*-axis. The legend shows the dipole orientation of the water structure, with H-up water indicated by ↑ and H-down by ↓. The H concentration, n/N, is indicated by the colorbar.

We obtain a simple Pt(111)|water Pourbaix diagram by interpolating the results for select proton/adsorbate coverages, n/N = −0.33, 0, 0.17, 1, and 1.17. For these coverages, we fit straight lines through the G^{int} *vs.* potential data at a range of pH (*cf.* Fig. 4),

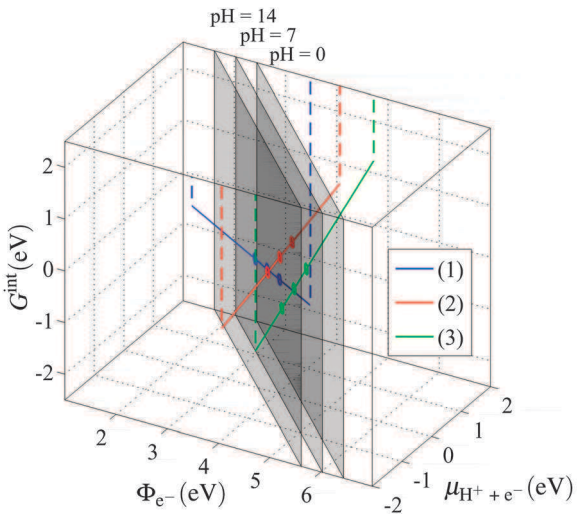

Fig. 3 Calculated G^{int} *vs.* $\Phi_{\mathrm{e^-}}$, $\mu_{\mathrm{H^+}+\mathrm{e^-}}$, for select Pt(111)|solution interfacial structures: (1) $\Phi_{\mathrm{e^-}}$ = 3.48 eV, n/N = 0.96, (2) $\Phi_{\mathrm{e^-}}$ = 4.06 eV, n/N = −0.22, (3) $\Phi_{\mathrm{e^-}}$ = 4.72 eV, n/N = −0.44. Dashed lines are shown as guides for the eye. Intersections of G^{int} with constant pH = 0, 7, 14 planes are marked with circles, indicating G^{int} at those particular pH.

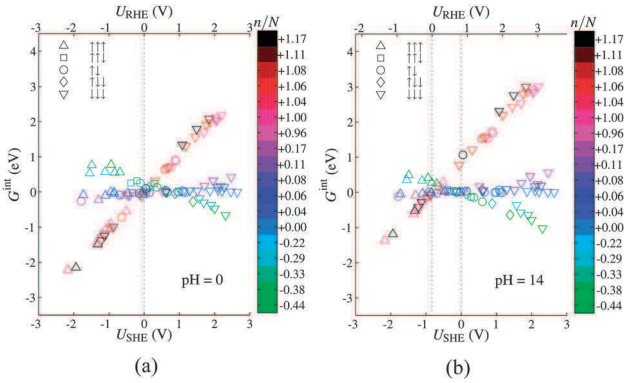

Fig. 4 Calculated G^{int} *vs.* U (*vs.* SHE and RHE) for all considered Pt(111)|solution interfacial structures, as projected onto (a) pH = 0 and (b) pH = 14 planes. The H concentration n/N is indicated by the colorbar, and the net dipole of the water by arrows.

and linearly interpolate both the G^{int} and dipole orientation. Then, at every U and pH, we pick out the most stable structure. The resultant Pourbaix diagram is shown in Fig. 5.

Consistent with experimental cyclic voltammograms and Pourbaix diagrams,[25,26] increasing U leads to a shift from a H_{ad} to OH_{ad} covered surface. The −0.059 eV/pH (−2.3 kT/pH) slope in the dotted lines dividing regions of different coverages show the expected U_{RHE} dependence of adsorbate coverage. Generally, as U increases and the surface changes from H_{ad} to OH_{ad} covered, water orientation tends to shift from H-up to H-down; this maximizes the hydrogen bonding between the adsorbates and water layer.[27,28] Water orients from H-down to H-up as pH increases, *i.e.* at low pH, H's tend to point toward the Pt surface. This trend is in agreement with that suggested by impedance spectroscopy.[29]

Calculated work functions are usually associated with a slight error, which introduces an uncertainty in the exact position of the systems relative to SHE and RHE. Correcting for this error

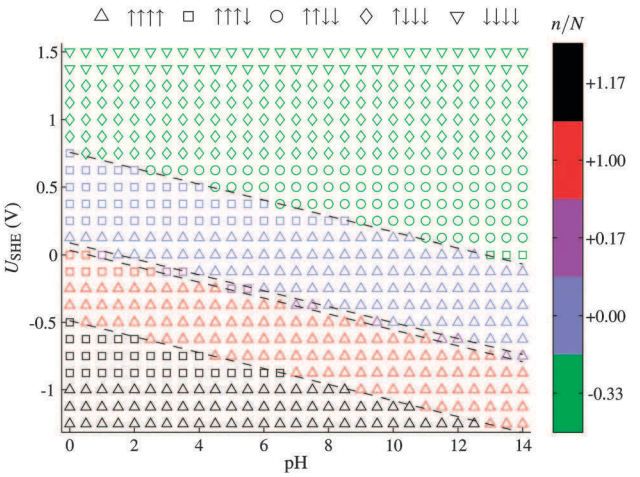

Fig. 5 Simulated Pourbaix diagram for Pt(111), showing the minimum energy structures as a function of pH and U_{SHE} for select excess H concentration n/N. Dotted lines dividing regions of different coverages have a −0.059 eV/pH slope, indicating the expected U_{RHE} dependence of adsorbate coverage.

would translate the systems along the different coverage lines in Fig. 4. This would change neither the preferred H coverage *vs.* SHE and RHE nor the observed trend in water orientation, but it could change the potential at which a certain water orientation starts to dominate. The precision of the method is strongly dependent on the accuracy of the DFT calculations. In any case, the trends allow us to at least distinguish between acidic, neutral, and alkaline conditions.

The Pt(111)|water example illustrates how pH and U affect the metal|solution interfacial structure. Essentially, the electrochemical potentials of both the protons and electrons are required to determine the ground state interfacial structure. Any U can be set up by a variety of adsorbate coverages, surface charge densities, and water dipole orientations. The electrochemical potential of the proton, determined by the pH, picks out the relevant minimum energy structure for a given U.

This new insight into the effect of pH on the interfacial structure does not necessarily invalidate previous computational hydrogen electrode studies, as long as the adsorbates of interest show negligible interactions with electric fields and water.[4,30] In this case, for a given adsorbate coverage, only differences in the water orientation contribute to the variation of G^{int} with Φ_{e^-}, and such contributions are negligible† compared to those of adsorbate binding energies. G^{int} then depends mainly on $\mu_{H^+ + e^-}$, not Φ_{e^-}, *i.e.* $G^{\mathrm{int}} \approx f(\mu_{H^+ + e^-}) = f(-eU_{\mathrm{RHE}})$. This leads to a simple U_{RHE} dependence of adsorbate coverage, as is the case for H_{ad} and OH_{ad} on Pt, considered above. G^{int} obtained *via* a computational hydrogen electrode and the present extrapolation (*cf.* Fig. 2) would then be very similar, even though water structures considered previously, if any, were likely not consistent with the ground state structures at the assumed pH and U. Where adsorbates are highly affected by field and/or water structure, *e.g.* adsorbates with substantial dipole moments,[30] and/or where adsorbate coverages do not show a simple U_{RHE} dependence,[31] the present analysis is required.

In reaction barrier studies, pH can have an important effect, as the barriers may be highly dependent on water structure. The ground state structures determined above could, for instance, explain the dramatically higher rates of hydrogen evolution on Pt in acidic solution than in basic ones.[11,12] At relevant electrode potentials and low pH, some hydrogens point toward the surface, which results in a very small barrier for proton transfer. At higher pH, all hydrogens point away from the surface, which gives rise to an extra barrier.

We have focussed on a simple model system of Pt(111)|water to illustrate the method. We expect more complex model systems with extended water layers, anions, and oxide species to further demonstrate the capabilities of the model, and detailed studies are in progress.

In summary, we have presented a simple scheme to determine the relevant interfacial structure at a given potential and pH, based on thermodynamic arguments. For any given interfacial structure containing any reaction intermediate of interest, the only required inputs to the analysis are the electron work function and the integral free energy, both easily determined using standard DFT. The method is in principle general, but as of today only rather idealized systems can be studied due to computational limitations. Applying the scheme to Pt(111)|water as an example, we show the pH to affect the adsorbate coverage and water orientation, which is expected to have an important impact on charge transfer reaction barriers. The method paves the way for *ab initio* studies of pH effects on the structure and electrocatalytic activity of electrochemical interfaces.

The CASE initiative is funded by the Danish Ministry of Science, Technology and Innovation. Support from DCSC is gratefully acknowledged. KC thanks NSERC for financial support.

† G^{int} ($\mu_{H^+ + e^-} = 0$) differences among neutral water layers of various dipoles are <0.1 eV.

References

1 J. Greeley, I. E. L. Stephens, A. S. Bondarenko, T. P. Johansson, H. A. Hansen, T. F. Jaramillo, J. Rossmeisl, I. Chorkendorff and J. K. Nørskov, *Nat. Chem.*, 2009, **1**, 552–556.
2 J. K. Nørskov, T. Bligaard, J. Rossmeisl and C. H. Christensen, *Nat. Chem.*, 2009, **1**, 37–46.
3 F. Calle-Vallejo and M. T. Koper, *Electrochim. Acta*, 2012, **84**, 3–11.
4 G. S. Karlberg, T. F. Jaramillo, E. Skúlason, J. Rossmeisl, T. Bligaard and J. K. Nørskov, *Phys. Rev. Lett.*, 2007, **99**, 126101.
5 J. K. Nørskov, J. Rossmeisl, A. Logadottir, L. Lindqvist, J. R. Kitchin, T. Bligaard and H. Jonsson, *J. Phys. Chem. B*, 2004, **108**, 17886–17892.
6 C. D. Taylor, S. A. Wasileski, J.-S. Filhol and M. Neurock, *Phys. Rev. B: Condens. Matter Mater. Phys.*, 2006, **73**, 165402.
7 J. Rossmeisl, E. Skúlason, M. E. Björketun, V. Tripkovic and J. K. Nørskov, *Chem. Phys. Lett.*, 2008, **466**, 68–71.
8 M. Otani and O. Sugino, *Phys. Rev. B: Condens. Matter Mater. Phys.*, 2006, **73**, 115407.
9 J. Cheng and M. Sprik, *Phys. Chem. Chem. Phys.*, 2012, **14**, 11245–11267.
10 S. Schnur and A. Groß, *Catal. Today*, 2011, **165**, 129–137.
11 N. M. Markovic, S. T. Sarraf, H. A. Gasteiger and P. N. Ross, *J. Chem. Soc., Faraday Trans.*, 1996, **92**, 3719–3725.
12 R. Subbaraman, D. Tripkovic, D. Strmcnik, K.-C. Chang, M. Uchimura, A. P. Paulikas, V. Stamenkovic and N. M. Markovic, *Science*, 2011, **334**, 1256–1260.
13 W. Sheng, H. A. Gasteiger and Y. Shao-Horn, *J. Electrochem. Soc.*, 2010, **157**, B1529–B1536.
14 R. Gisbert, G. García and M. T. M. Koper, *Electrochim. Acta*, 2011, **56**, 2443–2449.
15 S. Trasatti, *Pure Appl. Chem.*, 1986, **58**, 955–966.
16 V. Tripkovic, M. E. Björketun, E. Skúlason and J. Rossmeisl, *Phys. Rev. B: Condens. Matter Mater. Phys.*, 2011, **84**, 115452.
17 E. Skúlason, V. Tripkovic, M. E. Björketun, S. Gudmundsdóttir, G. S. Karlberg, J. Rossmeisl, T. Bligaard, H. Jónsson and J. K. Nørskov, *J. Phys. Chem. C*, 2010, **114**, 18182–18197.
18 H. Ogasawara, B. Brena, D. Nordlund, M. Nyberg, A. Pelmenschikov, L. G. M. Pettersson and A. Nilsson, *Phys. Rev. Lett.*, 2002, **89**, 276102.

19 *Dacapo pseudopotential code*, URL: https://wiki.fysik.dtu.dk/dacapo, Center for Atomic-scale Materials Design (CAMD), Technical University of Denmark, Lyngby, 2010.
20 J. J. Mortensen, L. B. Hansen and K. W. Jacobsen, *Phys. Rev. B: Condens. Matter Mater. Phys.*, 2005, **71**, 035109.
21 J. Enkovaara, C. Rostgaard, J. J. Mortensen, J. Chen, L. F. M. Dułak, J. Gavnholt, C. Glinsvad, V. Haikola, H. A. Hansen, H. H. Kristoffersen, M. Kuisma, A. H. Larsen, L. Lehtovaara, M. Ljungberg, O. Lopez-Acevedo, P. G. Moses, J. Ojanen, T. Olsen, V. Petzold, N. A. Romero, J. Stausholm-Møller, M. Strange, G. A. Tritsaris, M. Vanin, M. Walter, B. Hammer, H. Häkkinen, G. K. H. Madsen, R. M. Nieminen, J. K. Nørskov, M. Puska, T. T. Rantala, J. Schiøtz, K. S. Thygesen and K. W. Jacobsen, *J. Phys.: Condens. Matter*, 2010, **22**, 253202.
22 S. R. Bahn and K. W. Jacobsen, *Comput. Sci. Eng.*, 2002, **4**, 56–66.
23 B. Hammer, L. B. Hansen and J. K. Nørskov, *Phys. Rev. B: Condens. Matter Mater. Phys.*, 1999, **59**, 7413–7421.
24 L. Bengtsson, *Phys. Rev. B: Condens. Matter Mater. Phys.*, 1999, **59**, 12301.
25 M. Pourbaix, *Atlas of electrochemical equilibria in aqueous solutions*, Pergamon Press, 1966.
26 N. Garcia-Araez, V. Climent, E. Herrero, J. M. Feliu and J. Lipkowski, *Electrochim. Acta*, 2006, **51**, 3787–3793.
27 A. Peremans and A. Tadjeddine, *Phys. Rev. Lett.*, 1994, **73**, 3010–3013.
28 G. Jerkiewicz, G. Vatankhah, S.-i. Tanaka and J. Lessard, *Langmuir*, 2011, **27**, 4220–4226.
29 K. J. P. Schouten, M. J. T. C. van der Niet and M. T. M. Koper, *Phys. Chem. Chem. Phys.*, 2010, **12**, 15217–15224.
30 J. Rossmeisl, J. K. Nørskov, C. D. Taylor, M. J. Janik and M. Neurock, *J. Phys. Chem. B*, 2006, **110**, 21833–21839.
31 M. van der Niet, N. Garcia-Araez, J. Hernandez, J. M. Feliu and M. Koper, *Catal. Today*, 2013, **202**, 105–113.

Paper III

Influence of the Electrochemical Interface on adsorbed H.

Rizwan Ahmed, Martin H. Hansen, Mårten E. Björketun, Jan Rossmeisl

To be sumbitted soon.

Influence of the Electrochemical Interface on adsorbed H

Rizwan Ahmed[a], Martin H. Hansen[a], Mårten E. Björketun[a], Jan Rossmeisl[a,*]

[a]*Center for Atomic-scale Materials Design, Department of Physics, Technical University of Denmark, DK-2800 Lyngby, Denmark*

**Jan.Rossmeisl@fysik.dtu.dk*

DFT calculated pH effect on adsorbed H

Abstract

We have studied electrochemical hydrogen adsorption from first principles using a model that accounts for potential and pH and explicitly treats the atomic structure of the electrode-electrolyte interface. We find that hydrogen adsorption is totally dominated by the electrode surface, and the interface barely influences the results. This shows that in the case of hydrogen the interaction between the surface and the electrolyte is negligible and the effect of pH is not visible in the results. We have also calculated the pseudo capacitances for Pt(100) and Pt(111) surfaces for hydrogen adsorption region, which agrees to the experiments.

1. Introduction

Any future sustainable energy scenario relies on effective electrochemical devices. Renewable energy, in the form of electricity, has to be averaged over time in order to secure a steady supply, which means that energy needs to be converted and stored.[1] Electrochemical systems such as fuel cells and electrolysers potentially offer a very efficient conversion and storage of energy. Electrochemical energy storage and conversion is intimately related to charge transfer reactions between ion-conducting electrolytes and electron-conducting electrodes. It is at this charged interface between the electrode and the electrolyte that the energy conversion takes place. Atomic scale insight is needed to fundamentally understand and improve the interfaces for energy conversion and storage. However, at present a comprehensive atomic–level picture of the electrochemical interface is lacking.

The surface reactions are mainly determined by the thermochemistry.[2,3] Therefore it is possible to obtain trends in surface electrocatalysis without including the interface and without explicit simulations of the electrolyte. The thermochemical driving force for surface redox reactions by protons is determined by the chemical potential of protons and electrons together. Consequently, the chemical potential of protons and electrons can be substituted with that of hydrogen molecules, which means that protons solvated in water never have to be explicitly calculated, as it is instead possible to refer to gas phase hydrogen. This theoretical trick can be referred to as the computational reversible hydrogen electrode (CHE) reference.[4]

Hydrogen adsorption has been intensively studied applying the CHE approximation,[5,6] whereas this approach is likely to provide insight into trends in adsorption and activity it is clear that the effect of the interface is totally neglected and the role of the electrochemical interface on the hydrogen

adsorption is out of the scope of this type of simulations. It is possible to qualitatively test the effect of the interface by adding a field and/or include water either explicitly or as a medium. The former type of calculations suggests that hydrogen on a Pt surface only very weakly feels the effect of the electrochemical interface, which explains why the CHE approach actually works. However, recent modeling contradicts this and suggests that the hydrogen adsorption on Pt 111 is dependent on pH.[7] We have previously presented a method for including pH and electrode potential in atomic-scale simulations.[8] The analysis performed in this paper is based on that method.

The aim of this paper is to investigate the effect of the electrochemical interface, including pH, on hydrogen adsorption on Pt(111) and Pt(100). Hydrogen adsorption on low index Pt is probably the simplest system to investigate and very well defined. For this benchmark system different simulation methods and experiments all have to agree. Simulations on the level of DFT for such a simple system should compare very closely to experiments, otherwise is it equally likely that the interpretation for the experiments or the analysis of the simulations is wrong. In this paper we present the first attempt to include pH in simulations of hydrogen adsorption with an explicit model for the electrochemical inetrface.

2. Computational details

The electronic structure problems were solved using density functional theory (DFT), based on the real space uniform grid based projector augmented wave (PAW)[9] method and the Revised Perdew−Burke−Ernzerhof (RPBE)[10] functional was used for exchange and correlation. The calculations were performed using the GPAW[11,12] software package integrated with the Atomic Simulation Environment (ASE)[13]. Pt(111) and Pt(100) metal surfaces were represented by periodically repeated 4-layer slabs, separated by at least 15 Å of vacuum in the direction perpendicular to the surface in order to ensure convergence of work functions and energies. An optimized lattice constant of 4.0 Å and a grid spacing of 0.18 Å were used for all calculations. For both (111) and (100) surfaces, surface unit cells of size (3×3) were employed and sampled with (4×4×1) Monkhorst-Pack k-point grids. Symmetry was applied to further reduce the number of k-points. In all the cases, a dipole correction[14] was applied in the direction perpendicular to the electrode surface in order to decouple the electrostatic interactions between periodically repeated slabs. The width of the Fermi smearing was set to 0.1 eV and energies were extrapolated to an electronic temperature of 0 K. The two bottom layers of the slabs were fixed in their bulk positions, while all other atoms were relaxed until the magnitude of the forces acting on them became less than 0.05 eV/Å.

3. Results

3.1. pH and field dependence of hydrogen adsorption

We have performed simulations on Pt(100) and Pt(111) covered with 0-2 monolayers of hydrogen in the presence of an explicitly treated bi-layer of water. The energy per surface Pt, accumulated at the interface as hydrogen is adsorbed, can be calculated according to equation (1), where G(n,N) is the energy of the interface with N surface Pt atoms and n hydrogen adsorbed and $G(H_2(g))$ is the energy of a hydrogen gas molecule at standard pressure and temperature. ΔG^{int} calculated this way is therefore the Gibbs-isotherm at zero vs. the computational hydrogen electrode (CHE).

$$\Delta G^{\text{int}} = \frac{G(n,N) - G(0,N) - \frac{1}{2}nG(H_2(g))}{N}, \quad (1)$$

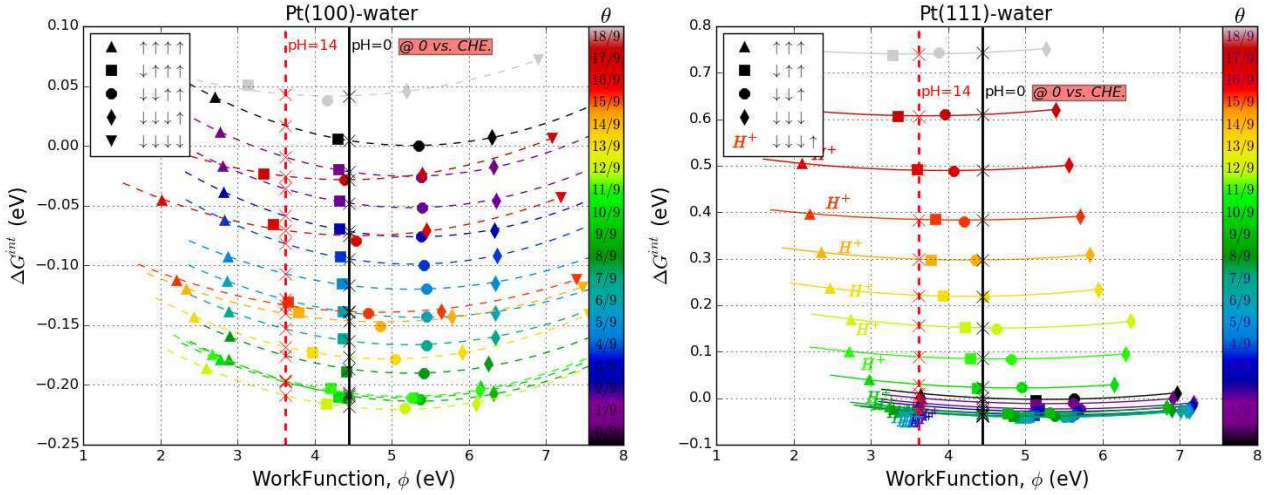

(a). *(b).*

Fig. 1: *ΔG^{int} for a) Pt(100) and b) Pt(111), plotted against the work function, ϕ, for different coverage of adsorbed hydrogen θ (indicated by the color). The legend shows the dipole orientation of the water structure, with H_up water indicated by ↑ and H_down by ↓. The black vertical line is the work function at zero potential vs. CHE for pH= 0 (ϕ = 4.44 V) and the red vertical line is the work function at zero potential vs. CHE for pH =14 (ϕ = 3.61 V).*

Fig. 1 shows the integral adsorption energy of hydrogen, $\Delta G^{\text{int}}(\phi, \theta)$, as a function of the work function, ϕ, of the interface for different hydrogen coverages, $\theta = n/N$. The different work functions originate from different orientations of the individual water molecules and hence their dipoles.[15] The energy of the hydrogen changes within a few hundreds of an eV as the orientations of the water dipoles change.

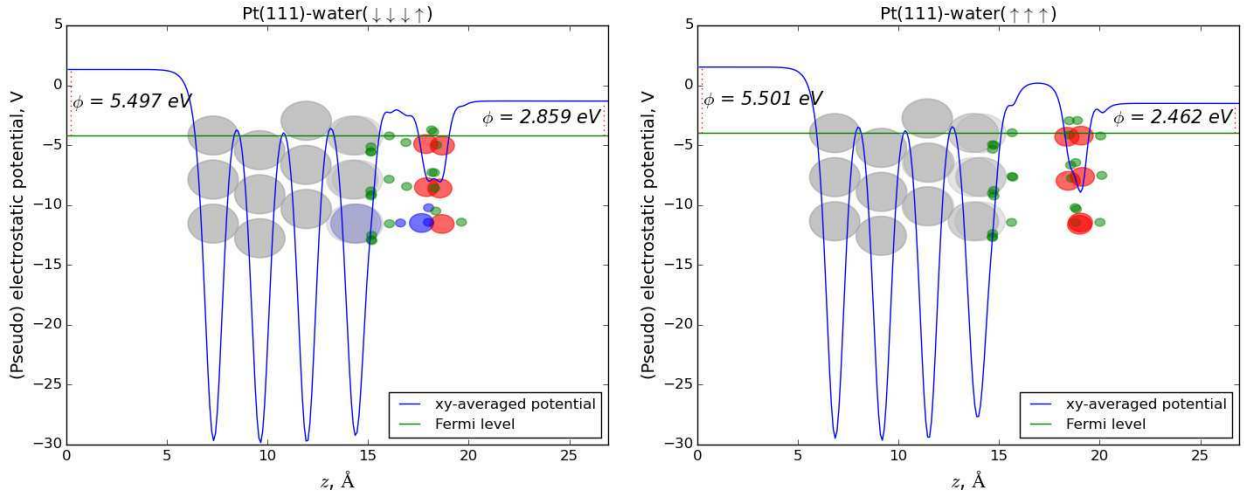

(a). *(b).*

Fig. 2: *Pt(111)-water interfacial atomic structures for a) Pt(111)_12H_{ad}- WL,H^+ and b) Pt(111)_13H_{ad}- WL. Both the sysems have equal number of atoms, but former system have proton which is coadsorbed between water and metal electrode shown by the corresponding oxygen atom in blue shade.*

This small variation is in agreement with previous simulations with a field added across the interface[2,16] and consistent with the small dipole moment of H* perpendicular to the surface.

Protons solvated in the water layer (WL) at the electrochemical interface might also interact strongly, at the same time with the metal surface, which will result in enthalpy gain and a barrier for it to reach the surface. However, for Pt surface, the calculations suggest[17,18,19,20,21,22,23] that as soon as the structure is relaxed, proton is transfered to the Pt surface except for the cases where the proton reacts with adsorbed hydrogen in order to make molecular hydrogen. Here we will also report a case, where the proton is more stable at the interface, being coadsorbed between Pt(111) surface and WL, where it interacts

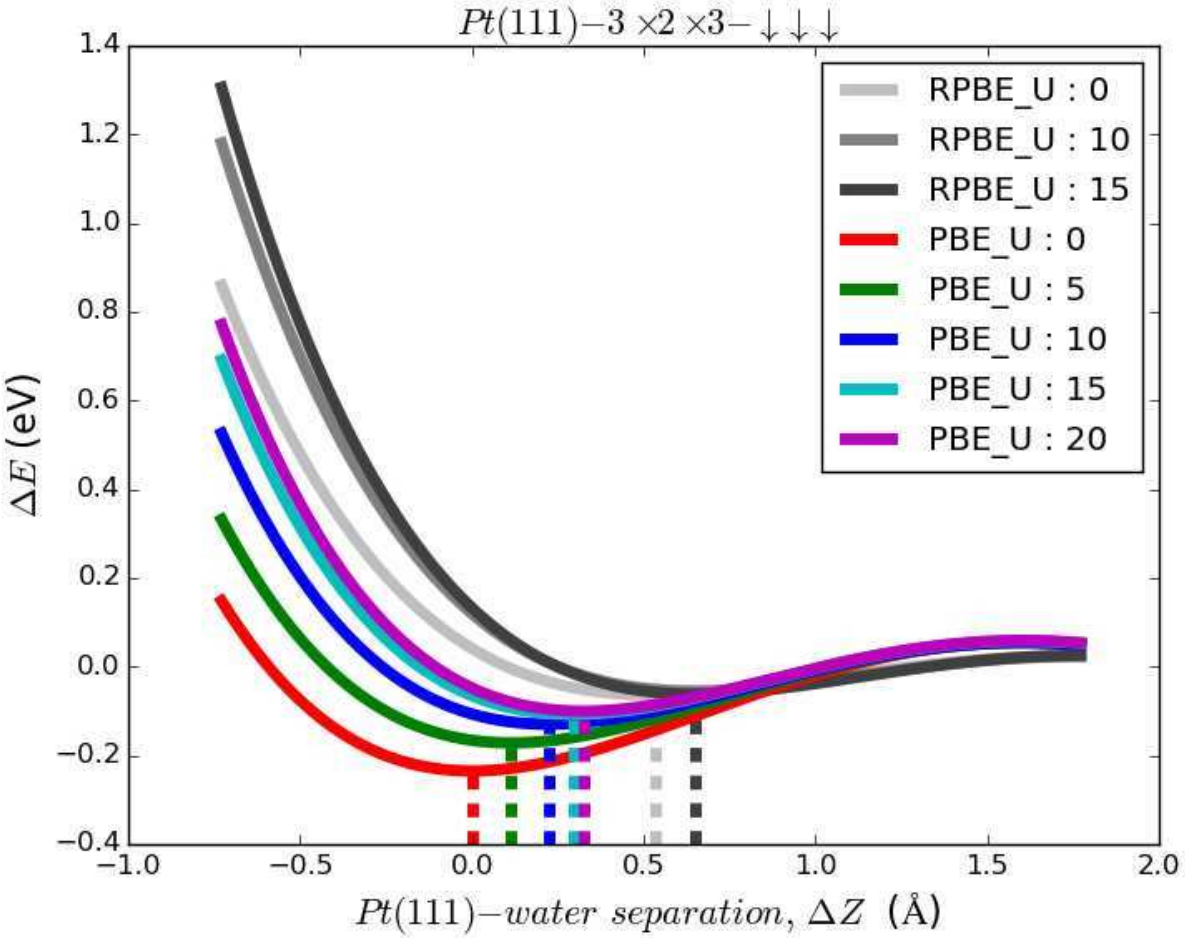

Fig. 3: Comparision of metal-water interaction and separation for: PBE and RPBE. Vertical dash lines show minima for each curve. The value at x-axis show the extra added/removed separation compared to fully relaxed structure at U=0 using PBE.

strongly with the Pt(111) surface by pulling up a Pt atom from the surface (similar to the case where it is adsorbed on an on-top). The corresponding atomic structure relaxed by using RPBE, is shown in Fig. 2a in comparison to a another system where this proton is replaced by H* adsorbed on the surface, cf. Fig. 2b. For the former case, the metal-water separation is considerably reduced due the proton being stable in the outer Helmholtz plane (OHP). This proton is more stable at the interface between WL and Pt(111) surface for the coverages (θ) less than 13/9 ML of hydrogen as suggested by H^+ symbols in Fig. 1b, but only for a specfic dipole of water layer (WL) as mentioned on top of Fig. 2a. This WL has thrice number of (out of plane) water molecules pointing down than pointing up, but still results in a workfunction which is more or less the same which we get with complete H_up WL as shown in Fig.

2b. So, the proton in the OHP, causes big change in the electrostatic environment in electric double layer (EDL). However, for coverages above 13/9 ML, this proton still hangs in the WL, where it is less stable than the being adsorbed on the surface.

RPBE usually suggest larger metal-water separation, and less chemical interaction between these two, compared to PBE functional as suggested by the Fig. 3. Significant charge trasfer at the interface is frequently observed, when PBE functional is used to model metal-water interface. It is due to the position of the HOMO level for the water (electrolyte), which is being too high in energy, when PBE functional is used.[24] However, if we add a U term, the metal-water interaction will decrease and separation between these two will increase by using PBE. At higher values of U, PBE will more or less produce the RPBE results as shown by Fig. 3. The metal-water interfaces, we report, are modeled using RPBE, and lies in the middle regime, where metal Fermi level is straddle by HOME-LUMO gap of the electrolyte, hence avoid artificial charge transfer [24].

We want to compare the hydrogen adsorption on Pt(111) and Pt(100) at pH=14 and pH=0, at constant potential vs. the computational hydrogen electrode (CHE), which means at constant chemical potential for $H^+ + e^-$. Therefore the value of ΔG^{int} at the work function corresponding to 0 vs. CHE is needed for all the coverages shown in Fig. 1. The energies are found by reading off the crossing with the two vertical lines in Fig. 1a and 1b. The solid black line at ϕ = 4.44 V corresponds to the work function of the standard hydrogen electrode defined at pH=0 and zero potential vs. CHE. The dashed red line at ϕ = 3.61 (=4.44 V -14*0.059 V/pH) indicates the work function at zero potential vs. CHE at pH=14.

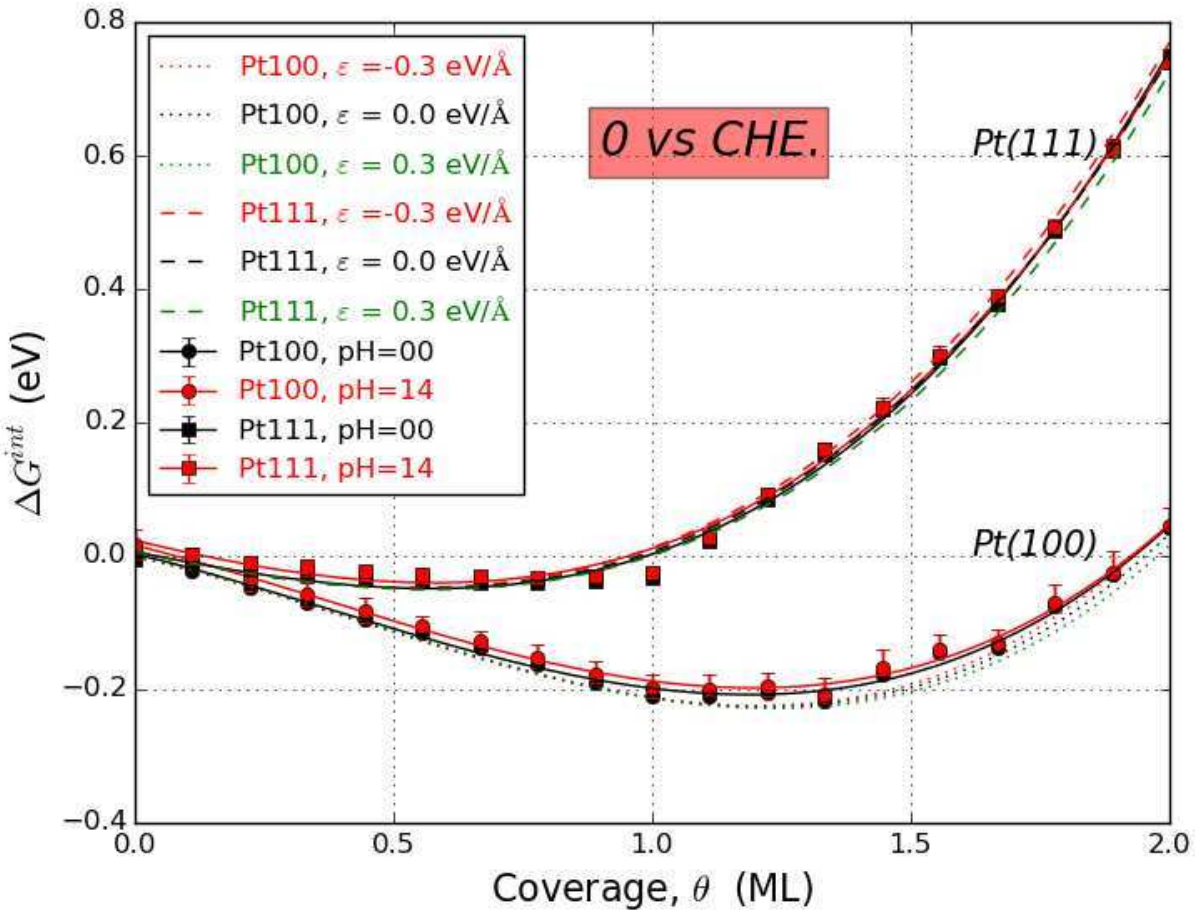

Fig. 4: ΔG^{int} plotted as a function of the hydrogen coverage. The black and red points correspond to the crossings of the black and red vertical lines with the different coverage lines in Fig. 1 (indicated by the x'es in Fig. 1). The dashed and dotted curves represent the results without water, with or without an electric field.

Fig. 4 reports the interpolated values of ΔG^{int} from Fig. 1, plotted as a function of the hydrogen coverage. Two distinctly different curves are shown for Pt(100) and Pt(111). These represent the energies of the interfaces when $H^+ + e^-$ is in equilibrium with hydrogen. The difference between the two curves reflects the difference in binding energy and the difference in interaction between the hydrogen atoms adsorbed on the surface. The repulsion is larger on Pt(111) than on Pt(100) because of the close-packed structure of the (111) surface. In addition, Fig. 4 reports results obtained in the absence of water, with and without a field. Comparing the different curves, it is obvious that for the surfaces investigated here neither pH nor water or electric field has any discernable influence on the adsorption. This strongly suggests that the interaction between hydrogen on the Pt surface and the electrolyte is very weak. This in turn means that hydrogen on Pt does not depend on the pH. This is a consequence of the very small dipole of hydrogen on Pt and the lack of any specific interaction between the electrolyte and the surface. In this study we have not pre-assumed any particular behavior of the energy with respect to the field, it is measured in the calculations. A change in work function does not necessarily give rise to a change in energy, thus there is no or very little influence of the pH and the nature of the electrolyte.

This study does not include any other possible ions than protons. However, those could only change the above results if they directly interact with the surface. Simply a change in the field will not influence the results reported here.

It is worth noticing that for stepped Pt a pH dependence in the hydrogen potential region has been observed experimentally.[25] This could be caused by hydrogen that on stepped surfaces gains a specific interaction with water or an interaction with the field. However, we do not consider that very plausible, as above one monolayer, where hydrogen adsorbs atop Pt atoms, they are still not interacting with the electrolyte. It is more likely that other species such as O*, HO* or water are strongly and specifically adsorbed on the defect sites. If these adsorbates interact strongly with the electrolyte, which is likely as they can form hydrogen bonds, the binding energy of these species becomes dependent on pH. The potential for hydrogen adsorption on defect sites therefore, indirectly, also becomes dependent on pH as the hydrogen has to replace e.g. adsorbed water, which is pH dependent. In principle this effect could also play a role for Pt(100) and Pt(111) if the water molecules are specifically adsorbed, however, this is not seen in the simulations. It should be noted that the description of water with standard GGA functionals could be debated; especially the too high position of the HOMO level can give rise to charge transfer from the water to the Pt surface. However, this artifact is not present in the simulations presented here. Moreover, the lack of vdW interactions could change the adsorption energy, but it has to be very large to give rise to a strong adsorption of water on the low index facets of Pt.

3.2. Capacitance

In the previous section we studied hydrogen adsorption at zero potential vs. CHE as we used standard gas phase hydrogen as reference. By a slight modification of Eq. (1) it is possible to extend the analysis to any computational reversible hydrogen potential. ΔG^{int} then becomes a function of the chemical potential of the hydrogen atoms as shown in equation (2).

$$\Delta G^{int} = \frac{G(n,N) - G(0,N) - \frac{1}{2}nG(H_2(g))}{N} + \frac{n}{N}eU_{CHE} \qquad (2)$$

Where $eU_{CHE} = -\mu_{H^+ + e^-}$ is the potential vs. CHE. Equation (2) and can be presented in a 3D plot with ΔG^{int}, ϕ and U_{CHE} as the three axes, cf. Fig. 5. Instead of having a line of pH = 0 for $U_{CHE} = 0$ we now get a plane for pH = 0 and ΔG^{int} as function of U_{CHE}.

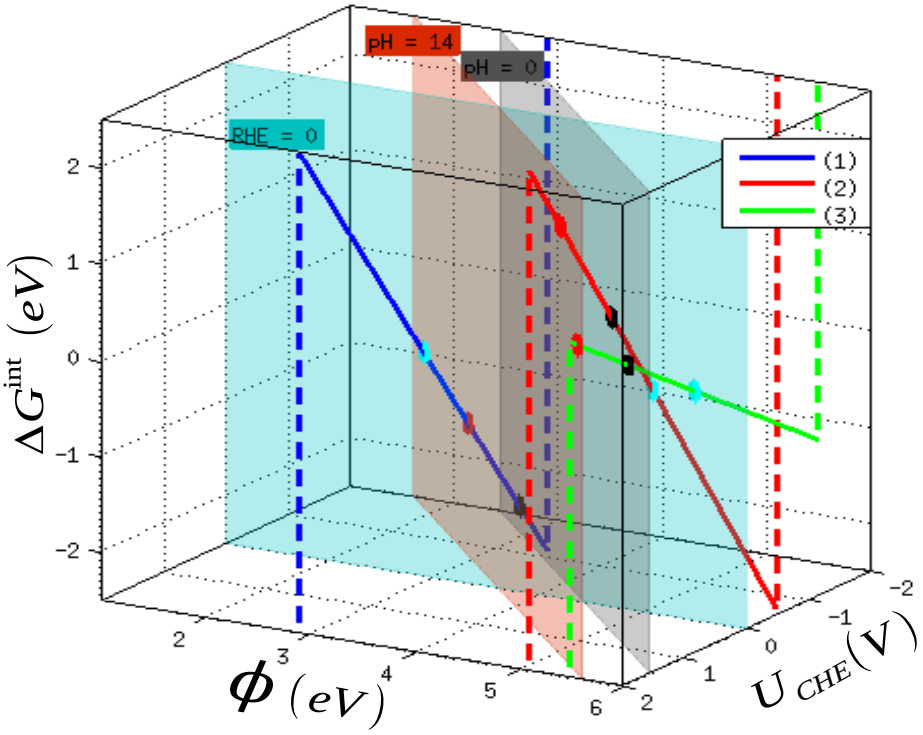

Fig. 5: ΔG^{int} as function of ϕ and U_{CHE} for exemplary metal|solution interfacial structures for Pt(100): (1) ϕ =2.9, θ=1.33, (2) ϕ=5.1, θ=1.44, (3) ϕ=5.5, θ=0.55. Colored marked circles on the lines show the projection of ΔG^{int} on the pH=0, pH=14 and CHE=0 planes. Dashed lines are shown as guides for the eye.

The CHE=0 plane intersects pH=0 and pH=14 planes at ϕ=4.44 eV and ϕ=3.61 eV, respectively. So, values of ΔG^{int} can be extrapolated for ϕ=4.44 eV and ϕ=3.61 eV using all the possible orientations of water mentioned in Fig. 1 in order to calculate ΔG^{int} values at pH=0 and pH=14 for $U_{CHE} = 0$ shown in Fig. 4.

The ΔG^{int} projections on pH=0 plane against corresponding U_{CHE} values for Pt(100) and Pt(111) are plotted in Fig. 6. These are the phase diagrams for hydrogen on Pt(100) and Pt(111). The first thing we note is that the coverage of hydrogen is increased as U_{CHE} is decreased. For Pt (111) hydrogen adsorbs in the FCC-hollow site until the coverage of 1 ML is reached, and upon further reduction of the potential the top sites start to be occupied. Ontop hydrogen is reactive and can form molecular hydrogen either with hydrogen atoms from neighboring hollow sites or with other ontop hydrogen. This means that in experiments it is impossible to accumulate two full monolayers of hydrogen on the surface. However, the simulations allow us to estimate the capacitance, when hydrogen atoms or protons and electrons are added to the interface.

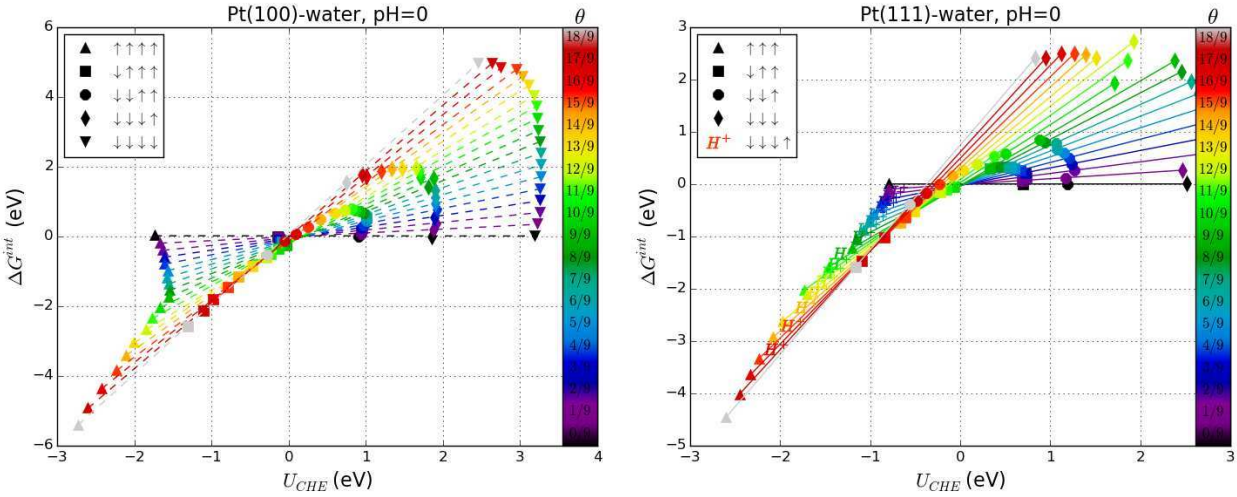

(a). *(b).*

Fig. 6: Phase diagrams for a) Pt(100) and b) Pt(111).

In Fig. 7 the results from Fig. 6 have been summarized and fitted to parabolas as shown above each plot. As before, there is no clear difference between the results at pH=0 and pH=14. The configuration and coverage with the lowest G^{int} for a given U_{CHE} defines the most stable structure of the interface. We will refer to this lower bound of G^{int} as $G^{int}(min)$. In the simulations the coverage can only be varied in steps defined by the number of surface atoms in the slab. However, by means of interpolation, as shown in Fig. 4, it is possible to obtain a continuous curve for $G^{int}(\theta)$ that can be directly translated into a continuous $G^{int}(min)$, cf. Fig. 7 and appendix.

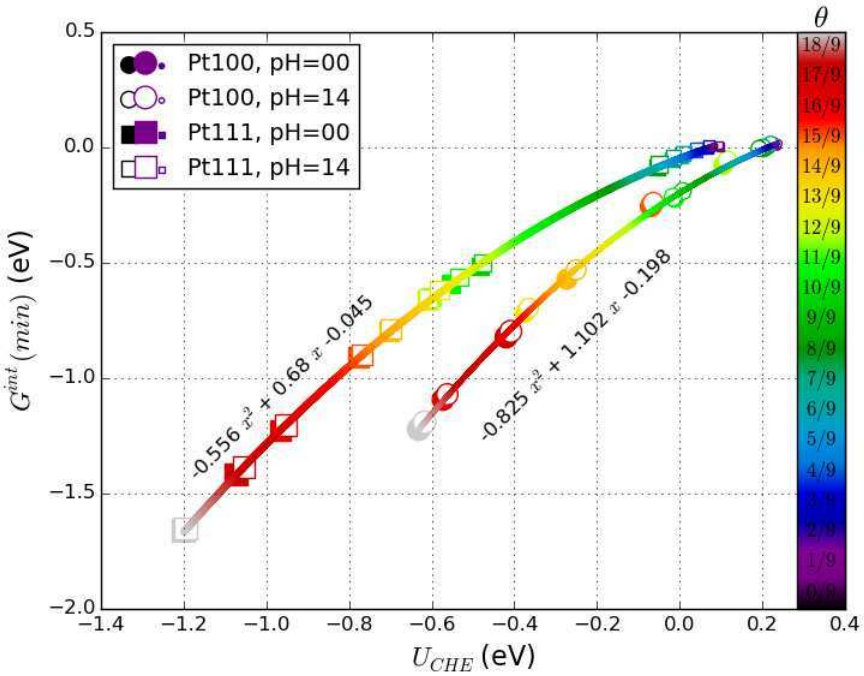

Fig. 7: The phase diagrams from Fig. 6a and 6b showing $G^{int}(min)$ as function of U_{CHE}.

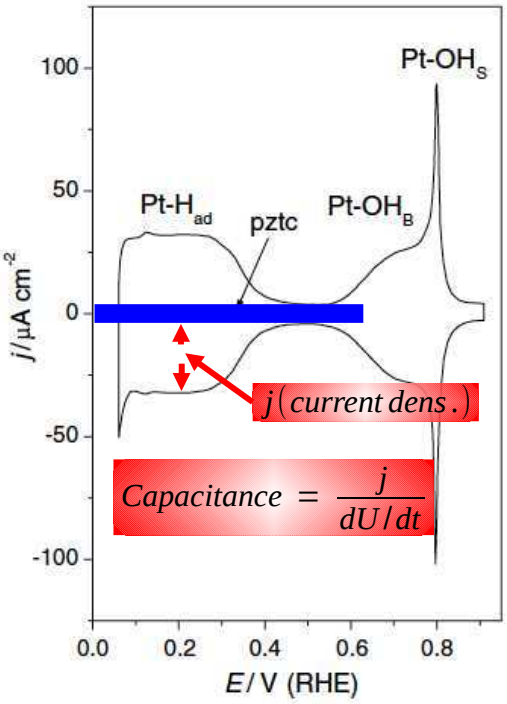

Fig. 8: State of the art Pt(111) cyclic voltammogram in 0.1 $HClO_4$ M solution at 50 mV^{-1}. Adapted from [25].

The curvature of G^{int}(min) shown in Fig. 7, is related to the capacitance. The capacitance is dominated by adsorption of hydrogen on the surface. The work function only plays a negligible part. The DFT calculated pseudo capacitance from curvature for Pt(111) is ~257 uF/cm^2(see the appendix), which is to be compared with experiments. In order to get experimental reference, we used experimental cyclic voltammogram as shown in Fig. 8. Considering the cyclic voltammogram, the current density for only the hydrogen adsorption or desorption region (half of the total width) can be divided with sweep rate, in order to get pseudo capacitance. If we account for background double layer capacitance, we get pseudo capacitance for H adsorption, which is around ~500 uF/cm^2 for Pt(111).[26,27,28,29] We have deduced this value from voltammogram, where the current density is almost flat with respect to potential and capacitance is given by j/(dU/dt).[1] This is the potential region where most of the hydrogen is adsorbed on the FCC-hollow site (just before hydrogen evolution region). DFT overestimates the distance among metal atoms, and we used optimized lattice constant which is 4.02 Å, which is different than experimentally known value of ~3.92 Å. The capacitances are reported in uF/cm^2, which is part of reason that DFT suggest slightly less capactitance. For Pt(111), it is unlikely that other ions are co-adsorbed in this potential range. However, for Pt(100), other ions might also be co-adsorbed in the hydrogen adsorption region, but a deduced value of ~425 uF/cm^2 can be compared with DFT calculated pseudo capacitance ~331 uF/cm^2.[28,30]

4. Conclusion

We have shown that on low index Pt facets, electrochemical hydrogen adsorption is totally dominated

1
dU/dt is the sweep rate

by the electrode surface, the interface barely influences the results. This shows that in the case of hydrogen the interaction between the surface and the electrolyte is negligible and the effect of pH is not visible in the results.
Previous studies have found the same, except studies where an energy dependency on the work function is assumed a priori e.g. with a capacitor model. In this study we do not assume any energy dependencies on the work function, however, it is calculated to be very small.

The simulations only contain a single water layer, however, as this layer does not play a role additional water layer cannot do that either. The description of water is based on standard GGA. This is probably fine for the hydrogen covered surfaces, but the results for clean surfaces could change slightly if higher-level functionals were used. This could give rise to a small pH dependence if the adsorption energy of physisorbed water changes with the work function. However, the mayor limitation of the analysis presented in the current paper is probably related to the lack of counter ions. This could influence the structure.

5. Appendix

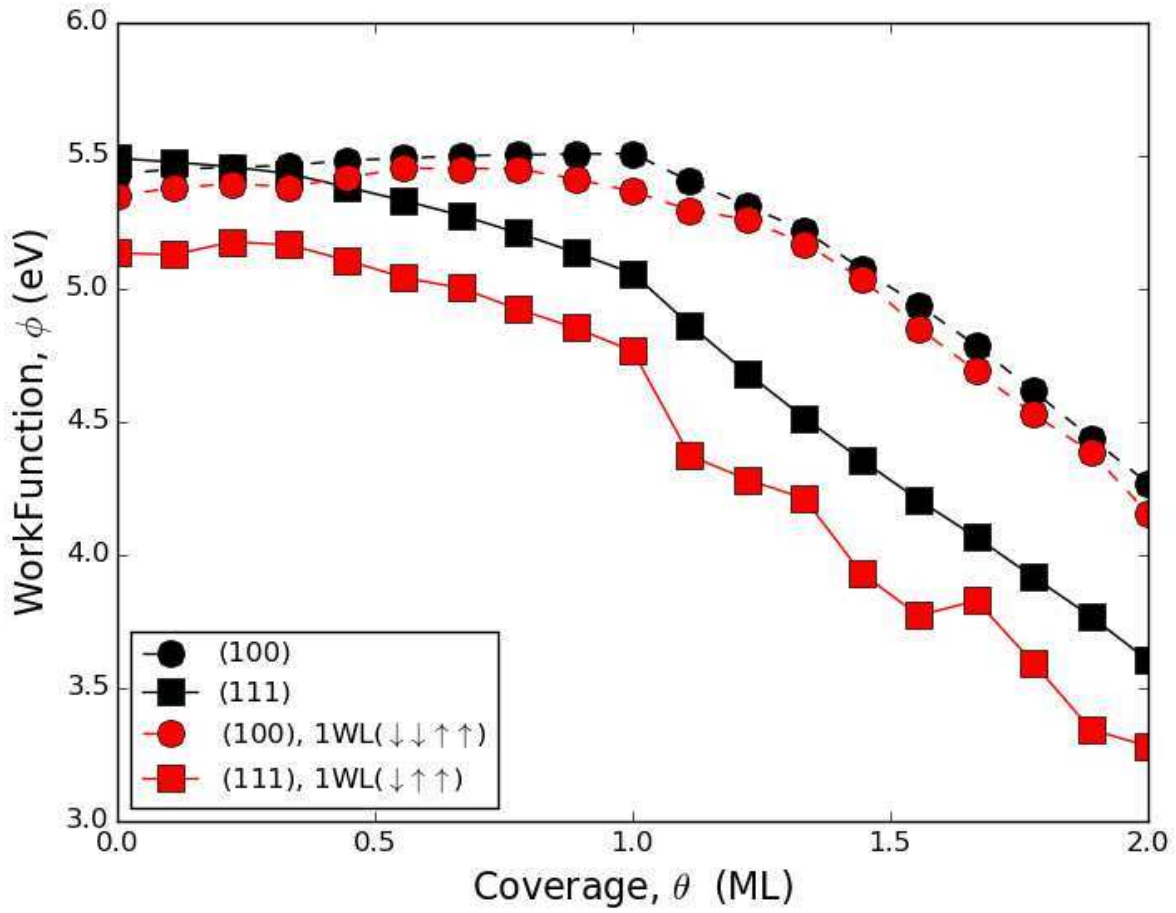

Fig. 9: Change in workfunction, ϕ, as a function of coverage, θ.

The Fig. 9 shows, how the workfunction change as we increase the coverage for both Pt(100) and Pt(111) surfaces. Results with and without water layer are reported, however, for Pt(111) surface, the modeled water layer has a finite dipole as shown in the legend.

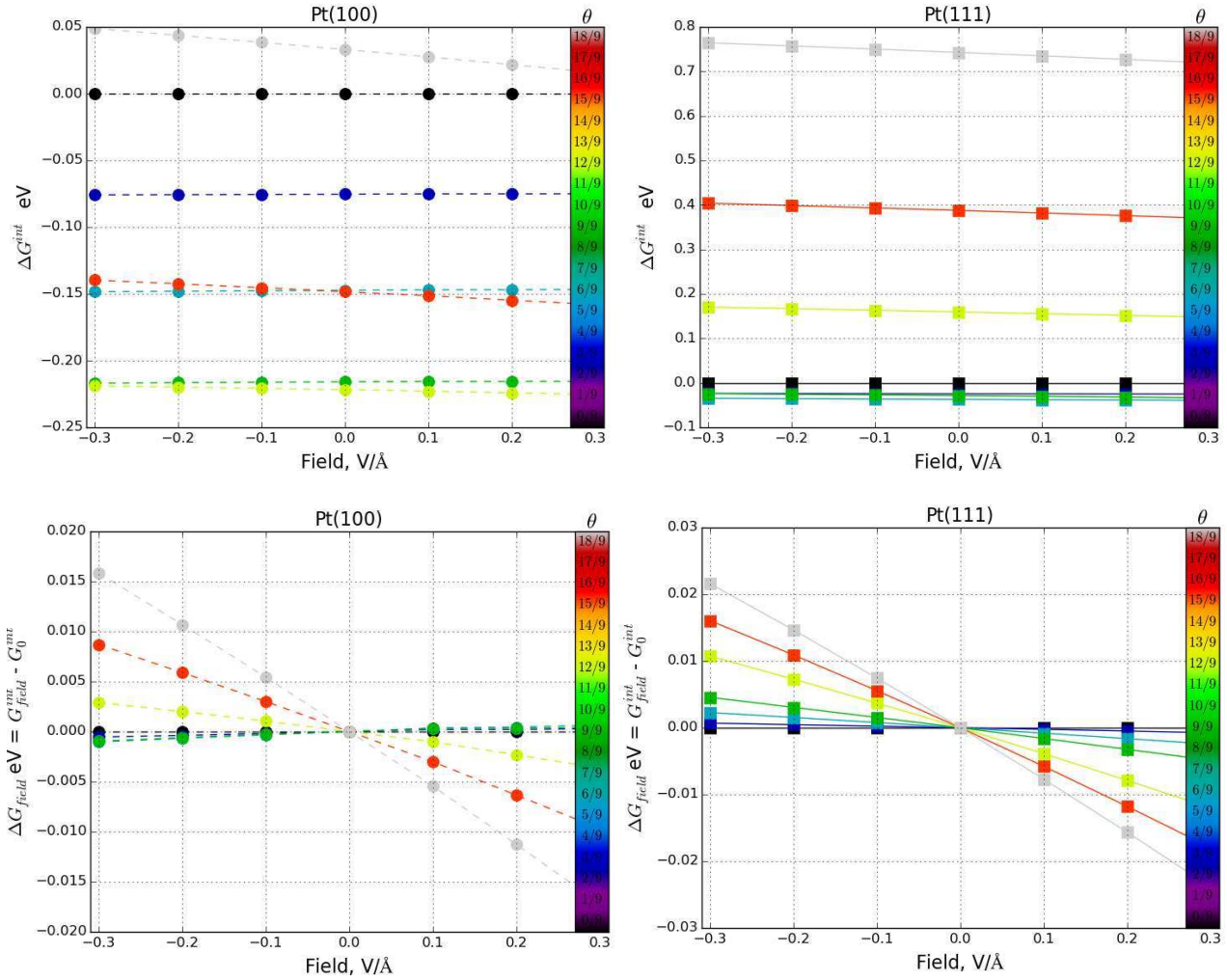

(a). *(b).*

Fig. 10: Change in G^{int} with respect to external applied field.

Fig. 10 reports the results where we have explicitly applied the external field instead of using water layers to set up a field at the interface.These results are also reported in Fig. 4.

The curve in Fig. 7 represents the minimum of G^{int} as a function of CHE potential. G^{int}(min) is made up by lines of the different coverages with the slopes θ. These lines can be viewed as tangents $T(\theta,U)$ to G^{int}(min). If the function of $G^{int}(\theta)$ as function of coverage is known then G^{int}(min) can also be calculated.

$$T(\theta,\ U) = \theta(U - U_0) + G^{int}(\theta,\ U_0) \tag{3}$$

At G^{int} (min),

$$T(\theta,\ U) \approx T(\theta+\delta\theta,\ U) \tag{4}$$

$$\theta(U - U_0) + G^{int}(\theta, U_0) = (\theta+\delta\theta)(U - U_0) + G^{int}(\theta+\delta\theta, U_0) \quad (5)$$

$$\theta(U - U_0) - (\theta+\delta\theta)(U - U_0) = G^{int}(\theta+\delta\theta, U_0) - G^{int}(\theta, U_0) \quad (6)$$

$$-\delta\theta(U - U_0) = \delta G^{int}(\theta, U_0) \quad (7)$$

$$(U - U_0) = -\frac{\delta G^{int}(\theta, U_0)}{\delta\theta} \quad (8)$$

As G^{int}(min) is the intercept of tangents with the slopes $\theta + \mathrm{d}\theta$. In other words, at the intercept,

$$T(\theta, U) = G^{int}(min)(U) \quad (9)$$

So, calculating G^{int} at the intercepts,

$$G^{int}(min)(U) = -\theta\frac{\delta G^{int}(\theta, U_0)}{\delta\theta} + G^{int}(\theta, U_0) \quad (10)$$

Considering the above equation (10), I have assumed U_0 (CHE potential) to be 4.44 and 3.614 for pH=0 and pH=14 respectively. I have calculated U vs. CHE for each coverage, where this coverage (tangents as mentioned by equation (9)) will give us G^{int}(min). So, we have set of points (each for every coverage), having values (U vs. CHE, G^{int}(min)). So, plotted circles and squares are for Pt100 and Pt111 surfaces respectively, where the filled symbols are for pH=0 and empty symbols are for pH=14 shown in Fig. 7.

I have interpolated all these points with parabolic fit, in such a way that the color of the line, which is showing the coverage, is also interpolated. It shows where each coverage starts to dominate as we change potential. So, this way we have get the G^{int}(min) for continuous coverage, instead of discrete coverage values. Parabolic equation from each parabola fit is also plotted over each parabola. So from these parabolas we can calculate capacitance for each surface (Pt100, Pt111).

We know that parabolic equation for G^{int}(min) can be written as equation (11). so from the curvature of these parabolas we can calculate capacitance for each surface (Pt100, Pt111). Calculated capacitances for Pt100, and Pt111 are 331 and 257 uF/cm^2 respectively.

$$G^{int}(min)(U) = -\frac{1}{2}CU^2 + bU + c \quad (11)$$

Acknowledgments

The CASE initiative is funded by the Danish Ministry of Science, Technology and Innovation. Support

from DCSC, DCTI's FTP program and SERC is gratefully acknowledged.

References

1. H. Wenzel, *"Breaking the biomass bottleneck of the fossil free society"*, Concito (2010).

2. J. Rossmeisl, J. K. Nørskov, C. D. Taylor, M. J. Janik and M. Neurock, *J. Phys. Chem. B* **110** (2006) 21833−21839.

3. G. S. Karlberg, J. Rossmeisl and J. K. Nørskov, *Phys. Chem. Chem. Phys.* **9** (2007) 5158−5161.

4. J. K. Nørskov, J. Rossmeisl, A. Logadottir, L. Lindqvist, J. R. Kitchin, T. Bligaard and H. Jónsson, *J. Phys. Chem. B* **108** (2004) 17886−17892.

5. J. Greeley, T. F. Jaramillo, J. Bonde, I. Chorkendorff and J. K. Nørskov, *Nature Mater.* **5** (2006) 909−913.

6. M. E. Björketun, A. S. Bondarenko, B. L. Abrams, I. Chorkendorff and J. Rossmeisl, *Phys. Chem. Chem. Phys.* **12** (2010) 10536−10541.

7. N. Bonnet and N. Marzari, *Phys. Rev. Lett.* **110** (2013) 086104.

8. Rossmeisl, J., Chan, K., Ahmed, R., Tripkovic, V., & Björketun, M. E. (2013). pH in atomic scale simulations of electrochemical interfaces. *Physical Chemistry Chemical Physics*, *15*(25), 10321-10325. 10.1039/c3cp51083b

9. P. E. Blöchl, *Phys. Rev. B* **50** (1994) 17953−17979.

10. B. Hammer, L. B. Hansen and J. K. Nørskov, *Phys. Rev. B* **59** (1999) 7413−7421.

11. J. J. Mortensen, L. B. Hansen and K. W. Jacobsen, *Phys. Rev. B* **71** (2005) 035109.

12. J. Enkovaara, C. Rostgaard, J. J. Mortensen, J. Chen, M. Dułak, L. Ferrighi, J. Gavnholt, C. Glinsvad, V. Haikola, H. A. Hansen, H. H. Kristoffersen, et al., *J. Phys.: Condens. Matter* **22** (2010) 253202.

13. Atomic Simulation Environment (ASE), [https://wiki.fysik.dtu.dk/ase], Center for Atomic-scale Materials Design (CAMD), Technical University of Denmark.

14. L. Bengtsson, *Phys. Rev. B* **59** (1999) 12301−12304.

15. S. Schnur and A. Groβ, *New J. Phys.* **11** (2009) 125003.

16. G. S. Karlberg, T. F. Jaramillo, E. Skúlason, J. Rossmeisl, T. Bligaard and J. K. Nørskov, *Phys. Rev. Lett.* **99** (2007) 126101.

17. E. Skúlason, V. Tripkovic, M .E. Björketun, S. Gudmundsdóttir, G. S. Karlberg, J Rossmeisl, T. Bligaard, H Jónsson and J. K. Nørskov, *J. Phys. Chem. C* 114, 18182-18197 (2010).

18. E. Skúlason, G. S. Karlberg, J. Rossmeisl, T. Bligaard, J. Greeley, H. Jónsson and J.K. Nørskov, *Phys. Chem. Chem. Phys.* 9, 3241 (2007).

19. M. Otani, I. Hamada, O. Sugino, Y. Morikawa, Y. Okamoto and T. Ikeshoji, *J. Phys. Soc. Jpn.* 77, 024802 (2008).

20. C. D. Taylor, S. A. Wasileski, J.-S. Filhol and M. Neurock, *Phys. Rev. B* 73, 165402 (2006).

21. R. Jinnouchi and A. B. Anderson, *J. Phys. Chem. C.* 112, 8747-8750 (2008).

22. M. J. Janik, C. D. Taylor and M. Neurock, *J. Electrochem. Soc.* 156, B126-B135 (2009).

23. J. S. Filhol and M. Neurock, Angew. *Chem. Int. Ed.* 45, 402 (2006).

24. Björketun, M., Zeng, Z., Ahmed, R., Tripkovic, V., Thygesen, K. S., & Rossmeisl, J. (2013). Avoiding pitfalls in the modeling of electrochemical interfaces. *Chemical Physics Letters*, *555*, 145-148. 10.1016/j.cplett.2012.11.025

25. J. Durst, A. Siebel, C. Simon, F. Hasch, J. Herranz and H. A. Gasteiger, *Energy Environ. Sci.* **7** (2014) 2255−2260.

26. Alexander S. Bondarenko, Ifan E. L. Stephens, Heine A. Hansen, Francisco J. Perez-Alonso, Vladimir Tripkovic, Tobias P. Johansson, Jan Rossmeisl, Jens K. Nørskov, and Ib Chorkendorff, *Langmuir* 2011, 27(5), 2058–2066

27. Antonio Berná, Víctor Climent, Juan M. Feliu, *Electrochemistry Communications* 9 (2007) 2789–2794

28. D. Strmcnik, D. Tripkovic, D. van der Vliet, V. Stamenkovic, N.M. Marković, *Electrochemistry Communications*, 10 (2008) 1602–1605

29. Marc T.M. Koper, *Electrochimica Acta* 56 (2011) 10645– 10651

30. DeHao Chen, JinYu Ye, ChangDeng Xu, Xin Li, JunTao Li, ChunHua Zhen, Na Tian, ZhiYou Zhou, ShiGang Sun, *Science China Chemistry*, Volume 55, Issue 11, pp 2353-2358